On the Effect of Boundaries on Confined Vortex Matter Systems

Austin Alexander Tomlinson

A Thesis Submitted to

The University of Birmingham

for the Degree of

DOCTOR OF PHILOSOPHY

Theoretical Physics Group

School of Physics and Astronomy

The University of Birmingham

February 19, 2018

Abstract

In this thesis, we investigate the effects of boundaries on confined superconducting vortex matter systems. We are primarily interested in understanding the properties of the so-called 'row-drop' transition in a density-driven, confined flow channel, reported by J. Watkins [111, 112]. We present numerical and analytic calculations that reveal chaos, structural progression, and novel energetic behaviour.

Firstly, we study a cylindrical geometry of confined vortices. Vortices align to form a regular structure that wraps around the cylinder in a commensurate fashion. We find a set of analytic equations and solve them *exactly* to find all possible lattices. Combining numerical results with energetic arguments enables us to construct the phase diagram of structural ground states for arbitrary circumference and density.

Following this, we generalise the results from the cylinder to a numerical study of a conical geometry of flowing vortices. We are able to accurately predict the lattice structures given the geometry of the cone and the density of vortices on its surface. By developing the theory of lattice structures on the cylinder, we propose a way of generating a single flowing lattice on the cone, subject to a source and sink reservoir of vortices at either end. Numerical simulations confirm this proposition.

Finally, we simulate vortices confined to a narrow, constricted channel constructed out of static, pinned vortices. By carefully controlling system parameters, we observe the emergence of chaotic behaviour centred at the aperture of the constriction. We present results diagrammatically and analyse them using established techniques to extract Lyapunov exponents from time series data.

This thesis is dedicated to the love of my life, Helena.

Acknowledgements

There are a number of people who have influenced me during the course of this project and to whom I am grateful.

Helena, thank you for your patience with me while I pursued my interests in physics. Your constant support has meant everything to me.

To my parents, thank you for giving me the freedom to make the choices that shape my life.

To my supervisor, Professor Nicola Wilkin, thank you for all the support and encouragement you have given me over the years. Your guidance has led me into an area of science that I am truly passionate about.

To all the research students I have had the pleasure to work next to, your ideas and discussions have been invaluable to me. I would particularly like to thank Dr Jon Watkins for his insights into the physics of vortex matter, technology, and everything in between.

Thank you to Professor Mike Gunn for the stimulating discussions and insights which have accelerated my research. Thanks to Professor Ray Jones for all the encouragement and curries. I would also like to thank Dr Martin Long for his dedication to postgraduate teaching.

Contents

List of Figures

1 Table of Physical Constants

Certain physical constants are used throughout this thesis and are all listed here [6]. Standard SI values are given to four significant figures.

Symbol	Definition	Value
h	Planck's Constant	6.626×10^{-34}Js
$\hbar$	Planck's Constant Modified ($\hbar \equiv h/2\pi$)	1.055×10^{-34}Js
m_e	Electronic Mass	9.109×10^{-31} Kg
e	Electronic Charge	-1.602×10^{-19} C
μ_0	Permeability of Free Space	$4\pi \times 10^{-7}$ TmA^{-1}
c	Speed of Light in Vacuo	3×10^{8} ms^{-1}

2 Introduction

Boundaries play a major role in the physics of many real systems. Bulk material properties are useful when trying to understand macroscopic quantities such as electrical resistance or mechanical stress responses, but are insufficient when considering the underlying microscopic properties. In mesoscopic systems of length scales intermediate to the atomic systems governed by quantum mechanics and classical thermodynamic bulk systems, individual particle motion is often important and leads to collective phenomena reliant on the entire system behaving coherently. Examples of collective phenomena in mesoscopic systems includes soliton flow in vortex flow channels [23], row-drop transitions in density-driven vortex channels [111, 112], and structural transitions in confined Wigner Crystals [89]. In all of these systems, the *boundaries*, in conjunction with the confined matter, are responsible for the observed properties.

We are interested in flow channels of vortex matter in superconductors that are strongly influenced by the boundaries that confine motion. They fall into the category of discrete soft matter systems where each unit of matter is large (can be considered a classical object), highly localised, and one of a few hundred particles that populate the system. The method of the confinement can cause effects for which there is no continuum analogue, such as soliton flow in narrow channels [23].

Our previous work focussed on narrow channels of confined vortex matter [108, 109]. We identified novel patterns of flow and structure attributed to the commensurability of the pinned lattice that confines flowing vortices. We also reported unusual time de-

pendence of the 'zig-zag' transition, when a single chain of vortices was strained beyond its critical point. Figure 1 shows single, double, and triple chain structures. The zig-zag transition occurs when neighbouring vortices on a single chain alternatively diffuse up and down. This thesis takes the ideas of structural transitions of these quasi-1D structures and investigates different types of confinement to study the physical mechanisms in more detail.

As well as being excellent choices for soft matter studies, vortices require a superconductor to exist. Narrow superconducting channels are highly tunable, which means vortex density, width, and driving force are all easy modified. Vortex density can be changed by tuning an applied magnetic field, width can be changed during the fabrication process, and driving force can be changed by varying an applied electric current. The quasi-one-dimensionality of narrow channels means we can understand the physics in simpler terms than for full two-dimensional flow since there are fewer variables to contend with.

In this thesis, we are interested in vortices on thin-film superconductors. They will be treated as 2D objects on a plane, giving the analytical and computational advantage of a simpler dimensional system than 3D, and are highly controllable by pinning and driving with various methods. We study systems of vortices with different boundaries and investigate the flow and structure that emerges.

The work presented in this thesis is divided into three parts: cylindrical confinement, conical confinement, and narrow constricted flow channels. Each part investigates a dif-

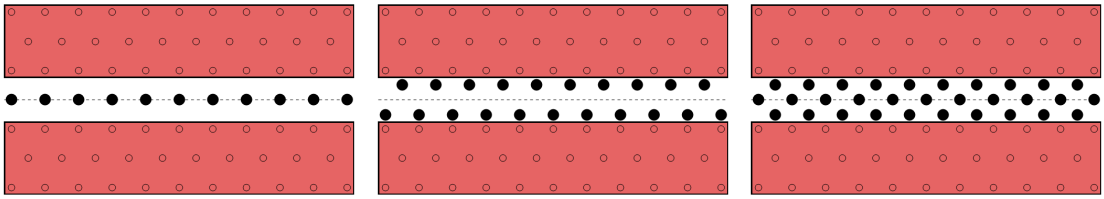

Figure 1: Sketches adapted from [23, 108, 109]. Examples of one, two, and three chains of vortices confined to a channel where the edges are formed by an array of static pins. The commensurability of the pinning lattice dictates the alignment and positioning of the chains to minimise the interaction energies to vortices. Open circles represent pinned vortices and closed circles represent free vortices. Diagram not drawn to scale in order to highlight the patterns; vortices are typically closer to the centre line of the channel.

ferent aspect of reported features of the wide, density-driven channel [111, 112].

2.1 Motivation

We are primarily motivated to understand certain aspects of the work presented in [112]. By studying a density driven lattice of vortices, confined to a channel, a number of questions have been raised from the observations of so-called "row-drop" transitions:

- How do changes in the number of flowing rows occur?
- Can we predict where a row-drop transition will occur?
- Can we learn anything by studying a row-drop transition down to a single row of vortices?

Figure 2 shows an example of a density-driven flow of vortices with a row-drop transition. An array of vortices are placed on the boundary of the flow channel to confine flowing matter. This causes a periodic term in the confining potential that causes dislocations and the 'freezing' of vortices close to the edges [111, 112]. The width of the channel is typically of the order of ten lattice spacings wide, which leaves a resultant confining potential along the centre of the channel that is weak compared to the more strongly confined

systems discussed in section 2.1.1. When source and sink reservoirs of vortices are implemented, a flow from high to low density occurs and 'row-drop' transitions are observed.

As the vortex lattice flows from high to low density, the underlying structure of a distinct number of rows will strain. At a critical point, it is energetically favourable to reconfigure the lattice by removing a row. This is mediated by a dislocation pair of vortices at the transitional interface that act to 'unzip' N rows into $N-1$ rows.

This strain can be attributed to several key factors:

- The channel width.
- The local density of vortices.
- The commensurability of the confining lattice.

The first two factors are intertwined since changing the width affects density. The commensurability is a factor because the dislocations that mediate the row transitions interact with so-called 'Geometrically Necessary Dislocations' (GNDs). These dislocations form as a result of a flowing lattice shearing past the static pinned edges. When row-drop dislocations collide with GNDs, their Burgers vectors combine and the row-drop vortex reflects back into the channel.

We study a system of cylindrically confined vortices to investigate how row-drops occur without a pinned confining lattice. By changing the boundaries, we aim to simplify the mathematics by making the geometry the focus, as opposed to the details of the interaction potentials. We aim to find solutions that span the entire parameter space as a result.

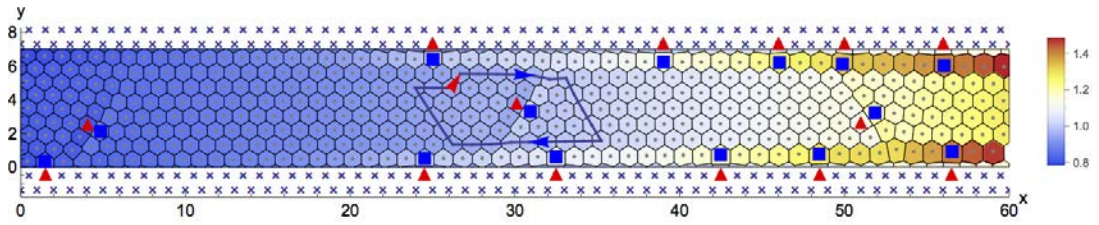

Figure 2: Figure taken directly from [111, 112] of density-driven vortices confined in a channel of width of $4\sqrt{3}a_0$, where a_0 is the natural lattice spacing of the pinned edge vortices. Initially there are 9 rows of vortices on the left of the channel and a transition to 8 occurs at $x \simeq 4$, mediated by a pair of dislocation vortices. Additional transitions from $8 \to 7$ occur at $x \simeq 30$ and $7 \to 6$ occur at $x \simeq 51$. The circuit drawn around the $8 \to 7$ transition is used to find the Burgers vector which indicates a lattice dislocation [113] by calculating the vector difference when following a rectangular loop of local lattice vectors. Pinned vortices are denoted with an $\times$ and flowing vortices with a point. Dislocation vortices are denoted by ▲ (5 neighbours) and ■ (7 neighbours). Commensurability with the flowing lattice's varying density and the pinned edges causes dislocations to form along the edges known as 'Geometrically Necessary Dislocations' (GNDs). The size of individual unit cells are indicated by the legend and colour scheme. Note that flowing vortices near to the edges are subject to stronger pinning than central vortices, which manifests as a freezing phenomena. The colour legend represents the local density of each unit cell scaled with the lattice parameter.

We search for insight into where to expect row-drop transitions and whether we can predetermine any that occur based on initial system parameters. We ultimately reflect on the applicability of our results on the parabolically confined systems, especially the tendency for helical states to form only on the cylinder. The results we obtain are generalisable, and we do so by investigating a cone-like geometry in section 8 and demonstrate the ability to control a dislocation-free flow.

The density driven flow channel also has a 'noise removal' mechanism, where dislocations leaving the source reservoir are absorbed by a row-drop dislocation. We will see in section 8 that without row-drop dislocations, these source dislocations will travel through the entire channel unimpeded.

We also investigate the row-drop transition in a narrow channel where we expect less noise from multiple rows of vortices moving past the transition and focus on a single constriction that forces rows to recombine.

2.1.1 Row Transitions in other Confined Channels

It is helpful to have an expectation of what results may look like by considering other systems that have been previously studied.

By restricting the freedom of vortices in a given direction by, for example, applying a parabolic confining potential that minimises energy along a central line, vortices align in rows along it. This is converse to the elementary properties of vortices without confinement; the natural bulk state of vortices is a triangular lattice and we study deviations away from this. Depending on the confining strength and the density, different numbers of rows form.

Under strong confinement, observations of row transitions have been reported in Wigner Crystal systems [88]. Wigner Crystals are 2D lattices of electrons at sufficiently low density that interact via a screened electrostatic interaction: a Yukawa potential [116, 122]. Depending on the density and confinement strength, numerical results determine different numbers of aligned rows of particles that form structural ground states. When investigating these systems at zero temperature ($T = 0$K), only energetics need to be accounted for. This simplifies the calculations and gives a limit for more complicated finite temperature calculations to tend towards. We discuss these results further in Section 4.1 and highlight

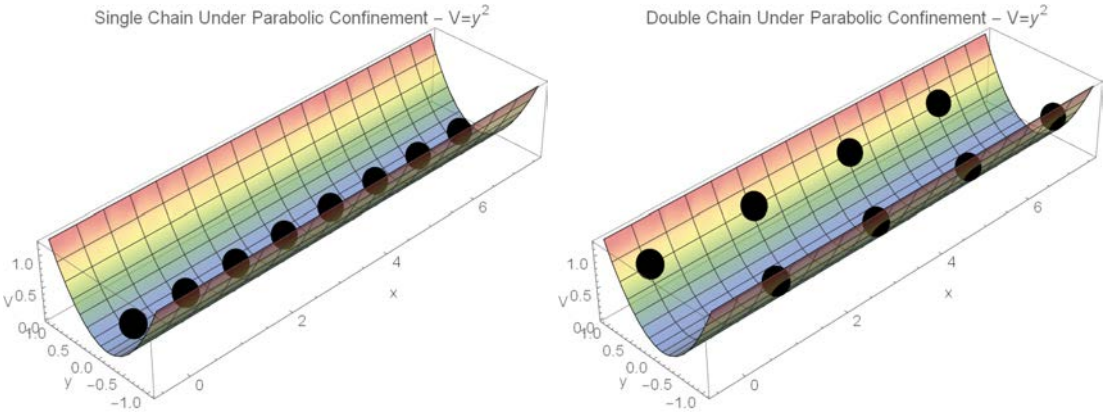

Figure 3: Depictions of discrete chains of particles under parabolic confinement in a single and double chain configuration. Under certain conditions of confinement strength and particle density, a single, double, triple, or higher chain configuration will be the structural ground state of the particles. The x and y axes represent the 2D position of the particles. The z axis represents the value of the potential each vortex has. This diagram is an analogue to repulsive particles confined in a literal hard parabola under gravity. The colour scheme is used for artistic reasons.

the techniques that we use in our own calculations.

2.2 Constricted Flow Channels

We will focus on constricted flow channels in section 9. We use them with the primary purpose of forcing row-drop transitions for parabolically confined particles.

The row-drop mechanism has been analysed numerically and analytically in channels with several rows of vortices, where two of them usually combine into one [111, 112]. The primary example of this is shown in fig. 2. The two rows that combine change to different neighbouring rows when the dislocation at the transition point moves up and down the channel. In the example shown, the row drop dislocations oscillate in the $y-$direction, interact and combine with GNDs and change direction. Because the combination of two

rows occurs next to other flowing rows, the physics of the row-drop mechanism is complicated by other flow effects. To study row-drop mechanisms in an environment with *only* the combining rows, we consider a narrow constriction, which reduces two or three rows down to one in a cleaner environment.

Section 2.2 shows an example of a transition line between the number of rows of particles under parabolic confinement. The confinement is a factor in determining the ground state. We explore this system in more detail in section 4. A constriction effectively increases the confinement in a small amount of space which can be designed to force a row-drop to occur. We can use this to study row-drops for small numbers of rows in thin channels. Additionally, the constriction causes effects seen in viscous fluid flow such as turbulence, stagnation, and chaos. In fig. 5, we simulate a 2D fluid dynamics analogue to the constricted flow channel presented in section 9. Notably, we observe a stagnation of the fluid near to the constriction, surrounded by a fluid vortex; we will see similar effects in our discrete systems.

Given the possibility of chaos emerging, as well the ability to study small numbers of row transitions, the constricted channel shows a variety of physical phenomena, all due to, or dictated by, the constraint of the channel edges and constriction. We present results that show the flow behaviour when it is well-behaved and predictable, and we also show phase diagrams that indicate regions where the system is chaotic.

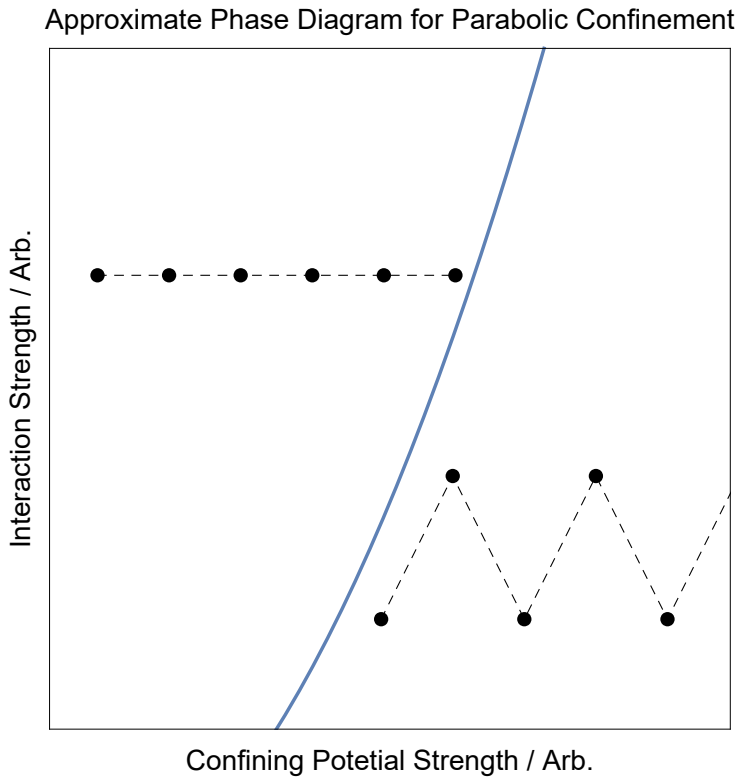

Figure 4: Sketch of a phase diagram for a system of repulsive particles under parabolic confinement. Depending on the values of interaction strength and confinement strength, particles will align accordingly. This sketch shows a representative transition line between a one- and two-chain state. The example we review in section 4 shows transitions between higher numbers of rows as well. This diagram is adapted from the results shown in [89].

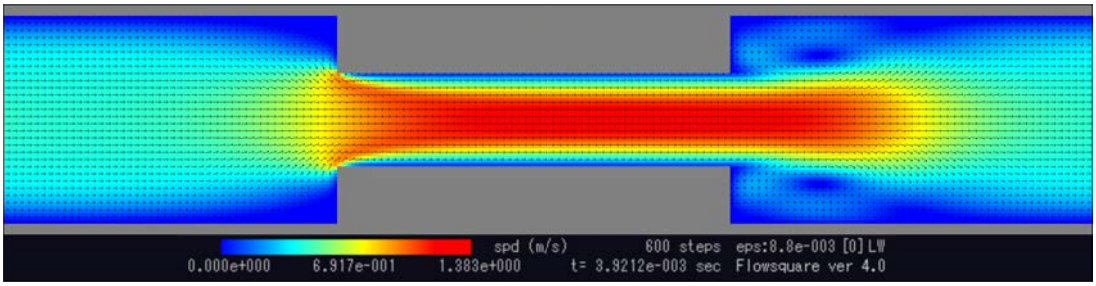

Figure 5: Continuum flow in 2D performed using Flowsquare [2]. The governing equations of incompressible flow [114] are solved to fourth order accuracy on a 304×64 mesh. This snapshot is in a transient phase and is selected to highlight the formation of vortices at the end of the constriction with a stagnation point in the centre where no fluid flows. The flow channel has periodic boundary conditions at the ends of the channel to reflect our systems.

2.3 Vortex Matter as a Tool for Investigating 2D Structures and Flow

The study of vortex matter in superconducting materials began in 1957 with the publication of Abrikosov's seminal work [10]. The magnetic properties of superconductors with a ratio of penetration depth to coherence length, $\kappa > 1/\sqrt{2}$, were found to be due to the quantisation of flux. Tubes of flux, $\Phi_0 = h/2e$, penetrate the material and give rise to encircling vortices of supercurrent.

Vortices exhibit properties that make them strong candidates for a number of different studies: they behave like identical two-dimensional (2D) particles that repel one another. This gives us the opportunity to study equations of motion with lower dimensionality where mass-like terms are all identical; with fewer degrees of freedom, we are more likely to be able to analytically solve certain aspects of the system given the higher symmetry.

We can control vortices to high degrees of accuracy. Techniques like columnar pinning and doping, discussed later, allow us to construct artificial geometries in which to study phenomena. We can show that the channels we construct cause a parabolic potential to leading order (Appendix B).

2.4 Thesis Structure

This thesis continues with section 3 by establishing the physics of superconductors and vortex mechanics needed to understand how and why we are able to study 2D soft matter systems with vortices. We then explore the relevant background and results needed to

motivate the work undertaken in sections 4 and 5. Numerical techniques are described in section 6 which form the foundation for all simulations performed during the research for this project.

The first and second chapters of original research both focus on periodically confined systems, with the aim to understand row changing mechanisms. In section 7, we employ numerical and analytical arguments to develop and solve a system of vortices on a cylinder. Using the knowledge generated, we then validate these results on a cone in section 8 and show how we can control the structure of the flowing vortices by controlling a source and sink reservoir with different vortex densities.

The third chapter of original research is presented in section 9. We show how a thin flow channel with a constriction can give rise to chaos under certain conditions, and we discover that transitions between different flow patterns are chaotic. We also categorise the flow patterns based on the ordering of vortices entering the constriction and their previous position along the channel.

We conclude the thesis by recapping the results and how they fit into previous work. We suggest further investigations to improve certain elements of the research limited by computational resources and time.

3 Superconductivity and the Vortex Lattice

Much of the work in this thesis relies on the physics of vortices in superconductors with novel geometries. In this section, we review the relevant background for vortices in superconductors so we can extract this physics required for simulation. We start by discussing the London approach to superconductivity which provides a basic picture of the physics before proceeding to Ginzburg-Landau (GL) theory, which is a phenomenological theory. We then use the results of GL theory and the London equations to derive the properties of the vortex.

Superconductivity was first observed in 1911 [82]. When the temperature of elemental Mercury drops below a critical temperature, T_c, its resistivity vanishes. The sudden change in resistivity is characteristic of a phase transition which shows a discontinuity in the second derivative of the system's free energy with respect to temperature, T. This is known as a second order (or continuous) phase transition. Defining superconductivity as a perfect conductor (since conductivity is inversely proportional to resistivity) is insufficient. A perfect conductor can also have a constant internal magnetic field that would be unaffected by external fields: this is not the case for a superconductor. The Meissner effect, first reported in 1933 [73], shows that superconductors always expel and screen all magnetic fields below a critical field, B_c. Above the critical field, the superconducting state is destroyed. It is accurate to describe the superconducting state as perfect diamagnetism, with magnetic susceptibility, $\chi = -1$.

A more complicated class (type II) of superconductors were identified in 1957 [10, 107]

where it is possible to minimise the free energy of the superconductor by allowing the partial penetration of an externally applied magnetic field through the sample. This occurs through units of quantised flux which penetrate the sample as a small 'fluxoid', each carrying a flux quantum $\Phi_0 = h/2e$. These fluxoids have the properties we require for this thesis.

Superconductivity is fundamentally a quantum phenomena: the state arises due to the binding of electron pairs on the Fermi Surface (the surface separating occupied states from unoccupied states in momentum space, (p_x, p_y, p_z), at $T = 0$K) via an electron-phonon interaction below a critical temperature, T_c [18]. The bound pairs of electrons are known as Cooper pairs, named after one of the proposers of BCS theory, a field theoretic description of quasi-particle excitations near the Fermi Surface that predict the properties of superconductors. Although powerful, the complete BCS description of superconductivity is not needed to understand the aspects of superconductors that we are interested in. The thermodynamic approach, described by the Ginzburg-Landau free energy of the system, is sufficient, along with an electromagnetic description detailed by the London approach.

We begin by considering the London approach to superconductivity. It is a phenomenological theory that takes an idealised view on supercurrent, applies it to Maxwell's equations of electromagnetism, and derives accurate macroscopic results. Once the London gauge is established, we then consider the thermodynamic approach of Ginzburg-Landau theory. This approach has the London results encoded into it and is useful for understanding vortex physics. Finally, we combine the relevant results to develop a model of the vortex

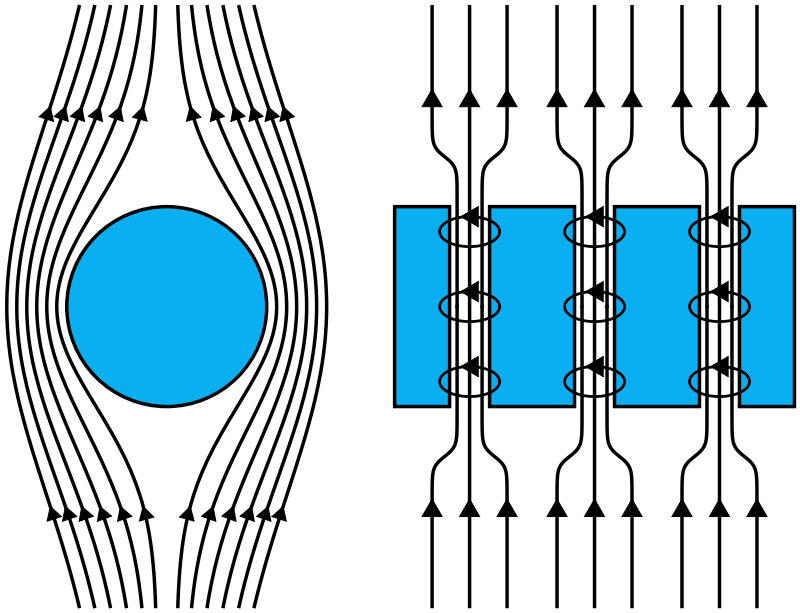

Figure 6: Depictions of magnetic field behaviour in type I (left) and II (right) superconductors. Magnetic field is screened outside type I superconductors (Meissner effect). Partial flux penetration of vortex cores occurs in type II superconductors. Diagrams adapted from [107, §2.3].

and discuss the physics required to simulate these objects.

3.1 The London Approach to Superconductivity

The first theoretical description of superconductivity was developed in 1935 [70] as a phenomenological theory. The London equations described the classical macroscopic properties of superconductors using Maxwell's equations of electromagnetism. We follow the methods presented in [14, 106, 107] throughout sections 3.1 to 3.3. Considering the unimpeded flow of superconducting electrons, we can express the supercurrent, $\mathbf{J}$, as simply:

$$\mathbf{J} = -n_s e \mathbf{v}, \tag{3.1}$$

where n_s is the density of superconducting electrons and $\mathbf{v}$ is the electronic velocity. Applying an electric field, $\mathbf{E}$, causes a force equal to $-e\mathbf{E}$ that accelerates the electrons.

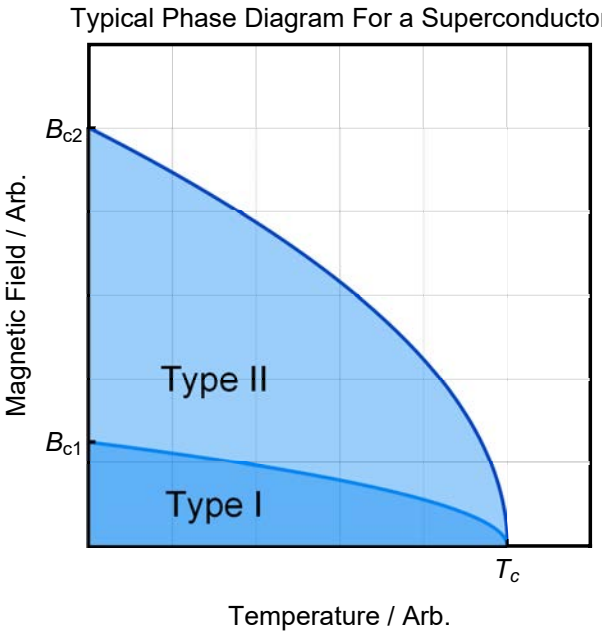

Figure 7: Phase diagram for a typical superconductor. There are two critical fields, B_{c1} and B_{c2}, that correspond to type I and II superconductivity respectively. If $B_{c1} > B_{c2}$ then the material is a pure type I superconductor. Diagram adapted from [14, §3.7].

Using $\mathbf{F} = m\mathbf{a}$ we find the first London equation (relativistic effects are ignored):

$$\frac{\partial \mathbf{J}}{\partial t} = \frac{n_s e^2}{m_e}\mathbf{E}. \tag{3.2}$$

Substituting this expression into Faraday's law ($\nabla \times \mathbf{E} = -\partial \mathbf{B}/\partial t$) yields:

$$\nabla \times \frac{\partial \mathbf{J}}{\partial t} = -\frac{n_s e^2}{m_e}\frac{\partial \mathbf{B}}{\partial t}. \tag{3.3}$$

Note that integrating this with respect to time yields the second London equation:

$$\nabla \times \mathbf{J} = -\frac{n_s e^2}{m_e}\mathbf{B}. \tag{3.4}$$

Equation (3.3) can be substituted into Ampere's law ($\nabla \times \mathbf{B} = \mu_0(\mathbf{J} + \epsilon_0 \partial \mathbf{E}/\partial t)$) after taking the curl and the differential with respect to time and including Faraday's law:

$$\nabla \times \nabla \times \frac{\partial \mathbf{B}}{\partial t} = \mu_0 \nabla \times \frac{\partial \mathbf{J}}{\partial t} + \mu_0 \epsilon_0 \nabla \times \frac{\partial^2 \mathbf{E}}{\partial t^2} \tag{3.5}$$

$$\nabla \left(\nabla \cdot \frac{\partial \mathbf{B}}{\partial t} \right) - \nabla^2 \frac{\partial \mathbf{B}}{\partial t} = -\frac{n_s e^2 \mu_0}{m_e} \frac{\partial \mathbf{B}}{\partial t} - \mu_0 \epsilon_0 \frac{\partial^3 \mathbf{B}}{\partial t^3}. \tag{3.6}$$

Including Gauss's law of magnetism ($\nabla \cdot \mathbf{B} = 0$), excluding the higher derivative by assuming slow time variation, and integrating with respect to time yields the London equation:

$$\nabla^2 \mathbf{B} = \frac{1}{\lambda^2} \mathbf{B}, \tag{3.7}$$

where the London penetration depth, $\lambda = \sqrt{m_e / n_s e^2 \mu_0}$. The London equation is sufficient to explain the Meissner effect; considering a 1D field, the solution is an exponential decay of $B(x)$ as it penetrates a superconducting sample. The penetration depth is therefore an exponential decay constant which characterises the drop-off of magnetic field.

Minimally coupling a magnetic vector potential, $\mathbf{A}$, to the system is a gauge transformation of the canonical momentum:

$$\mathbf{p} = m_e \mathbf{v} + \frac{e}{c} \mathbf{A}. \tag{3.8}$$

Referencing BCS theory [19], the canonical momentum must be zero in the superconducting state. Given this assumption, the expectation value of velocity is:

$$\langle \mathbf{v} \rangle = -\frac{e}{m_e c}\mathbf{A}. \tag{3.9}$$

Referring to eq. (3.1), we find a form of the London equation that will be useful later on.

$$\mathbf{J} = -\frac{n_s e^2}{m_e c}\mathbf{A}. \tag{3.10}$$

3.2 The Ginzburg-Landau Approach to Superconductivity

The Ginzburg-Landau approach introduces a complex 'pseudo-wavefunction', $\psi \in \mathbb{C}$, related to the number density of superconducting electrons, $n_s = |\psi|^2$. This also behaves like an order parameter that describes spontaneous symmetry breaking at a second order phase transition. The pseudo-wavefunction is determined by the solutions to the Ginzburg-Landau equation that is found by considering a free energy density expansion near T_c [106, §10.2]:

$$f \equiv f_s - f_n = \alpha|\psi|^2 + \frac{\beta}{2}|\psi|^4 + \frac{\hbar^2}{2m^*}|\nabla\psi|^2 + \frac{B^2}{2\mu_0}. \tag{3.11}$$

From here on, the subscripts s and n refer to the superconducting and normal states, respectively. The effective mass term, m^*, is the mass of the Cooper pair which mediates the superconductivity. The expansion represents the difference in free energy density, f, between the competing states. The constants α and β come from the series expansion and must be determined. The powers of $|\psi|^2$ are spatially homogeneous terms and appear

in the more general Landau theory of phase transitions. To allow for spatial variation, a gradient term is introduced by including the usual quantum mechanical kinetic energy operator, $\hat{T} = -(\hbar/2m)\nabla^2$. The final term is the energy stored in the applied magnetic field, B. All higher terms are truncated from the expansion for ease of solving; provided the temperature is close to T_c, this method is effective for conventional superconductors.

Minimising the free energy with respect to ψ in the homogeneous regime yields $|\psi|^2 = -\alpha/\beta$. We find $\beta > 0$, otherwise the free energy can be minimised when $|\psi| \to \infty$. The superconductivity is therefore controlled by α, which is not constant. If it is positive, the free energy is negative and the normal state is the ground state ($\psi = 0$). A negative value gives a finite free energy minimum at $|\psi|^2 = -\alpha(T)/\beta$, where α is now a function of temperature, T.

We find $\alpha(T)$ by Taylor expanding close to the transition temperature, T_c. Since at $T = T_c$, $\psi = 0 = \alpha$, we take the next term in the expansion:

$$\alpha(T) \simeq \left.\frac{\mathrm{d}\alpha(T)}{\mathrm{d}T}\right|_{T=T_c} (T - T_c). \tag{3.12}$$

We therefore have the approximate form of ψ:

$$|\psi|^2 \propto T - T_c. \tag{3.13}$$

This tells us that the density of superconducting electrons increases proportionally with decreasing temperature below T_c. This is a statement of a critical exponent of Ginzburg-

Landau theory. Near a phase transition, if a physical property is $\sim \tau^x$, where $\tau = (T - T_c)/T_c$, then x is the critical exponent. For Ginzburg-Landau theory, $\beta = 1/2$ is the critical exponent which describes the wavefunction (our is squared, hence the linearity).

We can relate back to results from the London approach by considering the varying part of ψ. By minimally coupling the vector potential into the free energy, the gradient term becomes [106, §10.2]:

$$\frac{\hbar^2}{2m^*}|\nabla\psi|^2 \to \frac{1}{2m^*}\left|\left(-i\hbar\nabla - \frac{e^*}{c}\mathbf{A}\right)\psi\right|^2 \tag{3.14}$$

$$= \frac{\hbar^2}{2m^*}|\nabla\psi|^2 + \frac{i\hbar e^*}{2m^* c}\left(\psi^*\nabla\psi - \psi\nabla\psi^*\right)\cdot\mathbf{A} + \frac{1}{2m^*}\left(\frac{e^*}{c}\right)^2(\mathbf{A}\cdot\mathbf{A})|\psi|^2. \tag{3.15}$$

The term in $|\nabla\psi|^2$ has no dependence on the vector potential and represents domain wall energies [107, §4.1]. The remaining terms are kinetic energy terms which equate to the current density [107, §1.5]:

$$\mathbf{J} = \frac{i\hbar e^*}{2m^*}\left(\psi^*\nabla\psi - \psi\nabla\psi^*\right) + \frac{1}{2m^*}\left(\frac{e^*}{c}\right)^2\mathbf{A}|\psi|^2. \tag{3.16}$$

Taking the curl of this equation recovers the London equation (since $\nabla\cdot\mathbf{A} = 0$ in the London gauge). We interpret $|\psi|^2 = n_s$ for this to work:

$$\nabla\times\mathbf{J} = \frac{e^*}{2m^*}\mathbf{B}|\psi|^2 = \frac{n_s e^*}{2m^*}\mathbf{B}. \tag{3.17}$$

3.3 The Vortex in a Superconductor

In a type II superconductor, flux can penetrate the sample through localised regions of normal material. This property gives rise to the vortex, which we use as our 2D particles in this thesis.

Consider a superconductor with a hole of normal material. To calculate the magnetic flux trapped in the hole, we integrate the magnetic field over a surface, S [106, §6.3]:

$$\Phi = \int \mathbf{B} \cdot \mathrm{d}\mathbf{S} = \int (\nabla \times \mathbf{A}) \cdot \mathrm{d}\mathbf{S} = \oint \mathbf{A} \cdot \mathrm{d}\mathbf{l}, \tag{3.18}$$

where we use Stoke's theorem to write the surface integral as a line integral. Combining eqs. (3.1) and (3.16), while using the form of $\psi = |\psi| e^{i\theta}$, we find:

$$\mathbf{A} = \frac{1}{2e} \left(\hbar \nabla \theta - 2 m_e \mathbf{v} \right). \tag{3.19}$$

Provided we take the line integral deep enough in the superconductor such that any currents are suppressed to zero, the line integral becomes:

$$\Phi = \frac{\hbar}{2e} \oint \nabla \theta \cdot \mathrm{d}\mathbf{l}. \tag{3.20}$$

In order for the pseudowavefunction to remain single-valued, the integral can take an integer number of 2π:

$$\Phi = n \frac{h}{2e} = n \Phi_0, \tag{3.21}$$

where we have now defined the flux quantum, $\Phi_0 \equiv h/2e$. In order for the pseudowave-function to be single valued, only a quantised amount of flux can pass through a normal region in the material.

It is this quantisation of flux that gives us a system of identical interacting 'particles'. It is possible for vortices with $n > 1$ flux quanta to exist by considering higher winding numbers, but these vortices are typically thermodynamically unstable, with only recent work suggesting stability in multi-component superconductors such as MgB_2 that we do not consider [17, 75]. To have an n-wound vortex would increase the free energy $\sim n^2$ due to the magnetic field kinetic energy terms both having squared terms proportional to n [106, §6.3.1]. All vortices in this thesis are modelled to have one flux quantum.

3.3.1 Vortex-Vortex Interactions

To see how they interact with each other, we convert the London equation into cylindrical polar coordinates (r, ϕ, z) to model the symmetric field of a normal tube of flux passing through a superconductor:

$$\nabla^2 B = \frac{1}{r}\frac{\partial}{\partial r}\left(\frac{1}{r}\frac{\partial B}{\partial r}\right) + \frac{1}{r^2}\frac{\partial^2 B}{\partial \phi^2} + \frac{\partial^2 B}{\partial z^2} = \frac{\mathrm{d}^2 B}{\mathrm{d}r^2} + \frac{1}{r}\frac{\mathrm{d}B}{\mathrm{d}r}. \tag{3.22}$$

Assuming no azimuthal or height variation, the derivatives in ϕ and z vanish and we are left with a 1D differential equation:

$$\frac{\mathrm{d}^2 B}{\mathrm{d}r^2} + \frac{1}{r}\frac{\mathrm{d}B}{\mathrm{d}r} - \frac{B}{\lambda^2} = 0. \tag{3.23}$$

This equation is a special case of the Modified Bessel Equation where the solution is a Modified Bessel Function of the Second Kind, $B(r) = (\Phi_0/2\pi\lambda^2)K_0(r/\lambda)$ [32, §10.25]. This describes the field strength moving radially outward from the vortex core. Despite the Bessel function diverging at $r = 0$, this is still physically accurate since the function is only valid when $r > \xi$, below which there is no superconducting material for the London Equation to describe (only core, which has a constant radial field strength).

Assuming the superconducting material is linear, then the fields from two vortices will superpose. Following [107, s5.1.2], the free energy of two superposed fields will be the sum of the energies of each vortex plus an interaction term, which also has the form of a Bessel function:

$$V_{\mathrm{vv}}(|\mathbf{r_i} - \mathbf{r_j}|) = \frac{\Phi_0^2}{2\pi\mu_0\lambda^2} K_0\left(\frac{(|\mathbf{r_i} - \mathbf{r_j}|)}{\lambda}\right). \tag{3.24}$$

Using this, we can calculate the force between two interacting vortices by differentiating ($F = -\mathrm{d}V/\mathrm{d}r$):

$$\mathbf{F_{vv}}(|\mathbf{r_i} - \mathbf{r_j}|) = \frac{\Phi_0}{2\pi\lambda^3} K_1\left(\frac{|\mathbf{r_i} - \mathbf{r_j}|}{\lambda}\right), \tag{3.25}$$

where $\mathrm{d}K_0(r/\lambda)/\mathrm{d}r = -K_1(r/\lambda)/\lambda$. This interaction force is included in simulations of vortex-vortex interactions performed in this thesis.

3.3.2 Driving Vortices with an Applied Current

Vortex motion can be induced with a Lorentz force by applying an external current, $\mathbf{J}$, to the superconductor [107, §5.4]. The Lorentz force acts perpendicularly to the current and magnetic field lines, so direction can be specified arbitrarily in an experimental set up:

$$\mathbf{F}_{\text{drive}} = \mathbf{J} \times \frac{\mathbf{B}}{c}. \tag{3.26}$$

3.3.3 Viscous Drag for Driven Vortices

The driven motion of the vortices is subject to viscous drag. A vortex driven by a Lorentz force will itself induce an electric field due to the perpendicularity of the magnetic field line and velocity, $\mathbf{v}$:

$$\mathbf{E} = \mathbf{B} \times \frac{\mathbf{v}}{c}. \tag{3.27}$$

Since the core of the vortex is a normal material, the induced electro-motive force is resisted by the material, thus dissipating power [107, §5.4]. A flowing vortex experiences viscous drag with coefficient, η, that couples to the velocity [19]:

$$\mathbf{F}_{\text{drag}} = -\eta \mathbf{v}. \tag{3.28}$$

This drag is important when simulating vortices; the motion is over-damped, leading to negligible acceleration terms. A first order equation thus appropriately describes vortex motion, which we discuss in section 3.3.5.

3.3.4 Thermal Motion of a Vortex

Vortices are also subject to thermal fluctuations. We discuss the consequences of this in section 3.4.1. It is possible to model the fluctuations with a single stochastic term, $\chi(t)$, which has the properties of a normally distributed random 'kick' that a vortex can experience. We discuss the properties of $\chi(t)$ in section 6.2.2.

3.3.5 Equation of Motion for a Vortex

Using the derivations of vortex-vortex interactions, driving force, and drag, we model the motion of a vortex core in a 2D many-body system populated by N_v vortices with the over-damped Langevin equation [66]:

$$\eta \frac{\mathrm{d}\mathbf{r_i}}{\mathrm{d}t} = \sum_{j}^{N_v} \mathbf{F}_{\mathrm{vv}}(|\mathbf{r_i} - \mathbf{r_j}|) + \mathbf{F}_{\mathrm{drive}}(\mathbf{r}, t) + \chi(t). \tag{3.29}$$

This thesis is primarily a numerical study of these equations, performed by simulating this equation with many different boundary and initial conditions. We control N_v and $\mathbf{F}_{\mathrm{drive}}$, along with carefully enforced boundaries, to simulate over parameter spaces. If our software was serially programmed, it would take several years of computational time to complete. As such, we optimise simulations with modern algorithms, including parallelisation, discussed in section 6. Analytical work presented in this thesis is derived from special case systems or idealised cases that do not depend on the details of the Langevin equation.

3.4 The Vortex Lattice

The vortex lattice, also known as the flux line lattice, is the natural thermodynamic state in a uniform superconductor. In this project, we study the deformations of the ideal lattice which are structural, rather than thermal.

The vortex lattice was first predicted by Abrikosov in 1957 [10]. Since vortices repel one another, the natural low-energy state must be that which maximises nearest neighbour distances. Although originally predicted to be a square lattice, Essmann [37] found it to be triangular in 1967. There are exceptions to this, such as Sr_2RuO_4 [54, 98] or ultra-pure Nb [80].

Originally, the lattice was observed using electron microscopy, which involves scanning a fine conducting needle over the surface of the sample and recording the electronic response to the vortices in its proximity. Later, neutron scattering techniques were used [40] which provide very accurate descriptions of a regular vortex lattice, including the square lattice observed in Sr_2RuO_4 [54]. Neutron scattering requires an ordered lattice to produce clear Bragg peaks; the systems we are interested in exhibit mesoscopic behaviour and order that would be cumbersome to observe this way since there are chains of vortices moving amongst a lattice. Scanning Hall probe microscopy also provides single-vortex resolution of the vortex lattice [83].

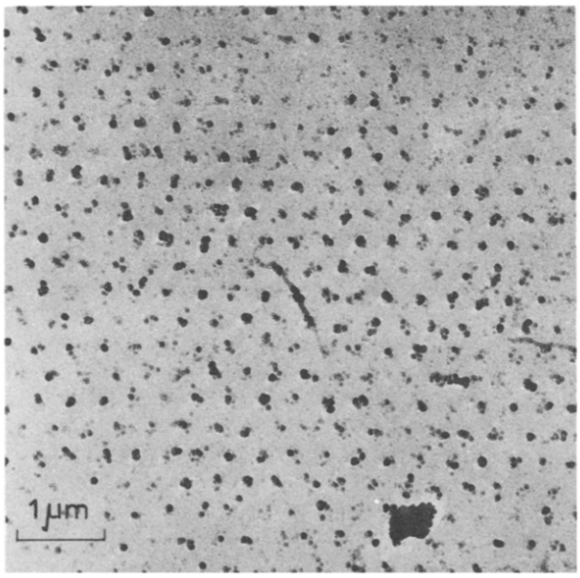

Figure 8: Image taken directly from [37]. The original observation of the triangular flux-line lattice, imaged by electron microscopy on a PbIn rod.

3.4.1 Thin Film Superconductors

Thin films of superconducting material have the ideal properties for a 2D many-body system. The film is set such that the length of a vortex is much less than the average separation of nearest neighbours. This prevents vortices tangling and exhibiting 3D behaviour. Furthermore, thin film superconductors have rich phase diagrams with vortex 'liquid' [45] and 'solid' [28] phases arising from the thermal motion of the vortices. An example of the phase diagram for a thin film superconductor is shown in fig. 9.

The solid phase is the Abrikosov lattice, where vortices tend towards a 6-fold translational symmetry and are well-ordered. For much of this research, we are interested in systems where vortices are deeply in the solid phase, largely unaffected by thermal fluctuations that cause melting, or cause energetically sensitive structures to collapse.

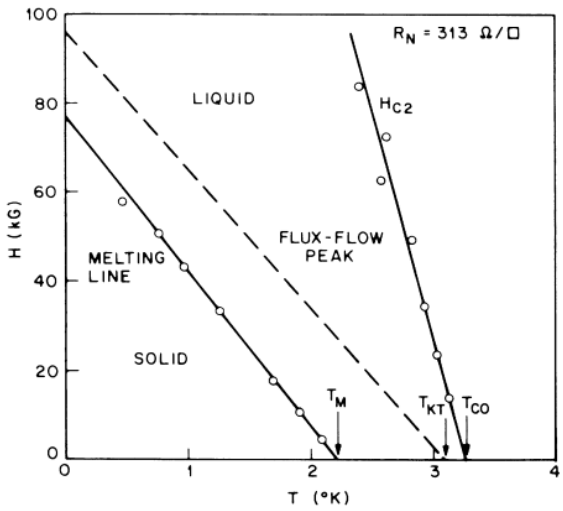

Figure 9: Figure taken directly from [45]. Example of an experimentally derived phase diagram for In/InO_x films. The solid phase exists for the lowest temperatures and field strength and the liquid for higher temperatures and field. Note the absence of the Meissner phase; for a thin film, an external field is unable to be screened by the material since its thickness is less than the penetration depth.

There is a phase transition in the vortex lattice between the solid phase and a disordered liquid phase [123]. They are often observed in high temperature superconductors, such as $Bi_2Sr_2CaCu_2O_8$, as thermal fluctuations in 2D cause vortices to displace from their energetic minima on the hexatic lattice. Dislocation pairs of vortices, one with five and the other with seven nearest neighbours, form and unbind from one another. This unbinding is predicted to be a Kosterlitz-Thouless (KT) transition [39, 48]. The KT transition is an unconventional phase transition in 2D where the free energy of the system is infinitely differentiable at the transition temperature. Regular phase transitions typically have discontinuities in the first or second order derivatives of the free energy.

Strictly speaking, the melting transition and many of the structural transitions we observe in this thesis are not true thermodynamic phase transitions. Firstly, the number of particles is of the order of hundreds, far below Avagadro's number for statistical physics

to be an accurate description. Secondly, due to the soft nature of the vortex lattice, the response of the lattice due to local fluctuations can be much slower than a thermodynamic material. Thirdly, many of these simulations are at zero temperature, which means that thermal fluctuations are non-existent (numerical noise will still persist, however). Conveniently, at zero temperature, the free energy of the system is the internal energy, which is a crucial assumption made in section 7.

The Mermin-Wagner theorem [74] forbids long range order in lattices of dimension $d \leq 2$ at finite temperature. This is not an issue in the systems we study since the systems are finite size and small; Mermin-Wanger assumes an infinite system.

Experimentally, thin film superconductors and the induced vortex lattice have been intensively studied. Figure 9 shows a phase diagram from a study of In/InO_x films, where the material is a conventional low-temperature superconductor. These materials are typically cooled to below 5K where they start to exhibit superconducting properties, vortex lattice melting, and the KT transition [45].

An alternative material to use is a-Nb_3Ge, which is amorphous [23]. When the atomic structure of the material lacks long-range order, due to being amorphous, vortex pinning due to lattice effects is reduced [22]. Layering this compound with NbN, which is prone to vortex pinning, and etching a channel through it, leaves a highly pinned channel edge controlled by the NbN and an easy-flow channel on the NbGe substrate. We discuss this system in detail in section 4.3.1.

3.5 Remarks

We have established the vortex as an ideal candidate for studying 2D many-body physics on thin-film superconductors. From herein, we treat them as 2D point like objects that repel one another, are subject to thermal fluctuations, and can have externally applied forces acted upon them.

In the next section, we discuss their applications to narrow and wider flow channels. Then, in section 6, we discuss how we computationally model vortices in many-body systems.

4 Confined Channels in Soft Matter Systems

In this section, we will review the literature on confined channels of repulsive soft particles. We pay particular attention to systems and results relating to row transitions that underpin the research we undertake.

One such system is a parabolically confined channel of Yukawa particles that one can solve the structural phase diagram for. The methods used in the original paper [89] are reviewed and we repeat the calculations to reconstruct the phase diagram. The methods are then adapted in section 7 in an adapted way which means we can solve structural ground states on the cylinder.

We also discuss the form of the potential when pinned edge arrays of vortices are used to confine flowing vortices inside the channel. The confinement gives rise to non-linear waves known as solitons and exhibits a one-to-two chain transition known as the zig-zag transition.

We finish by discussing experimental examples of confined systems that exhibit row transitions and other related properties that arise in our systems.

4.1 Parabolic Confinement

A standard way to confine a system of soft particles in 2D is with a parabolic confining potential, $V_{\text{conf}}(x, y) \sim y^2$. The potential has a minimum along the line $y = 0$, hence a

vertical displacement of particles corresponds to an increase in energy and only arises due to interactions with other particles. The seminal study on this topic [89] studies Wigner Crystals under parabolic confinement and introduces fundamental ideas that we use in our approaches in similar systems. Firstly, if the system of particles is not subject to thermal noise, the energy can be written in terms of summations over rows of vortices that can be mathematically expressed as a set of chains of particles. Secondly, using mathematical descriptions of different numbers of chains, one can perform energetic sampling routines to optimise the structures and find the ground state.

At zero temperature, one needs only to consider the energetic competition of interactions and confinement to calculate structural ground states. The general Hamiltonian for such a system can be expressed by:

$$\mathcal{H} = \sum_{i}^{N} \sum_{j \neq i}^{N} V_{\text{int}}(|\mathbf{r_i} - \mathbf{r_j}|) + \sum_{i}^{N} V_{\text{conf}}(y_i). \tag{4.1}$$

The interaction potential for a Wigner Crystal is a Yukawa Potential [116]: $V_{\text{int}} = e^{-\kappa|\mathbf{r_{ij}}|}/|\mathbf{r_{ij}}|$, where κ is the interaction strength coefficient. If one knows the configuration of particles for a specific density, ρ, then this Hamiltonian can be calculated to computational precision. If the system is a theoretically infinite-length channel, then a per-particle energy can be calculated instead. This idea of applying a per-particle energy is used in section 7. If one then knows all possible configurations, then different energies can be compared to find the ground state for a particular point on the phase diagram.

The parabolic channel has an overriding horizontal symmetry that forces one or more

rows of particles to align along the x-axis. Figure 1 in section 2 shows examples of three different states of parabolically confined chains that align along the x-axis. Assuming particles are evenly spaced on individual rows which are exactly out of phase with neighbouring rows (a local triangular arrangement), the state can be parametrised in terms of row separation. For example, a three-chain state has a regular array of particles along $y = 0$ and two rows at $y = \pm Y$, where the optimal value of Y that minimises the energy of this particular chain needs to be determined numerically. Each chain hosts a third of the particles, so for a density, ρ, the particle separation on each chain is $3/\rho$. For a choice of ρ and κ, the optimal value of Y is found for the three-chain state along with corresponding heights for one, two, four, and higher numbers of chains. With each state optimised, the one with the lowest energy is the ground state.

Since, in principle, any number of rows of particles could be the ground state at a given point on the phase diagram, we need to know what a reasonable number of chains to consider is. This is best done by initially simulating confined particles to get an indication of how many chains should appear in the parameter space, as well as a general trend for the progression of rows. An extreme argument can be made by considering what happens at low density: particles are so far apart that their interactions are negligible and positioning at any finite height will increase energy, so a single chain is optimal. Molecular Dynamics and Monte Carlo simulations readily confirm this. Increasing density shows the single chain bifurcates into a two-chain configuration via a zig-zag transition [25, 30, 31, 44, 65, 71, 87, 89, 103, 119]. In section 4.2, we review the zig-zag transition in more detail.

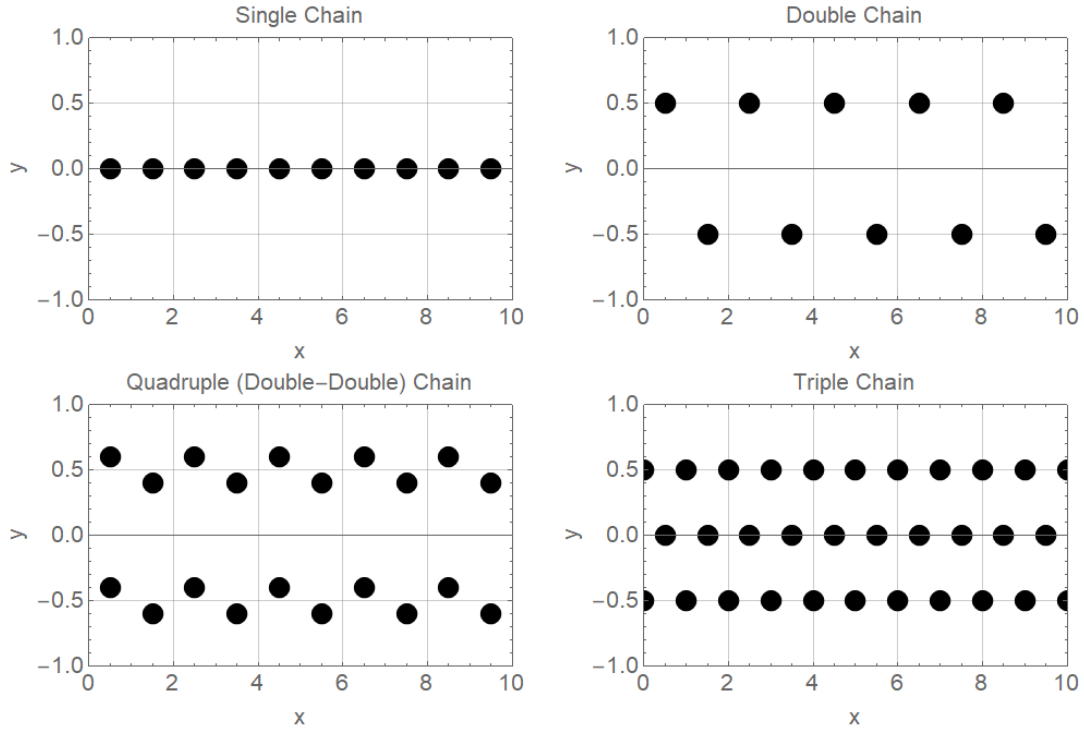

Figure 10: Examples of static chains of particles. The single chain bifurcates into the double chain via the zig-zag transition at a critical confinement. Eventually, each chain in the double chain system individually bifurcates to form four chains. A realignment then occurs and the four chains merge into three [89]. The x and$y$ axes represent the 2D position of each particle.

The two-chain state then has a 'double zig-zag' transition where each chain bifurcates into a total of four chains. As density increases, the middle two chains merge to a three-chain configuration and eventually reform to a four-chain state. These states are illustrated in fig. 10. There is a general trend of increasing row number observed with increasing density. By initially simulating different densities and potential strengths, we generate a course grained phase diagram, which indicates that the maximum number of chains we will observe is 6. We repeat the numerical calculations performed in [89] by considering up to 10-chain states and find this sufficient to generate the portion of the phase diagram published.

Since the ground state is a chain of evenly spaced particles, the energy per particle can be expressed by calculating a series of summations. For example, in the single chain, each particle has total energy [89]:

$$V_1 = \sum_{i \neq 0} V(i/n_L). \tag{4.2}$$

This is because each particle should be evenly spaced along the line $y = 0$. With a number of particles per unit length, n_L, the spacing is the reciprocal of it. The case $i = 0$ is omitted since it is a self-interaction term. Wigner Crystals are modelled with a Yukawa potential: $V(r) = e^{-\kappa r}/r$.

The energy per particle of the 2-chain state is similar in construction [89]:

$$V_2 = ky_0^2 + \sum_{i \neq 0} V(2i/n_L) + \sum_i V(\sqrt{((2i+1)/n_l)^2 + 4y_0^2}). \tag{4.3}$$

Here, each chain is at a height of $\pm y_0$. The first term is the parabolic potential energy gain of separating the single chain. The second term is the interactions with particles on the same chain as the one being considered. The third term is the interactions with the opposite chain which is displaced out of phase along the y axis and separated by a distance of $2y_0$.

For a given value of κ and n_L, either $V_1 < V_2$, $V_1 > V_2$, or $V_1 = V_2$. Each case corresponds to:

- The single chain is energetically favourable when $V_1 < V_2$.
- The double chain is energetically favourable when $V_1 > V_2$.
- The transition point between the two states occurs when $V_1 = V_2$.

Numerical testing is implemented to map out the phase diagram for this system.

For higher numbers of chains, the energy per particle is more complicated due to the loss of translational symmetry between chains. A weighted average of energies a particle has on each chain is thus used. For more than one chain, the energy must first be numerically minimised to find the optimal value of chain separations. For example, one must search for the optimal value of y_0 for the double chain. Naturally, $y_0 = 0$ corresponds to the single chain. For other chains, additional separation distances are minimised over, and the minimisation becomes a $\lceil n/2 \rceil$-dimension problem for n chains, making the calculation significantly more time-consuming for large numbers of chains.

In Section 7, inspired by the method of mathematically constructing states on an infinitely long system, we generate a set of phyllotactic structures that we sample and search amongst for the ground state. We assume homogeneity in a similar context to this work by ignoring any possible defect or dislocation effects and confirm its validity with Molecular Dynamics and Monte Carlo simulations. Since the system has strong translational symmetry between sites, we only consider single summations without weighted averages for each state.

We test the validity of the method of state construction and sampling by repeating the

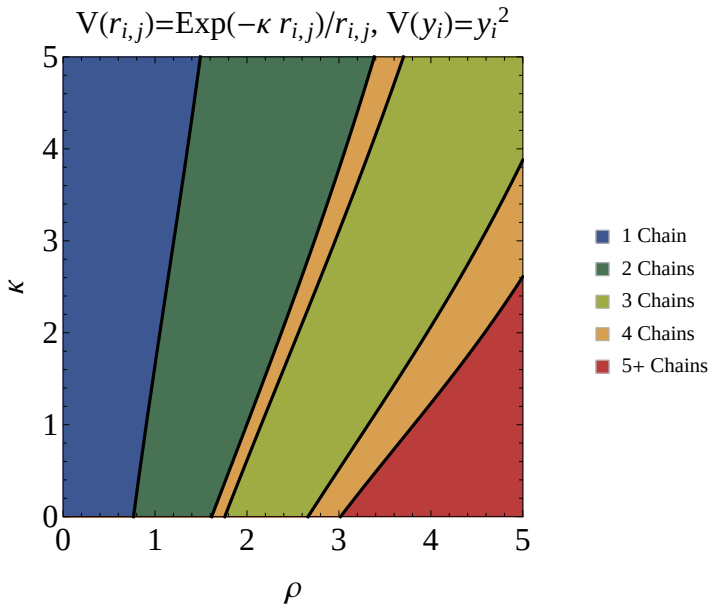

Figure 11: Independent verification of the results and model presented in [89] for a range of densities $0 < \rho \leq 5$ and interaction strengths $0 < \kappa \leq 5$. Following the scheme of numerical optimisation, we find ground states consisting of up to 5 chains of particles in this particular parameter space.

calculations in [89] and find complete agreement with their work. We are thus confident that this method is effective in the system we investigate.

4.2 The Zig-Zag Transition

The zig-zag transition is the simplest row transition because of its mechanisms and mathematical descriptions. Higher row transitions include many variables and additional complications like twisting and reorienting [42, 43]. The zig-zag transition is characterised by the alternating separation of particles on a single row to equal and opposite heights into the confining potential. This transition is unique amongst row changes since it is the only 'continuous' transition. Caution is taken when discussing continuous transitions in zero temperature mesoscopic systems because particles cannot thermalise and undergo

a true thermodynamic phase transition. Due to this, it is possible to make a continuous transition appear discontinuous in particular symmetric cases such as this. Previous work presented in [109], as well as work on transverse diffusion at the zig-zag transition [29, 31, 103], indicates long time scales associated with the transition, due to the slow growth of numerical fluctuations that drive the transition. In appendix A.5, we show that beyond the transition point, the single chain becomes energetically unstable and requires a symmetry breaking mechanism (numerical noise is sufficient) to cause the bifurcation to occur. Our previous results indicate there are two time regimes during this process, one where the growth of the mean square displacement $\sim t^{0.25}$ and another where growth $\sim t^2$. This is unlike the other cited studies, although our simulations were performed at zero temperature which may account for the unusual (and arguably un-physical) behaviour.

All other transitions are discontinuous due to additional requirements of realignment giving an effective 'latent heat'. Particles have to dramatically realign in order to transit, and the energy required for this must come thermally for the system to escape its meta-stable minimum [89].

4.3 Periodic Potentials from Vortex Confinement

The confining potential can be modulated along the x-axis. This can be due to creating the confinement with a regular array of vortices which generates periodic minima and maxima along the channel. This sinusoidal effect creates a length scale in the channel which causes numerous flow effects, the most well-known being soliton flow [23]. Aspects of the research in this thesis are strongly confined and periodic, so we need to understand

the key observations of these systems in order to identify similarities and differences with our results.

4.3.1 Systems of Confined Vortices

Vortices in flow channels have been studied extensively; numerical studies of vortices are experimentally viable and there are several studies we review in this section highlighting this. They can be pinned via material doping by adding impurities at pinning locations to force a normal region which a vortex will form around [72]. Alternatively, 'columnar defects' [26] can form in high-T_c superconductors such as YBCO ($YBa_2Cu_3O_7$, where a beam of radiations causes the crystal structure to deform. The superconductivity in YBCO is dependent on layers of copper-oxide planes [124]; where the columnar defect passes through these planes, the superconductivity breaks down.

Typically, two thin-film superconductors are layered together with a channel etched into the upper layer. The upper layer is tuned to be in a vortex 'solid' phase, whereas the lower layer is in a 'liquid' phase. Pinned vortices on the solid layer lock the field below it on the lower layer, except for in the etched region, where vortices can flow and interact with pins.

4.3.2 Solitons in Modulated Narrow Channels

It has previously been shown that an incommensurate number of flowing vortices, with respect to pinned vortices, causes solitonic flow [23]. For example, if each vortex assigns a potential minimum to itself and there is one vortex too many, that vortex will form the

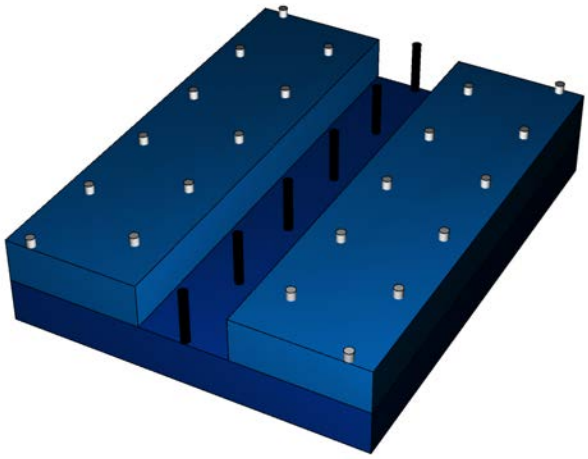

Figure 12: 3D rendering of the etched channel, adapted from [23, 108, 109]. The upper layer consists of a pinned array of vortices that cause vortices to pin directly below the layer. The etched layer is unpinned and vortices can move freely in the channel, interacting with pinned vortices via the vortex-vortex interaction.

core of a soliton which causes a local distortion of the chain which is able to flow at a different rate to the chain. This is a non-linear effect and the form of the soliton is found by solving the Sine-Gordon model for the relative displacement, $u(x,t)$ of each vortex [63]:

$$\frac{\partial^2 u}{\partial t^2} - \frac{\partial^2 u}{\partial x^2} + \sin(u) = 0. \tag{4.4}$$

The basic soliton solution is a localised 'kink' in the flowing chain [49]:

$$u(x,t) = \tan^{-1}\left(e^{x-\beta t}\right). \tag{4.5}$$

The value of the coefficient, β, determines the speed of the soliton. Although of specific interest in thin periodic channels, we present results that show solitonic flow in a density gradient as a feature in section 9. Our previous work [108] studied narrow channels with uniform density; results in section 9 shows solitons can form in more general systems with

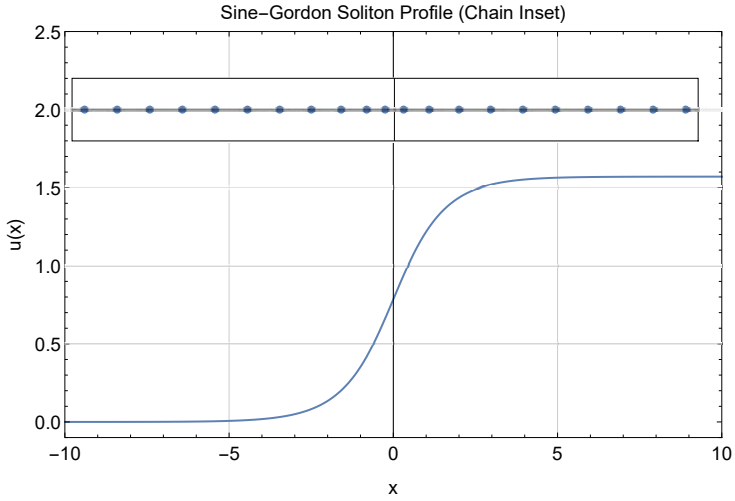

Figure 13: Example of a soliton with $u(x) = \tan^{-1}(e^x)$. The chain with a soliton is inset; vortices' original, regularly placed, positions are displaced subject to $u(x)$.

non-uniform density.

4.4 Experimental Examples

As well as being computationally accessible, much experimental work exists on this subject. The earliest work [91] studied the usual NbN/a $-$ Nb_3Ge materials with multiple etched channels of width 90nm. The strong pinned NbN layer is 50nm thick and the weakly pinned a $-$ Nb_3Ge is 550nm thick. The experiment consisted of 200 of these channels, separated by 10μm, and measurements of the shear modulus, c_{66}, were made which gives insight into the movement of layers of vortex rows over one another. This work led to many more studies on vortex flow channels, some of which we discuss in the remainder of this section.

Work on a $-$ MoGe, another amorphous material, investigates wider channels (approximately six rows of vortices) of varying trench depths [90]. Using a scanning superconducting quantum interference device (SQUID) microscope to image vortices, they were

able to measure the vortex density near to the trenches. This imaging method is another possible way to measure experimental data in implementations of vortex flow.

Vortex flow through thin channels (up to three or four rows of vortices) was successfully implemented in [55]. By increasing the density of vortices, they observed a relationship between transport current with field that modulated as the number of rows increased. A row-gain transition indicates the turning point of critical current because the dislocation pair associated with it causes a jamming phenomena. It is this jamming effect that we are interested in with the constricted flow channel and row-drops in section 9. In our system, the jamming is due to multiple rows of vortices all merging to the same row, similar to the observations made in these experiments and simulations.

Row transitions have been observed in similar systems. Experimentally, an $n \rightarrow n+2$ transition is observed due to field focussing into the etched channel that brings in additional vortices from either side as driving force increases [58]. This effect is not included in any of our models since we are more interested in the pure behaviour of repulsive particles in novel geometries. Work on $NbSe_2$ films [52] derived a phase diagram for row transitions as a function of field and film depth when a ferromagnetic strip is used as the 'channel'. Using the thin strip of $Fe_{20}Ni_{80}$ forces vortices to form only where the strip is, thus creating a channel. A range of rows from one to seven are presented in the experimentally derived phase diagram. This result is in line with other studies in that vortex rows are dependent on magnetic field strength and channel geometry.

An experimental example of $n \to n-1$ transitions [61] reports, that for a superparamagetic colloid being driven through a channel under the force of gravity, a density gradient forms and row transitions occur similarly to the original system we are interested in.

Studies also exist on multiple layers of superconductor that produce rich phase diagrams and structures [59]. It is possible to form chains of vortices of various row numbers by controlling the magnetic field and temperature to change the coupling between layers. Although quite far away from our interests, this work highlights the range of systems where vortex rows appear.

Outside the field of soft matter, vortices in Bose-Einstein condensates in trapping potentials have shown zig-zag transitions, as well as more radially-symmetric structural transitions [69]. It is also possible to study chain bifurcations and soliton formation in chains of cold atoms [85]. By trapping $^{132}Yb^{+}$ ions in a radio frequency (Paul) trap [86] and changing the strength of the trapping potential, a zig-zag transition can occur. Commensurability of the modulated trapping potential can also cause a kink to form between the two bifurcated chains. This phenomena has also been reported in previous work [108] in the vortex channel.

4.5 Remarks

Having reviewed the literature on discrete confined flow channels, we have highlighted some crucial points:

- Wide flow channels with a density gradient exhibit row-drop transitions along the

length of the channel.

- For homogeneous systems under parabolic confinement, we can numerically optimise chain structures to find structural ground states at zero temperature.
- In narrow modulated flow channels, solitons form and flow through the system.
- There are several experimental options, including vortex matter systems, for realising these systems.

Our results and methods draw on these main points in the results sections. Since we study a unique form of confining vortices with a periodic boundary condition, we continue our literature review in the next section on cylindrically confined system.

5 Cylindrical Confinement in Soft Matter Systems

Previous work [111, 112] has established the importance of the boundaries in narrow channels. The geometrical properties of these boundaries dictate the structures that are observed in the channel and the dynamical response to a driving force. It is beneficial to separate the narrowness and the boundaries from each other in the channels to investigate the effects of just one. We elect to concentrate on a cylindrical geometry, since we are able to focus on the width of the channel. Structures and responses that are not observed in this system can be attributed to the effects of boundaries alone.

We study a system on a substrate with the same properties as an infinitely long cylinder or torus (a finite-length cylinder with an additional periodic boundary condition). Although parabolic confinement can be used to trap vortices in the vertical direction, it is possible to study systems where the confinement is a periodic boundary condition in the vertical direction. This geometry is useful primarily because it enables us to examine the properties of vortex lattice flow in the confined channel without any boundary effects caused by pinned edge vortices. The cylinder also removes GNDs by design.

Cylindrical systems are abundant in nature [36] and we use the standard notation of phyllotaxis to describe the positions of petioles on plant stems [11] to denote the structural states we observe.

In this section, we review the literature on related systems to develop the background knowledge required to understand the system and results for cylindrical confinement in

sections 7 and 8.

5.1 Cylindrical Confinement of Hard Spheres and Disks

Much of the recent work on cylindrical confinement involves the study of hard disks [46, 57, 78]. Disks interact via hard-wall boundary potentials, as illustrated in fig. 14, on their circumferences only. The focus of these studies is to solve the optimal close-packing problem, which is purely geometric since disks can not overlap and there are no interactions that extend beyond a disk's size. A lattice on the cylinder is generated which repeats cyclically along the poloidal direction. It is described by the phyllotactic notation and the scheme is as follows (also depicted in fig. 14):

- Choose any node on the lattice at a point, $\mathbf{r_0}$.
- Define the periodicity vector, $\mathbf{V}$, to be the translation vector from $\mathbf{r_0}$ to the first repeated copy of the initial node, $\mathbf{r_1}$. Typically, $\mathbf{V} = \hat{\mathbf{y}}c$ where c is the circumference.
- Identify the smallest two primitive lattice vectors that define the lattice, $\mathbf{a}$ and $\mathbf{b}$. The next largest vector, $\mathbf{c}$, will either be equal to $\mathbf{a} + \mathbf{b}$ or $\mathbf{a} - \mathbf{b}$.
- A triangle of these three vectors is then constructed such that the same number of each is used and the side consisting of that many $\mathbf{c}$s coincides with $\mathbf{V}$.
- The Phyllotactic notation is $[l, m, n]$ where l is the number of each vector used to construct the triangle. Depending on the definition of $\mathbf{c}$, m and n are defined by: $\mathbf{V} = l\mathbf{a} + m\mathbf{c}$ and $\mathbf{V} = l\mathbf{b} - n\mathbf{c}$ or $\mathbf{V} = l\mathbf{a} + n\mathbf{c}$ and $\mathbf{V} = l\mathbf{b} - m\mathbf{c}$.

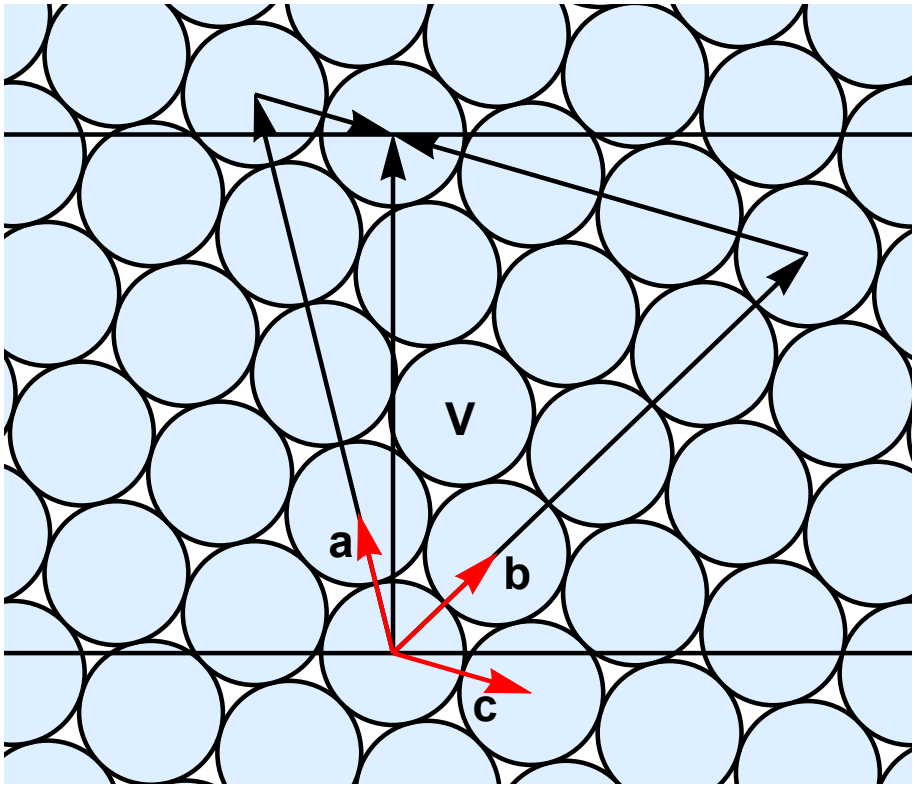

Figure 14: Example of a $[4, 3, 1]$ state as defined by the stated scheme. A total of 4 of each vector, $\mathbf{a}$, $\mathbf{b}$, and $\mathbf{c}$ are needed to draw the triangle that coincides with $\mathbf{V}$. The translation vector from $4\mathbf{b}$ to $\mathbf{V}$ is $-3\mathbf{c}$ and the translation vector from $4\mathbf{a}$ to $\mathbf{V}$ is $1\mathbf{c}$. The 4, 3, and 1 are combined in descending order to give $[4, 3, 1]$. The horizontal lines represent the repeated boundary which describes the system. This diagram is adapted from a similar figure presented in [78].

This scheme omits cases of a 'line-slip' boundary, where the close packing problem is optimised by including a dislocation that breaks the translational symmetry of the lattice. Line-slips frequently occur in hard disk systems; conveniently, however, they are not included in the vortex system due to the differences in repulsive interactions and hard-wall boundaries.

The phyllotactic notation can be interpreted as a set of rows of particles, tilted at a common angle along the poloidal direction. This brings a comparator to the regular vortex flow channels for which rows, and row-reduction mechanisms, are of interest.

The most relevant studies to our work involve packing hard spheres in tubes [76]. Since the structure is controlled by the size of the spheres and the diameter of the cylinder, the phase diagram can be plotted in terms of the ratio of the spherical diameters to the cylindrical diameter, which scales out one of the parameters [77]. A rich range of phyllotactic states are observed, typically showing a structural progression of distinguishable rows in a sequential order, starting from a single straight chain, to a zig-zag, then to higher numbers of chains, as the ratio increases.

The ground state structures of hard spheres are found by simulation and annealing. Line-slip phases are frequently observed since the spherical hard-walls mean that positions can not smoothly fill the cylinder, allowing grain boundaries to form. This is a property that we ignore in our models; repulsive point-like particles should be able to fill any substrate homogeneously, and we demonstrate this with simulations in section 7. Analytic work on hard disks shows that line-slips occur because their rhombic counter parts (i.e. if the line-slip was shifted to make the lattice regular) are unstable [78].

Additional studies of hard spheres study wider cylinders and serve to confirm the validity of previous results [41]. Because spheres lie inside the surface structure, the phase diagram is more complicated, although still shows a general trend of increasing row number with the cylinder-sphere diameter ratio.

A contrary result that suggests line-slips are possible is presented in [118]. By simulating

Lennard-Jones particles confined to a cylinder, they observe some line-slip structures that emerge due to the relaxation of strain on an otherwise uniform structure. We note that these simulations were at finite temperature and this additional free energy is enough to allow a line-slip phase to form. In our systems at zero temperature, these phases are not observed.

Yukawa particles confined in a cylinder show phyllotactic and helical phases [84]. There are no line-slips reported in this study of direct line-of-sight interacting particles (interactions are in 3D, rather than around the cylindrical surface in 2D). Again, a progression of increasing chain numbers is observed as the density of particles increases, an effect also reported in [111, 112].

A study more relevant to the conical geometry we investigate in section 8 shows that by considering the local geometry of a changing diameter, one can construct the optimal packing of disks by combining various local structures together algorithmically [79]. This generates a set of different phases along the geometry, similar to the separated phases we observe in section 8. An interesting observation made in this system is that the number of rows in each separate phase varies as a Fibonacci sequence when the diameter varies as a Tanh function. i.e. as diameter increases and row transitions occur, the number of rows changes from $1 \to 2 \to 3 \to 5 \to 8 \ldots$. Our cone is a linearly varying system and the Fibonacci sequence evolution is not observed. Our methods do not use this modern technique, although it is an area of future research that should be investigated on the simple cone.

5.2 Experimental Studies

A number of experimental studies exist that examine cylindrical confinement from different perspectives. An excellent candidate for a cylinder is the carbon nanotube - a cylindrical arrangement of carbon atoms comprising of a 'rolled-up' sheet of graphene. Work presented in [56] shows how filling nanotubes with bucky-balls (C_{60}) generates helical arrangements of the molecules. Zig-zag phases are observed, including helical versions, similar to those reported in [84].

Larger versions of the nanotube/C_{60} are studied in [120]. Again, ordered arrangements were observed, consistent with the phyllotactic notation.

More recent work [67] observed ordered structures of polystyrene-tethered gold nanoparticles in cylindrical nanopores of anodic aluminium oxide. Golden cores coated in polystyrene are able to remain in strong contact with the nanopore due to the brush-like strands of polymer attached to them. The anodic aluminium oxide has a hexagonal close packed structure of nanopores, ideal for a cylindrical confinement study. Electron microscopy techniques show a range of phyllotatic structures from single chains up to tens of helical rows of nanoparticles.

Although these experiments are direct line-of-sight interactions, phyllotactic structures are still present. Although our work will study interactions around the surface of the sub-

strate, it is reassuring to know that the results should be similar to previous experiments.

5.3 Remarks

In order to establish an effective mapping between cylindrical and pinned confinement, this thesis contributes to the body of work on the related phase diagram for cylindrically confined vortices. The lack of line-slips simplifies the problem, but we also find additional features that enable us to make analytic progress with the problem to the point where we consider it fully solved. Using the techniques developed in the analysis, we extend the system to a cone-like structure, where we can establish single-phase flow over the entire system, eliminating dislocations and grain boundaries. By demonstrating the ability to control row-changing mechanisms in a density driven channel, we are able to suggest why they occur in the pinned systems.

6 Computational Simulation of 2D Vortex Matter Systems

This section presents an overview of the numerical methods employed in this thesis. We highlight areas where care must be taken and justify the choices we make when setting up the systems.

Simulations and analyses are performed using the C++ programming language and the Wolfram language for Mathematica [8]. C++ provides an effective basis for simulating vortex matter systems and is easily scalable to parallel processing techniques using the Intel Compiler [3].

The systems studied in this project are predominantly non-linear, stochastic, and many-body. Analytical methods, although useful, often follow from established results where we find justifiable approximations used to solve for some set of dynamics. For example, our own work uses numerical results to underpin the assumptions we take forward into an analytical description of phyllotactic states on the cylinder in section 7. Data that we consider 'physical' either comes from experiment or simulation and is used to direct analytical methods that lead to a deeper understanding of the physics. We rely on simulation data in this study because many of the systems are idealisations of realisable experiments or require modifications to system parameters that would otherwise involve the re-fabrication of samples.

Given we are interested in effects caused by very specific boundary conditions, simulations are performed at zero temperature or with perfectly rigidly pinned edge vortices.

Although the physicality can be brought into question, since $T = 0$K is unobtainable and pinned vortices do fluctuate in their positions [23], we study these idealised systems in order to understand the unperturbed physics of the system.

We simulate many more systems than we present data for in this thesis. This is because many of our simulations are run to probe parameter spaces to highlight any novel physics, as well as repeating simulations, where possible, to ensure our results are accurate. We also aim to generate fine-grained data so we can perform accurate analyses; simulating parameter spaces at high resolution significantly increases the number of simulations we need to perform. Our high computational demands are met by a local high-performance cluster: BlueBEAR.

6.1 High-Performance Cluster Computing

Running the code for this project on local workstations is impractical due to analysis bottlenecks due to long simulation times. Access to high-performance computing nodes significantly reduces this bottleneck by offering many more nodes to run simulations that are typically clocked at higher speeds than what is available locally.

The University of Birmingham hosts a High-Performance Cluster (HPC) known as BlueBEAR. In the generation used during this project, up to ten Intel Xeon E5-2660 processors can be utilised at once to provide 160 threads of parallel processing capability. Jobs can be submitted in batch and are automatically scheduled to run based on the needs of other

users on the network.

6.2 Molecular Dynamics

The most common way to numerically study the real-time dynamics of a many-body physical system is with Molecular Dynamics (MD) methods. The term originally refers to studying systems of atoms or molecules, either classically or quantum mechanically, but can be extended to particles with more general properties, like the vortex. There are numerous MD algorithms used for different purposes such as Runge-Kutta methods, or the Velocity Verlet algorithm [105]. The algorithms are designed to accurately simulate many-body motion in arbitrarily complex systems; depending on the desired accuracy, higher order methods can be implemented to study precise phenomena.

Our choice of integration routine is in line with the numerical studies of vortex matter referenced in this thesis, we use the the Runge-Kutta algorithm [23]. Since the Langevin equation is over-damped, only first order derivatives exist, removing the requirement of methods developed for higher-order terms such as Velocity Verlet.

The Langevin equation is used in many molecular dynamics studies of vortex matter [24, 33, 94, 95, 97, 111]. For the position of the i^{th} vortex, $\mathbf{r_i}$, we solve the over-damped Langevin equation:

$$\eta \frac{\mathrm{d}\mathbf{r_i}}{\mathrm{d}t} = \sum_j \mathbf{F}_{\text{vv}}(|\mathbf{r_i} - \mathbf{r_j}|) + \mathbf{F}_{\text{EXT}}(\mathbf{r}, t) + \chi(t). \tag{6.1}$$

The vortex-vortex interaction, $\mathbf{F}_{\mathrm{vv}}(\mathbf{r}) = \hat{\mathbf{r}}K_1(|\mathbf{r}|/\lambda)$, is the usual Bessel function derived in section 3.3.1. The dissipation coefficient is given by η that we usually set to unity. An external force, $\mathbf{F}_{\mathrm{EXT}}(\mathbf{r}, t)$, can be applied to the system, typically as a uniform drive. The stochastic term, $\chi(t)$, represents a thermostat that controls the temperature of the system. Although we are primarily interested in zero-temperature results, the system must usually be annealed to $T = 0$ in order to ensure the correct ground state is obtained. Simulated annealing is discussed in section 6.4. Since the motion is dissipative, a thermostat is used to maintain an energetic equilibrium by supplying noise to the vortex velocity. A full description of the thermostat is given in section 6.2.2.

A useful optimisation is to use a simplification of the Bessel function that introduces a cut-off radius of interaction, r_c [62]:

$$F_{\mathrm{vv}}(r) \simeq \frac{1}{r}\left(1 - \frac{r^2}{r_c^2}\right)^2. \tag{6.2}$$

This causes the interaction to drop to zero at the cut-off since $F_{\mathrm{vv}}(r_c) = 0$. We set $r_c = 3.33$, in line with previous studies [23, 62]. Qualitatively, results between using this force and the full Bessel function should be quite similar since the closer-range interactions are dominant over long-range interactions. At the cut-off, the interaction strength is 5% of the strength of nearest neighbours on the lattice: $K_1(3.33)/K_1(1) = 0.045$. We use this approximation on the constricted flow channel in section 9; the full Bessel function is used in section 8 since we need longer interaction ranges to study interactions around the entire conical surface.

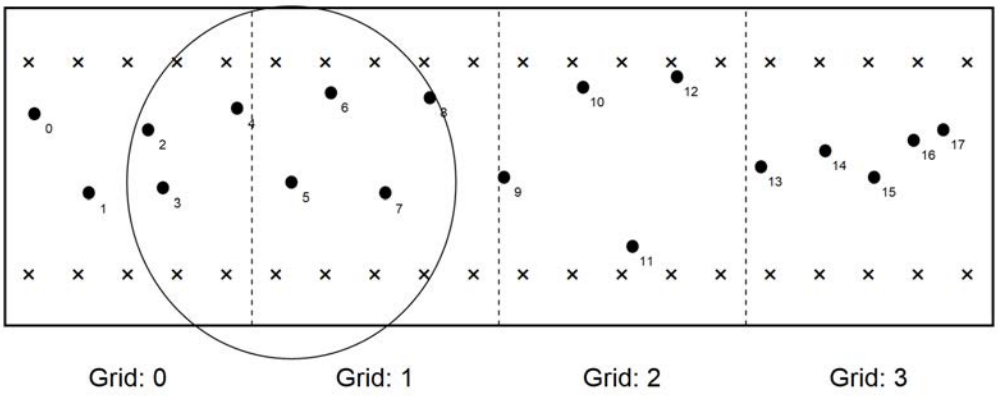

Figure 15: Example of a cell-decomposed thin channel. Vortices are labelled here and cross-referenced in fig. 16. A radius of influence is drawn around the vortex labelled 5; a vortex can interact with other vortices in the same grid, or an adjacent one.

6.2.1 Cell Decomposition

The simplest molecular dynamics method involves comparing each particle with every other one to calculate interactions. For a system of N particles, the time needed is proportional to N^2 so larger systems become very inefficient to simulate. Cell decomposition is a technique that reduces the number of comparisons required by establishing a grid of 'cells' where each vortex is indexed to the cell it is in.

Depending on the interaction distance, vortices in a cell and its nearest neighbours can be compared to fully compute the value of the interaction force. Since the cut-off length for vortices is typically much smaller than system size, our software takes advantage of this by decomposing the system into grids. Narrow channels can be decomposed into a 1D array of grids since the boundaries are usually within the cut-off length.

Figure 15 shows a section of a thin channel divided into grids of length 5. An ar-

	0	1	2	3
0	0	5	9	13
1	1	6	10	14
2	2	7	11	15
3	3	8	12	16
4	4	-1	-1	17
5	-1	-1	-1	-1
$\vdots$	$\vdots$	$\vdots$	$\vdots$	$\vdots$
N	-1	-1	-1	-1

Figure 16: Representation of `grid[4][N]` for the vortices labelled in fig. 15. Much of the array consists of -1 values; given the abundance and speed of memory available, an excessively sized array is unproblematic.

ray, `grid[4][N]`, is defined where the first index refers to the particular grid label and the second index contains the list of vortices in each cell. The second dimension is set to the number of vortices to ensure that the list can be completely filled if all the vortices are in the same cell. The array is populated by placing vortex indices into the corresponding i^{th} part, starting from `grid[i][0]` and increasing the value of the second index by one. Once there are no more vortices to place from a cell, an additional index of -1 is written to the end which can be used by the software as a loop terminator.

Decomposing cells makes simulation time proportional to N. For systems with many more pinned vortices than mobile, there must be $N_v \times N_p$ comparisons, with N_v flowing vortices and N_p pinned vortices, made without cell decomposition on just the interactions with pins. Decomposition reduces this number greatly and is a major optimisation seen in pinned systems. Figure 17 shows an example of the speed-up achieved using cell-decomposition, which results in approximately 1/3 of the number of required comparisons, as shown in fig. 17. Since the problem scales linearly, with N_p as the constant of proportionality, decomposition lowers this constant while maintaining an approximately

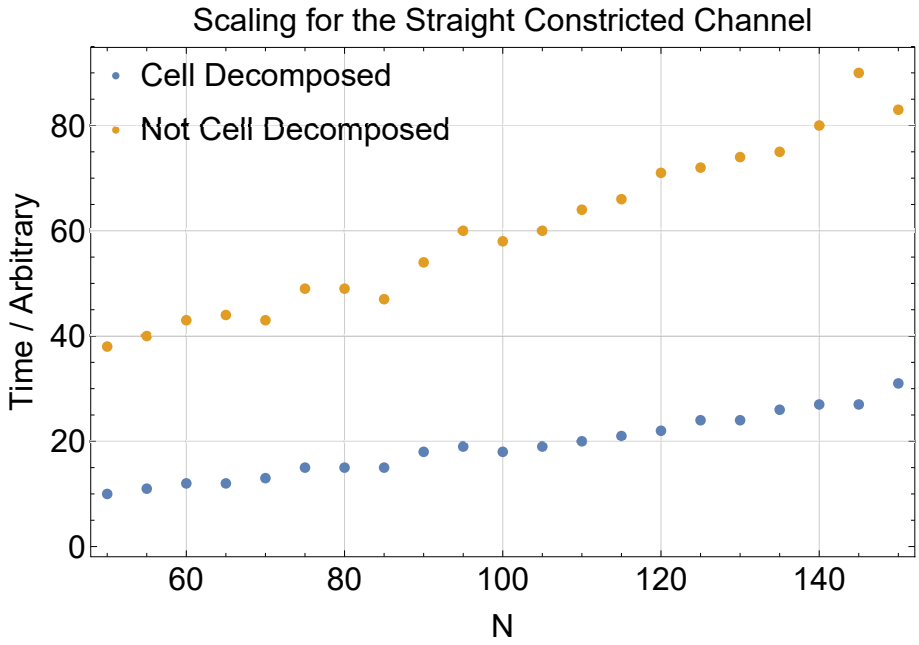

Figure 17: Plot of times taken for 10^5 time steps to run for different numbers of mobile vortices in the straight constricted channel. The system size is fixed with $N_p = 546$ pinned vortices.

linear scaling which dominates the quadratic scaling from mobile vortex interactions for the typical system sizes we investigate.

Since each constricted channel simulation is run over 10^7 time steps, and we run several hundred to generate the results presented in this thesis, many weeks of computation time have been saved. We run many different simulations in order to fine-grain phase diagrams and check that trends are consistent with nearby points. If one factors in simulations that yielded null results, we estimate at least 12 months of computational time has been saved.

6.2.2 Temperature

As previously mentioned, temperature is important in zero temperature systems for the initial process of simulated annealing. At zero temperature, it is quite possible for struc-

tures to be in energetically excited states that are unable to de-excite through an energetic barrier. These higher-energy states are known as meta-stable. Thermal fluctuations provide the local energy needed to overcome energetic barriers and increase the likelihood that the true ground state is found. The process by which we implement this is called simulated annealing and described in section 6.4.

Simulating temperature in a dissipative system involves maintaining a steady state of energy flowing in and out of the system. Since the dissipation term in the Langevin equation is proportional to vortex velocity, as kinetic energy increases, so does dissipation; a thermostat is used to regulate and balance the applied energy with lost energy.

A variety of thermostat schemes exist for Molecular Dynamics. To model temperature that exactly reflects nature is impossible [38]. Provided a thermostat scheme satisfies the equilibrium properties in eq. (6.3), it will provide a reasonable approximation to reality. We use the Ansdersen thermostat [13] which generates an isobaric and isothermal ensemble (NPT) [92].

Typically, thermostat implementations involve applying randomised forces with a stochastic function, $\chi(t)$, to particles to simulate Brownian motion. For one to best resemble physical reality, we require its statistical properties to match a random Boltzmann distri-

bution:

$$\langle \chi_i(t) \rangle = 0 \tag{6.3}$$

$$\langle \chi_i(t) \chi_j(t') \rangle = 2k_B T \eta \delta_{ij} \delta(t - t'). \tag{6.4}$$

The angle brackets denote the average of the entire distribution described by χ. Generated thermal kicks must be centred at zero and be uncorrelated in time and between successive particles. The Andersen Thermostat uses a Gaussian distribution of thermal kicks that are applied to particles at each time step at a predetermined probability, p [13]. In [109], we calculated the coefficient of eq. (6.3) by considering the corresponding moments to the Fokker-Plank equation. This probability must be tuned such that the correct distribution of energy is observed, without losing the deterministic dynamics to the noise. Since there is no exact solution to the Langevin equation with temperature due to stochasticity, using high-accuracy algorithms to solve wastes computational time. We integrate at first order, ensuring the time increment, Δt, is small enough such that the maximum change of position of any vortex is $a_0/50$ [60, p.26]:

$$\mathbf{r_i}\left(t + \Delta t\right) = \mathbf{r_i}\left(t\right) + \Delta t \mathbf{v_i}\left(t + \Delta t\right) \tag{6.5}$$

$$\mathbf{v_i}\left(t + \Delta t\right) = \frac{1}{\eta}\left[\sum_j \mathbf{F}_{\mathrm{vv}}(|\mathbf{r_i}\left(t\right) - \mathbf{r_j}\left(t\right)|) + \mathbf{F}_{\mathrm{EXT}}(\mathbf{r_i}\left(t\right), t) + \sqrt{\frac{2k_B T \eta}{\Delta t p}} \gamma_{\mathbf{i}}\left(t\right) \Theta\left(p - q_i\left(t\right)\right)\right]. \tag{6.6}$$

Here, the temperature is set to an absolute scale, T, from which we determine its relative scale by finding the temperature required to melt a vortex lattice, T_m. We calculate T_m in

section 6.3. During each increment, a uniformly distributed random number, $q_i \in [0, 1]$, is generated. If $q_i < p$, then $\gamma_\mathbf{i}$ is used to generate a Gaussian-distributed kick in 2D. We set $p = 0.01$ since we find it maintains the Gaussian distribution and deterministic dynamics effectively.

6.3 Numerically Deriving the Melting Temperature

As previously discussed in section 3.4.1, we expect the vortex lattice to melt at some critical temperature. We need to know this temperature since, if we simulate at higher temperatures, any previously established order can be lost, undoing any previously implemented annealing cycles. It is sometimes useful to melt the lattice, as it can reset the system's initial conditions without having to run a separate simulation.

The thermostat is calibrated relative to the vortex lattice melting temperature, T_m. Knowing T_m means we can set the temperature well below melting to study strong lattice dynamics, or well above to apply parts of the annealing process. We originally calculated T_m in [109] and followed the methodology in [101]; this section explores the original methodology followed and concludes with a value for T_m that we use throughout this thesis.

In 2D, we use order parameters as criteria for determining whether or not a lattice has melted. Since the zero temperature ground state of the vortex lattice is triangular, we use the hexatic order parameter to calculate how much triangular order is present [101]:

$$\Psi_H = \left| \left\langle \frac{1}{N_v} \sum_{i=1}^{N_v} \frac{1}{z_i} \sum_{j=1}^{z_i} e^{6i\theta_{ij}} \right\rangle \right|^2 . \tag{6.7}$$

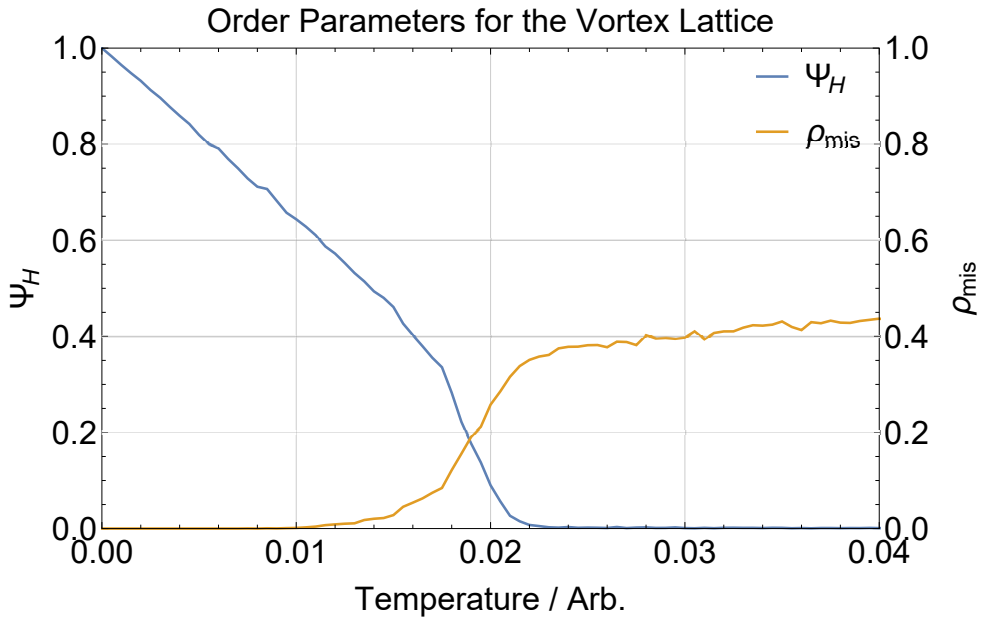

Figure 18: Order parameter values for a range of temperatures. This data was originally presented in [109] and the diagram is also adapted from the same source. The figure resembles one presented in [101] since we follow a similar methodology.

The coordination number, z_i, equals the number of nearest neighbours for the i^{th} vortex. The angle between the i^{th} and j^{th} vortex is given by θ_{ij}. The angle brackets denote a time-averaging of states in order to find a statistical mean value. For a perfect triangular lattice, $\Psi_H = 1$. For highly disordered lattices, $\Psi_H \to 0$.

The misalignment density is also used to determine disorder [101]:

$$\rho_{\text{mis}} = 1 - \frac{1}{N_v} \sum_{i=1}^{N_v} \delta_{6,z_i}, \tag{6.8}$$

where the Kronecker Delta is used to calculate the number of vortices with 6 nearest neighbours. For a fully coordinated triangular lattice, $\rho_{\text{mis}} = 0$. When the lattice is highly disordered, we usually find $0 \ll \rho_{\text{mis}} < 1$ since there are often six-fold coordinated vortices, even when the system is noisy.

For reference, we simulate a $34 \times 34\sqrt{3}/2$ system populated with 1156 vortices which form a perfect triangular lattice when placed accordingly with periodic boundary conditions applied in the x and y directions. This system size is large enough such that a vortex is unable to interact with itself due to the cut-off radius, which would otherwise cause unphysical long-range order. The boundary conditions are such that $\mathbf{r_i} = \mathbf{r_i} + 30m\hat{\mathbf{x}} + 34\sqrt{3}n\hat{\mathbf{y}}/2$ with $\{m, n\} \in \mathbb{Z}$. We measure the order parameters for a series of temperatures several times and plot the averages in fig. 18. Each measured point is left for 10^5 time steps before measurement to ensure thermalisation.

From fig. 18, we use the crossover of the two order parameters to define T_m. Since we are interested in an approximate value, we find $T_m \simeq 0.02$.

6.4 Simulated Annealing

We anneal our systems by initiating them at a temperature much higher than T_m. Vortices will be highly disordered at this temperature and will resemble a random initial placement condition. It is then our choice of how to bring the temperature down, but a quick drop in temperature risks quenching the system, leaving it stuck in a meta-stable state. We find an exponential decay works well to bring the temperature down below melting, but to allow the system enough time to access its microstates. We anneal our systems for 10^6 time steps; this has generated reliable results in sections 7 and 8 from which we base our calculations.

6.5 Parallelisation

The arrival of multi-core processors in the early 2000s has enabled scientists to greatly speed up numerical simulation time by offering increasing numbers of floating point operations per second (FLOPS). With individual processor clock speeds plateauing, due to the approaching quantum limit of transistor size, adding a second, fourth, or even eighth core to a CPU will theoretically boost overall performance in line with Moore's law [35].

There are three main categories for a computational problem: memory-bound, input/output-bound, and compute-bound. Memory bound problems are limited by the amount of available storage and random access memory a computational node has. For example, the 1D Ising model of spins requires 2^n bits of memory to store all of the microstates. If a 3D model is studied of size $3 \times 3 \times 3$, then 2^{27} bits are needed which corresponds to 16.8GB of memory. Solving these problems exactly is therefore quite limited.

I/O-bound problems occur when data is processed faster than it is requested. This kind of problem becomes increasingly more prominent as processor clock speeds increase, although not very relevant to physical simulation studies.

Compute-bound problems are limited by the performance of the CPU they are being run on. Molecular dynamics is an example of this. Since position data for even a large number of particles is relatively small in file size, it can be written to local cached memory on the CPU much quicker than it can be processed. Investment in fast CPUs will speed up solution time with little to no programming effort.

Parallelisation enables us to increase overall clock speed by distributing the work load to multiple threads that are run, in parallel, on a CPU. In this section, we discuss how we program with Intel's Cilk package in the C++ environment to parallelise the custom molecular dynamics code used in this thesis.

Further parallelisation is possible with the use of CUDA, a language developed by Nvidia for the general purpose programming of their Graphics Processing Unit (GPU) chips. With the specialised nature of GPUs, compute-bound problems often become memory-bound problems due to the large number of processing cores available. This is discussed in section 6.5.2.

6.5.1 Utilising the Intel Cilk Package

Although there are numerous ways to parallelise code, including OpenMP and MPI, we use a proprietary extension for the C++ language developed by the Intel corporation: CilkPlus. CilkPlus can be used alongside the Intel C++ Compiler (ICC) or on versions of the GNU C++ Computer (GCC). It enables the programmer to make relatively small changes to existing code, provided it is parallelisable, by including some functions with parallel properties. The hardware available while research was conducted for this thesis was exclusively Intel CPUS; ICC is optimised for Intel hardware which makes it an effective choice. It should be noted that it has recently been announced that CilkPlus will be deprecated in future versions of ICC and replaced with more modern parallelisation protocols [5]. CilkPlus is now open source and is still relevant, especially for simple implementations of parallelised software.

The basic principle of using Cilk is the parallel for-loop: `cilk_for` [1]. This loop must be initiated in the same way a traditional C++ for loop is by including the initiator, end condition, and increment: `cilk_for(int i=0; i<8; i++)`. Each step in the for loop is then evaluated in parallel; if there are eight threads available, then each one will evaluate the loop for one of the unique values of `i`.

We also use the `cilk_sync` command which forces all threads to wait at this point in the code until all values of `i` have been evaluated up to this point. This is used to avoid data racing by preventing certain parts of the loop changing a value which an earlier part might rely on.

For a system of N particles, the parallel for loop is:

```
1 cilk_for(int i = 0; i < N; i++){
2         increment(i);
3         cilk_sync;
4         r[i][0] += dr[i][0];
5         r[i][1] += dr[i][1];
6 }
```

The `increment(i)` function calculates the change of position for the i^{th} vortex and sets `dr[i]` to this value. No increment depends on any other, so the order does not matter, provided the position steps are updated once all the increments are calculated. The `cilk_sync` prevents any thread from updating the position data, stored in `r[i]`, until all of the increments are calculated. This can be extended to higher order integration algo-

rithms with each step being inserted and separated with `cilk_sync` commands.

Parallelisation is crucial when simulating physical systems. CilkPlus, in conjunction with the use of BlueBEAR, has provided us with the means to run the quantity of code needed for this project. CilkPlus is also useful when running simulations locally; we use Core i7 processors, designed for parallel processing.

6.5.2 Massive Parallelisation with CUDA

Computational tasks are often best suited to hardware designed with a particular application in mind. GPUs are intended to perform many basic image transformations per second, ideal in the video entertainment industry. Although not designed for molecular dynamics, the architecture translates well into physical simulation problems. Furthermore, since there is a constant demand of higher bandwidths and frame rates in a healthy competitive market between AMD and NVidia chips, improved technology is released every few years at accessible prices.

The architecture of GPUs contrasts with that of CPUs due to the specific nature of the task to be completed. CPUs are general purpose chips. GPUs often have two orders of magnitude more cores than CPUs and much faster, albeit less, local cached memory. If a non-graphical application can be written to run on a GPU, this is known as General Purpose computing on Graphics Processing Units (GPGPU) [7].

Although a majority of our software is written for CPU nodes, we recognise that GPGPU

offers much higher speeds for simulations of the vortex lattice. The technology improved significantly during the course of the project and is now mainstream enough to begin writing applications for. We implemented the energetic sampling of parabolically confined Yukawa particles, discussed in section 4.1, and some simulations of the cylinder presented in section 7. We were limited by the availability of GPU resources for the cylinder simulations and a majority were run on CPU nodes due to the abundance of them. There are now GPUs on the consumer market that can serve as much better molecular dynamics calculators than similarly-priced CPUs.

The basic components of a CUDA application involve initialising memory on the GPU, sending the data to be processed, processing the data, and sending it back to the host machine.

6.6 Monte Carlo - Metropolis Prescription

While molecular dynamics is well suited to studying dynamics and motion, there is an alternative routine we use to find structural ground states. Some Monte Carlo methods are used to find ground states, given a temperature, for a general classical or quantum system. The general principle is to sample the energy landscape of the system by considering small perturbations to it and evolving the system towards the lowest energetic minimum. In principle, for a finite temperature, the algorithm should be run ad infinitum to guarantee all microstates have been sampled. The metropolis prescription is a Monte Carlo method which is commonly used for this purpose.

The Metropolis algorithm is a Markov Chain Monte Carlo (MCMC) method [50]. A Markov Chain is any process for which its time-evolution is only dependant on its current state, not its history. The constraints in eq. (6.3) represent a Markov Chain since they have no memory of their history. It is used to find ground states without any history-dependence where new state propositions are taken from a statistical distribution designed to match a Boltzmann distribution. The algorithm we implement is as follows [60]:

- Select a vortex at random and propose a new position $\mathbf{r_i'} = \mathbf{r_i} + \Delta\mathbf{r_i}$ where $\mathbf{0} < \Delta\mathbf{r_i} \leq a_0(\hat{\mathbf{x}} + \hat{\mathbf{y}})/\sqrt{2}$ is a uniformly randomly generated number. Moves greater than a lattice spacing, a_0, are ignored.

- If the new system energy, E', is less than the previous system energy, E, then the proposed move is accepted. If $E' > E$, then accept the move with probability $e^{(E-E')/k_BT}$.

Allowing the system to evolve out of potential wells means it can escape from metastable states. If the algorithm is run for an infinite amount of time, it is guaranteed that the entire state space will be searched and the ground state discovered. Provided it is run for sufficiently long enough, but for a finite amount of time (typically one million time-steps are used in our implementations), it will sample enough of the state space to give an approximation to the true ground state. It is not possible, in general, to know if we have missed the true ground state, although we can know we are close to it if the internal energy and structure matches with theoretical predictions. In these cases, we take the lowest energy state found to be the approximate ground state. We use Monte Carlo in section 8 and typically find that the lowest energy states we observe are not quite the

ground states. This is due to other configurations which have very similar energies to the ground state forming in small domains, slightly raising the energy. The numerical ground states are, however, structurally similar to predictions and hypotheses we make.

7 Structural Ground States of Vortices in a Cylindrical Channel

As we have established in sections 4 and 5, the role of the boundaries and the channel width on confined vortices are both important in determining the structures and patterns that are observed. In this section, we separate the boundaries from the width by applying a periodic boundary condition in the confining direction, such that vortices self-confine by aligning with the cyclically repeated images of themselves. This system resembles a cylinder, where vortex positions are on the surface and interactions mediate around it.

We stress that this cylinder is an analytic tool. It is not a realisable system, but the results reveal the physics on more generally confined systems. Although not physical, it can still be simulated, so results can be checked independently using various computational techniques.

Vortices align themselves into structural states described by the phyllotactic notation. Using the fact that states must be phyllotactic and a homogeneous isosceles triangular lattice, we generate an analytical set of states, where one must be the ground state for any set of system parameters. The associated phase diagram of circumference, c, and number density, n_L, shows that phases are separated by curves described by $c = \alpha/n_L$, where α is a dimensionless number that can be derived for each transition.

Using α, we scale out circumference and number density to simplify the system to a set of states described by this single variable. We are left with a smaller parameter space to search and do so numerically. By comparing transition points between various states

we find that transitions occur when two states are identical aside from a global rotation of one into the other, or when the energy of two differently distorted lattices become equal. The first case yields exact solutions to the transition lines on the phase diagram. For the second case, we find that the energy of each state when plotted against lattice vector length varies approximately quadratically. Since we know the exact length for where the energetic minimum is, we use the symmetry of the energetic parabola to find transition lines. These results are transcendental and, since the energy curves are not exactly quadratic, approximations.

Since we can find any transition between any two states, we complete the phase diagram to arbitrary size, starting from any known state. With a known state, the closest transition point must be the transition, so a series of states can be incrementally constructed.

Finally, we reflect on the states we observe, and how they compare and contrast to those in a parabolically confined channel. Many of the states are helical, which is exclusive to cylindrically confined systems. The key feature we note is that the parabolically confined channels tend to force states to align along them, reducing the number of possible states one needs to consider.

Since previous studies have focussed on hard spheres with only contact interactions, the results we present are novel. One physical realisation of this system consists of magnetic spheres on a cylinder [12]; our system is physically abstract since there are no such sys-

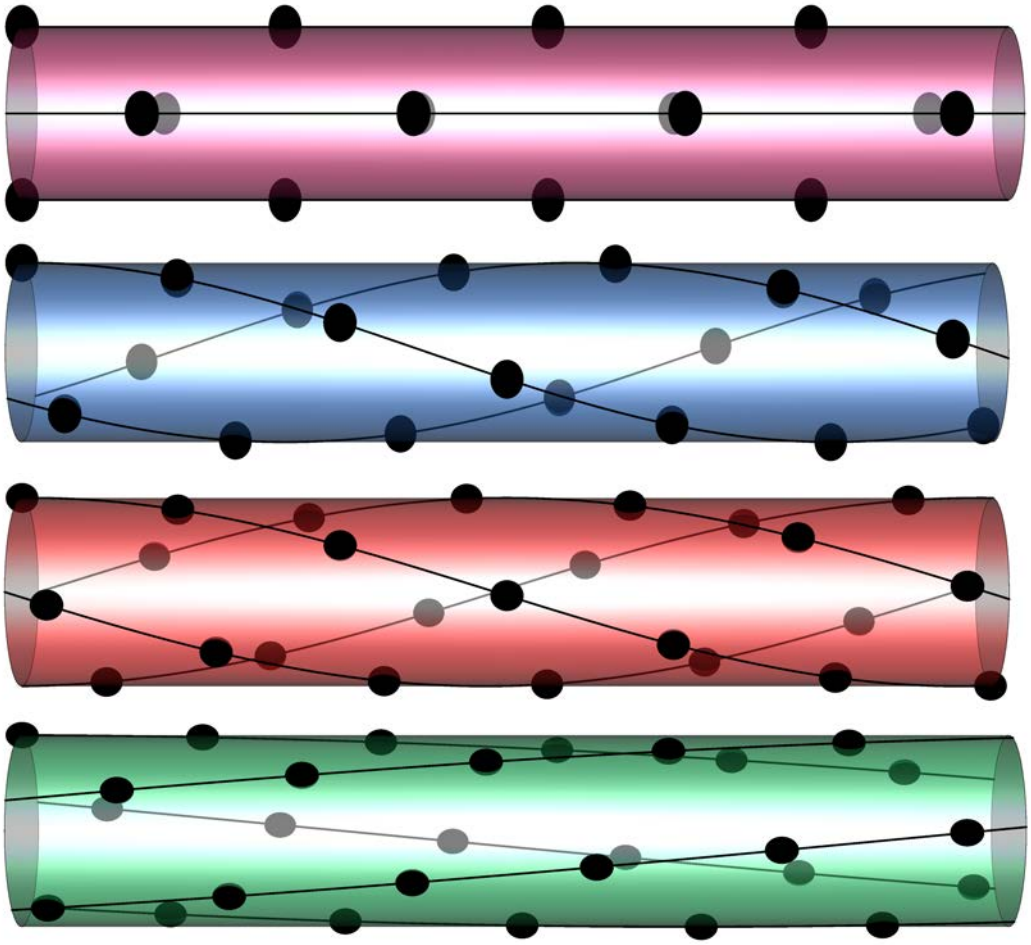

Figure 19: Examples of some ground states rendered in 3D. The Lines join phyllotactic chains that wrap helically around the cylinder.

tems of vortices on the surface of a cylinder. The goal of this work is to study the effects of removing a confining potential and to understand the influence of confinement in a theoretical system. Additionally, this work extends the knowledge of generally repulsive objects on cylinders by providing a new method of constructing states and analysing transitions.

7.1 Description of the Cylindrical System

When setting up a cylindrical system of particles on the surface, there are two possible particle interaction distances to select from. Firstly, a direct line-of-sight 3D distance calculation of straight lines. This type of interaction is relevant for systems including nano-particles confined in carbon nanotubes, where the interaction doesn't follow the surface of the nanotube [56, 120] (discussed in section 5). Direct line-of-sight interactions generate helical phases, where particle chains twist around the cylinder; the periodic geometry that we employ also generates helical structures.

Interactions in our system mediate along the surface of the cylinder. This choice is made to remove the effects of the hard boundary of the cylinder. This is thought of as a cylinder with an insulating core and a conducting surface medium. We then consider this to be a 2D system with a periodic boundary condition imposed in a given direction (in our case, y). Defining the circumference, c, we then write the interaction energy between two vortices to be a sum of images:

$$V = \sum_{i=-\infty}^{\infty} K_0(|\mathbf{r_1} - \mathbf{r_2} + i\mathbf{V}|). \tag{7.1}$$

The periodicity vector is consistent with [78]: it is the position vector from a vortex to its first image. In our case, $\mathbf{V} = \hat{\mathbf{y}}c$, where $\hat{\mathbf{y}}$ is the unit vector in the y direction. The infinite sum is complicated by the need to sum over all vortices in the system; we consider a system of infinite length in order to avoid any potential subtleties due to finite size and periodic boundary effects. The infinite system allows us to focus on bulk effects and be more exact about domains of structural ground states. The full potential energy for an infinite set of vortices, each interacting with all other vortices, is then given by:

$$V = \sum_{i \neq j} \sum_{k=-\infty}^{\infty} K_0(|\mathbf{r_i} - \mathbf{r_j} + k\mathbf{V}|) \qquad \forall \{i, j\} \in \mathbb{Z}. \tag{7.2}$$

A general solution to the minimised potential is impossible, but by posing the problem with the assumption that the ground state should be an ordered triangular lattice, we can make some analytic progress.

The triangular lattice is the state for which particles maximise nearest neighbour distances, thus minimising their potential energy. Section 3.4 shows an example of this for vortices; phyllotactic states observed on cylinders also resemble triangular lattices [77, 118]. The triangular lattice is the most efficient way to spread out the contents of a system in a homogeneous manner. There is an expectation that we will observe triangular lattices forming in our system and, for rigour, we simulate the system for a

variety of parameters with the usual molecular dynamics procedure to justify our ansätze.

7.2 Initial Numerical Results

When simulating a finite-size cylinder, we avoid boundary effects by making the cylinder periodic in the x direction, effectively making it a torus. Provided the torus is sufficiently long, we expect to see desired bulk effects. The caveat to a torus is that commensurability effects are present. For example, if the ground state lattice has some angle of rotation. θ, with respect to x, then unless $ma\cos(\theta) = L$, where a is the lattice parameter, m is an integer number of vortices wrapping around, and L is the length of the torus, the state can not be periodic. A grain boundary forms due to this commensurability effect and a small region of the structure will differ from the ground state. We set the length of the torus to 100 units long so that bulk effects dominate; regions of misaligned states are up to 20 units long so the bulk effect is noticeable. We anneal the vortices to zero temperature using the periodic method detailed in section 6.4.

Figures 20 and 21 show two examples of calculated ground states with Molecular Dynamics and Monte Carlo methods. Both methods are prone to the formation of dislocations due to commensurability, but both indicate the formation of the triangular lattice.

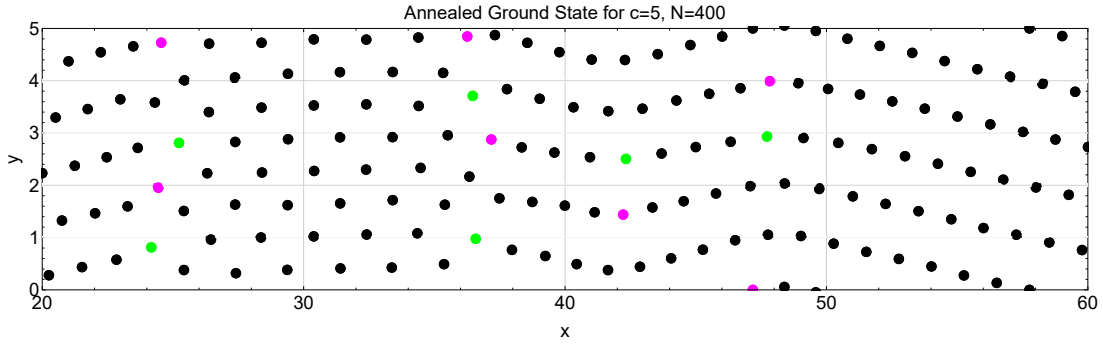

Figure 20: Molecular dynamics simulation of an annealed ground state for $c = 5$ and $N = 400$, with system length $L = 100$. Only part of the snapshot is shown to highlight the grain boundaries and dislocations. Dislocations vortices with 5 and 7 neighbours are coloured purple and green respectively. The structure located at $25 \leq x \leq 36$ is not the ground state. The ground state observed in the remainder of the system can be orientated with an angle above or below the $x-$axis. Since the energy is identical for either orientation, the snapshot we observe shows multiple regions of each angle.

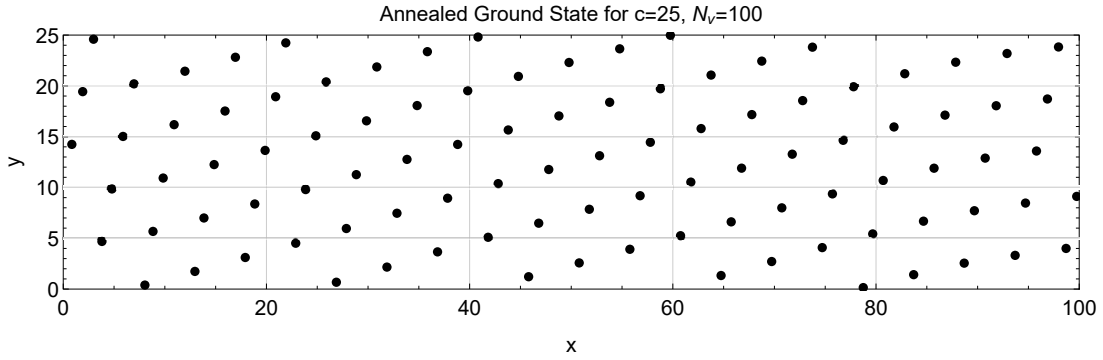

Figure 21: Example of a ground state calculated with the Monte Carlo method. This example is a case where the entire system aligns without grain boundaries or dislocations.

A crucial feature observed in these simulations is that two of the three unit vectors are the same length. Figure 22 shows histograms of vector lengths indicating this feature. Two equal vector lengths will be used as one of the ansatz for constructing ground states.

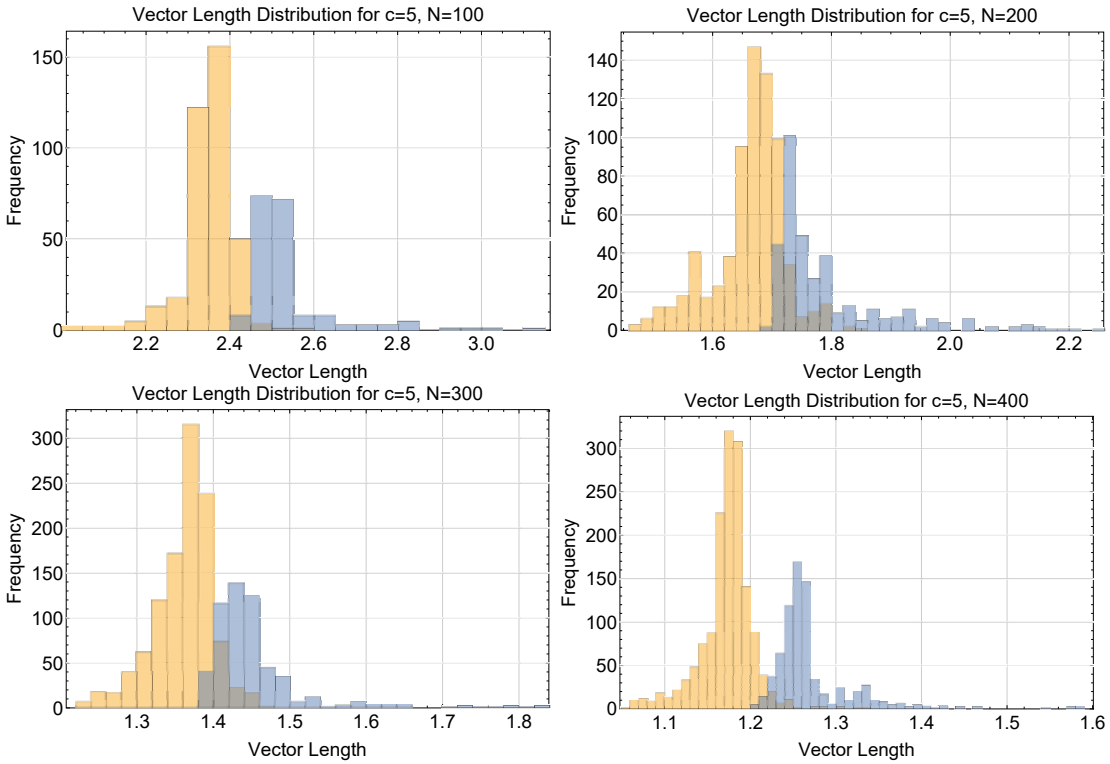

Figure 22: Histograms of vector lengths for some selected ground states. The yellow coloured data shows two-thirds of the data and indicates that two lattice vectors are equal length since their distributions lie on top of one another.

7.3 Ansatz for the Ground State Structure

On the infinite cylinder, we expect a homogeneous triangular lattice with unit cells of equal area, at least two of the lattice vectors to be equal in length, and an integer combination of the two equal lattice vectors to equal the periodicity vector. We define these two vectors, $\mathbf{a}$ and $\mathbf{b}$, as the solutions to the following set of equations:

$$\hat{\mathbf{z}} \cdot (\mathbf{b} \times \mathbf{a}) = c/n_L \tag{7.3}$$

$$|\mathbf{a}| = |\mathbf{b}| \tag{7.4}$$

$$m\mathbf{a} + n\mathbf{b} = \hat{\mathbf{y}}c. \tag{7.5}$$

Here, we define n_L to be the linear density (number per unit length) of vortices in the system. Although unconventional, the system is quasi 1D since one direction is finite and the other infinite, so a 1D density definition is appropriate. The linear density relates to the regular 2D density, $\rho_2 = n_L/c$, which is a scaling to the number of vortices per unit area. We continue to use n_L in this section, with ρ_2 becoming important in section 8. The area of a hexagonal unit cell is the cross product of two of the lattice vectors; we include the dot product in the direction perpendicular to the lattice, $\hat{\mathbf{z}}$, to be mathematically consistent. The vectors technically become 3D with a constant zero in the z direction, and we only express the x and y coordinates from now on. The integers, m and n, become parameters and form a set of vectors that align to the periodicity of the cylinder. These equations are solved by considering vector components since the periodicity constraint can be written as two equations giving four equations and four unknowns:

$$\mathbf{a} = \frac{1}{n_L}\begin{pmatrix} -n \\ \frac{mcn_L - n\sqrt{(cn_L)^2-(m^2-n^2)^2}}{m^2-n^2} \end{pmatrix} \qquad \mathbf{b} = \frac{1}{n_L}\begin{pmatrix} m \\ \frac{-ncn_L + m\sqrt{(cn_L)^2-(m^2-n^2)^2}}{m^2-n^2} \end{pmatrix}. \quad (7.6)$$

There is an additional set of solutions which are oppositely orientated to the x axis. These are geometrically identical aside from the rotation and hence energetically degenerate. The rotated solutions explain the reorientation of the lattice we observe in fig. 20. As the vortices cool, the ground state lattice can nucleate in two different orientations and positions and form a grain boundary. With two pieces of lattice, realigning a large number of vortices is energetically difficult without forming more boundaries. The opposite-angled solutions are found by interchanging $m \leftrightarrow n$ or by considering negative values of either

integer. Given this degeneracy, we simplify the numerics by restricting m and n to only positive values. Due to the interchange condition, we also only need to consider values of $m \geq n$. If $m = n$, then we use L'Hôpital's rule to reduce the vectors to:

$$\mathbf{a} = \begin{pmatrix} -m/n_L \\ c/2m \end{pmatrix} \qquad \mathbf{b} = \begin{pmatrix} m/n_L \\ c/2m \end{pmatrix}. \tag{7.7}$$

We note that if $cn_L < m^2 - n^2$, then the square roots become imaginary and that particular state can not form.

We are left with a 2D phase space to explore, with a set of structural states formed by the valid combinations of m and n. We proceed by performing brute force numerical minimisation to generate the ground state phase space.

7.4 Numerical Sampling of Candidate States

We calculate each state's energy and compare to find the ground state. Although there are an infinite set of states, the initial molecular dynamics simulations indicates the values of m and n we should sample are small. We derive eq. (7.24) in section 7.6.3 which validates this assumption post-hoc. The states seen in fig. 20 either have $(m = 4, n = 4)$ or $(m = 4, n = 1)$ for a linear density $n_L = 4$. We test the entire phase space for $0.5 \leq c \leq 5$ and $0.5 \leq n_L \leq 5$ and with values of $m <= 10$ and $n <= 10$. Extremely low values of c are difficult to simulate accurately since the cut-off range of the vortex-vortex interaction

is much larger than the system size, and we must sum around the cylinder many times, which is computationally expensive. We note that c and n_L must be finite and solve the phase space with a resolution $\delta c = 0.01$ and $\delta n_L = 0.01$.

Since the lattice is homogeneous, the potential energy every vortex has is identical to any other. This means we need only consider the per-vortex energy by calculating the potential energy acting on a single vortex, that we place at the origin for simplicity. The exact value of the energy is:

$$E = \sum_{i,j} K_0(|i\mathbf{a} + j\mathbf{b}|/\lambda) \qquad \forall (i \neq 0) \vee (j \neq 0). \tag{7.8}$$

For clarity, the notation indicates that summations include all values of i and j, except for the case where they both simultaneously equal zero (this avoids a diverging self-interaction). This summation has no immediate way of finding a Fourier expansion, so we rely on the fast convergence of the Bessel function to zero for large distances. Provided we generate a lattice which encompasses vortices up to the numerical cut-off of the Bessel function, we can be computationally exact. Numerically solving $K_0(r) = 10^{-16}$ gives us a cut off of $r_c = 35.282$. Although this calculation is relatively computationally demanding for a fine-grain phase space, it can be parallelised at several different levels. One option is to parallelise the set of candidate energies for each combination of m and n. Computing different points on the phase space in parallel, however, is the most efficient way to parallelise since there is no down-time for cores that are waiting for longer calculations to finish. The algorithm finds a table of ground states for given values of c and n_L and

generates the following phase diagram shown in fig. 23.

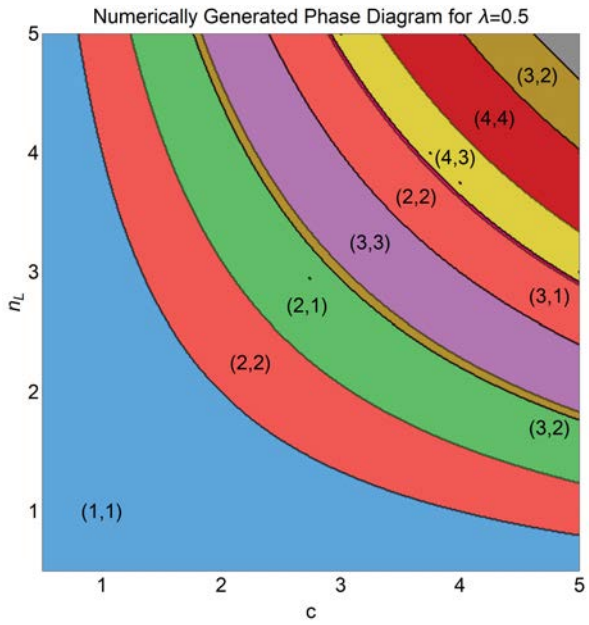

Figure 23: Numerically derived phase diagram. Values of m and n for each state are shown as (m, n).

7.5 Scaling out System Parameters

The transition lines in fig. 23 fit to curves of the form $c = \alpha_i/n_L$, where α_i is a number to be found for each transition. This relationship is key to analytically solving for transitions since we can now reduce the problem to a single-variable exercise. If we find a single point on the transition line, we can calculate the remainder of the line since we know its form is monomial; this is illustrated in fig. 24. The simplest way to do this is by setting searching for transitions along the line $c = n_L(= \sqrt{\alpha})$; this will re-scale the lattice vectors to the following:

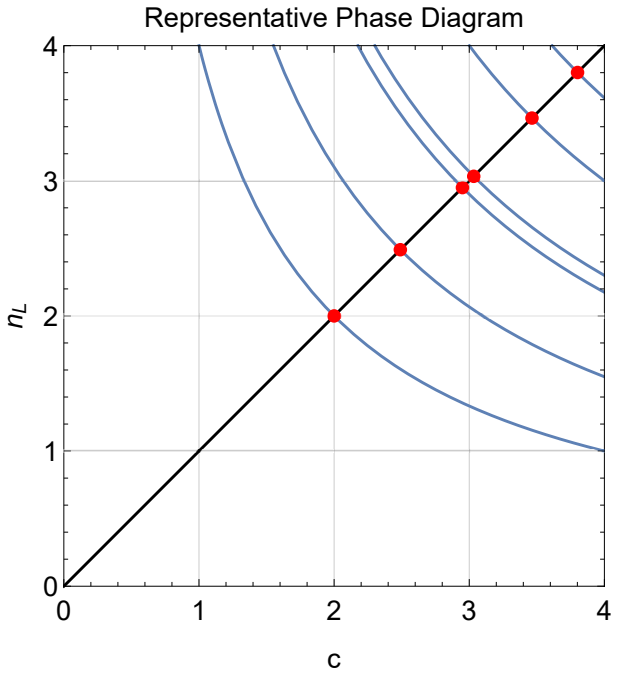

Figure 24: Example of part of the phase diagram with transition lines of the form α_i/c. The line $c = n_L$ cuts through each transition line once at the point $(\sqrt{\alpha_i}, \sqrt{\alpha_i})$. The intersections are highlighted with red points.

$$\mathbf{a} = \frac{1}{\sqrt{\alpha}} \begin{pmatrix} -n \\ \frac{m\alpha - n\sqrt{\alpha^2-(m^2-n^2)^2}}{m^2-n^2} \end{pmatrix} \qquad \mathbf{b} = \frac{1}{\sqrt{\alpha}} \begin{pmatrix} m \\ \frac{-n\alpha + m\sqrt{\alpha^2-(m^2-n^2)^2}}{m^2-n^2} \end{pmatrix}. \tag{7.9}$$

$$\mathbf{a} = \begin{pmatrix} -m/\sqrt{\alpha} \\ \sqrt{\alpha}/2m \end{pmatrix} \qquad \mathbf{b} = \begin{pmatrix} m/\sqrt{\alpha} \\ \sqrt{\alpha}/2m \end{pmatrix}. \tag{7.10}$$

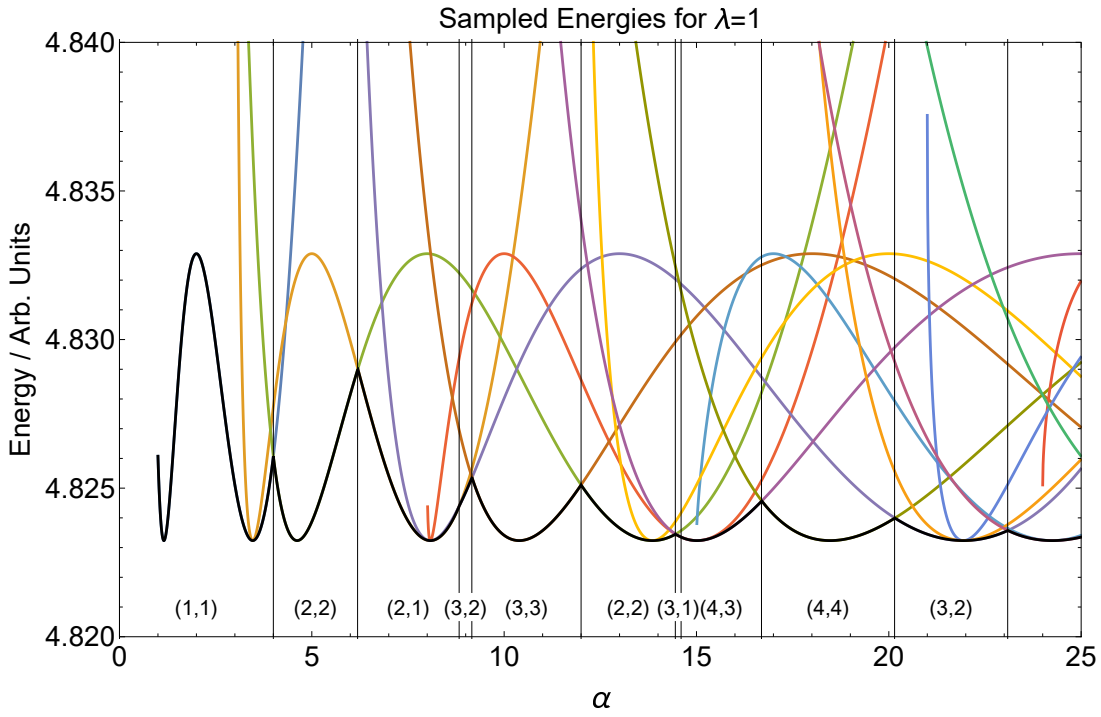

Figure 25: Energetic sampling along the line $c = n_L$. The ground state is highlighted in black and candidate state energies are coloured. Structural transition points are divided by the vertical black lines. The notation (m, n) is used the same way as fig. 23.

7.6 Analytic Solutions

7.6.1 Structures and Categorisation

We can write down particular values of α in terms of m and n that generate special cases of the lattice that help us determine the structure of the phase space. The perfect hexagonal lattice, formed of regular triangles, is guaranteed to have a lower energy than any distorted version of itself. The perfect lattice forms when all three lattice vectors (not just the two we enforce) are equal in length. We define the third lattice vector, $\mathbf{c}_\pm = \mathbf{a} \pm \mathbf{b}$, which can take two values, where the shortest length gives the primitive lattice vector of interest, and solve either: $|\mathbf{c}_\pm| = |\mathbf{a}| = |\mathbf{b}|$. Finding the solutions is a matter of elementary algebra: $\alpha_{\triangle\pm} = 2(m^2 \mp mn + n^2)/\sqrt{3}$. These solutions represent a set of energetic minima

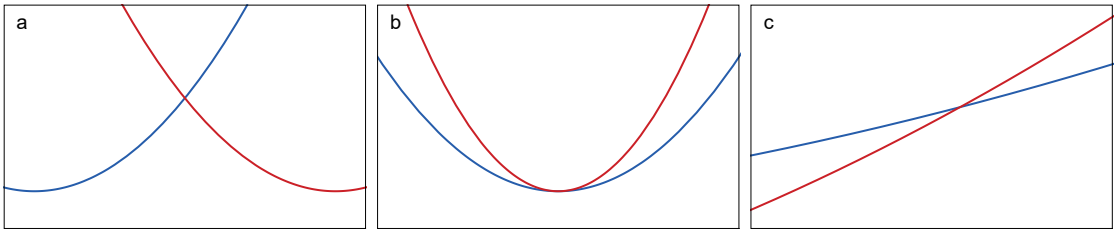

Figure 26: Examples of the three types of energetic equivalence. a) Lattices have different hexatic minima and become equal in energy somewhere between them. b) Lattices share a hexatic minima. No examples of a ground state transition are observed at this type of point, only an instantaneous degeneracy. c) Lattices share an energetic minima and a ground state transition occurs away from the hexatic point.

that are connected by the structural transitions that we observe in fig. 25.

Another special case is the square lattice. When the lattice takes a square form, $\mathbf{a}$ and $\mathbf{b}$ are perpendicular and $|\mathbf{c}_+| = |\mathbf{c}_-|$. We solve this equation and find $\alpha_\square = m^2 + n^2$, i.e. the maxima observed in fig. 25. The square lattice will be useful later in this section when we define the phyllotactic notation.

Given a set of energetic minima defined by $\alpha_\triangle$, we sort them into ascending order and join them at structural transition points. Where degenerate minima occur, we must consider all the possible energetic crossovers between two points. We develop the method for finding transition points by solving with reference to the numerical results before demonstrating an algorithm that can extrapolate to $\alpha > 25$.

The first transition to occur is the $(1,1) \rightarrow (2,2)$ transition. We hypothesise that the energies of each lattice equate due to them having the exact same structure up to a global rotation. If this is the case, the primitive lattice vectors of each state must be equal in length, which is how we solve for this transition point. Describing the lattice vector as a

function of m and n, $\mathbf{a}(m,n)$:

$$|\mathbf{a}(1,1)| = |\mathbf{a}(2,2)| \tag{7.11}$$

$$\begin{vmatrix} -1/\sqrt{\alpha} \\ \sqrt{\alpha}/2 \end{vmatrix} = \begin{vmatrix} -2/\sqrt{\alpha} \\ \sqrt{\alpha}/4 \end{vmatrix} \tag{7.12}$$

$$\frac{1}{\alpha} + \frac{\alpha}{4} = \frac{4}{\alpha} + \frac{\alpha}{16} \tag{7.13}$$

$$\alpha = 4. \tag{7.14}$$

Only real and positive solutions need to be taken here. This value agrees with the numerical result and the global rotation method accounts for several of the transitions we observe. If we continue to use this method to find transitions, we find $\alpha((2,2) \to (2,1)) = 8\sqrt{3/5} \simeq 6.1968$, which again agrees with the numerical result. If we try the next transition for $(2,1) \to (3,2)$, we find $\alpha = 14/\sqrt{3} \simeq 8.0829$, which is actually the degenerate hexatic minimum that both states share. It appears as if the curves cross over each other again approximately 0.6 units of α later. To see what is happening physically, we need to look at the lattices more generally and study their energetic evolution.

To do this, we construct lattices at the numerically derived transition points and compare them to reveal categories of lattice that relate to $\mathbf{c}$ and relative lengths of $\mathbf{a}$ and $\mathbf{b}$. We number the categories $\textcircled{1} \to \textcircled{7}$, and they are defined as follows:

- $\textcircled{1}$: $|\mathbf{a}| < |\mathbf{c}_-|$
- $\textcircled{2}$: $|\mathbf{a}| = |\mathbf{c}_-|$
- $\textcircled{3}$: $|\mathbf{c}_-| < |\mathbf{a}| < |\mathbf{c}_+|$

- ④: $|\mathbf{c}_-| = |\mathbf{c}_+|$
- ⑤: $|\mathbf{c}_+| < |\mathbf{a}| < |\mathbf{c}_-|$
- ⑥: $|\mathbf{a}| = |\mathbf{c}_+|$
- ⑦: $|\mathbf{a}| > |\mathbf{c}_+|$

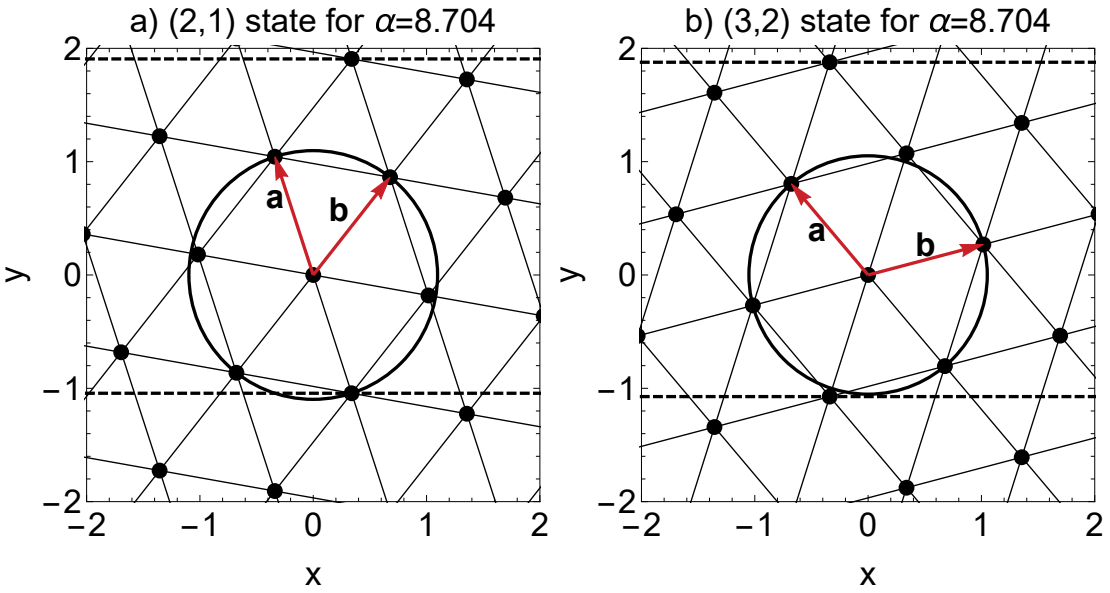

Figure 27: Depictions of the two states at the transition line $\alpha = 8.704$. a) The $(m = 2, n = 1)$ state is in category 3. b) The $(m = 3, n = 2)$ state is in category 5. These diagrams are adapted from [78].

These categories are useful when we consider a generalised form of the lattice. They are located in different parts of an energy curve that enable a direct calculation with just values of m, n, and α.

7.6.2 The Generalised Lattice

To understand where we are so far, we consider a lattice that has the same properties as the set we have generated, but is re-parameterised for simpler analysis. Since we search along $c = n_L$, the size of the unit cell, $c/n_L = 1$. We re-formulate the initial constraints and replace the periodicity constraint with a condition that rotates this lattice such that

the x components of $\mathbf{a}$ and $\mathbf{b}$ are equal and opposite. This is reasonable since we know a global rotation has no effect on the energetics.

$$\hat{\mathbf{z}} \cdot (\mathbf{b} \times \mathbf{a}) = 1 \tag{7.15}$$

$$|\mathbf{a}| = |\mathbf{b}| \tag{7.16}$$

$$\mathbf{a} \cdot \hat{\mathbf{x}} = -\mathbf{b} \cdot \hat{\mathbf{x}}. \tag{7.17}$$

There are now three equations with four unknowns, so we need to introduce a parameter, γ, that defines the lattice.

$$\mathbf{a} = \begin{pmatrix} -\gamma \\ \\ 1/2\gamma \end{pmatrix}, \qquad \mathbf{b} = \begin{pmatrix} \gamma \\ \\ 1/2\gamma \end{pmatrix}. \tag{7.18}$$

Any state previously defined by m, n, and α can be rotated into a state defined by a particular value of γ. The angle of rotation is found numerically in most cases. For example, the state defined by $m = 3$ and $n = 2$ when $\alpha = 8$ can be rotated by 0.3376 radians to match with a value of $\gamma \simeq 0.9368$. This is found using the standard rotation matrix and solving for equal and opposite x components such that $a_x \cos(\theta) - a_y \sin(\theta) = b_y \sin(\theta) - b_x \cos(\theta)$. We can more simply write:

$$\theta = \arctan\left(\frac{a_x + b_x}{a_y + b_y}\right), \qquad 0 \leq \theta < 2\pi. \tag{7.19}$$

The corresponding value of gamma is found by performing the rotation and comparing x components: $\gamma = -(a_x \cos(\theta) - a_y \sin(\theta))$. We now measure the energy of the lattice as a function of γ.

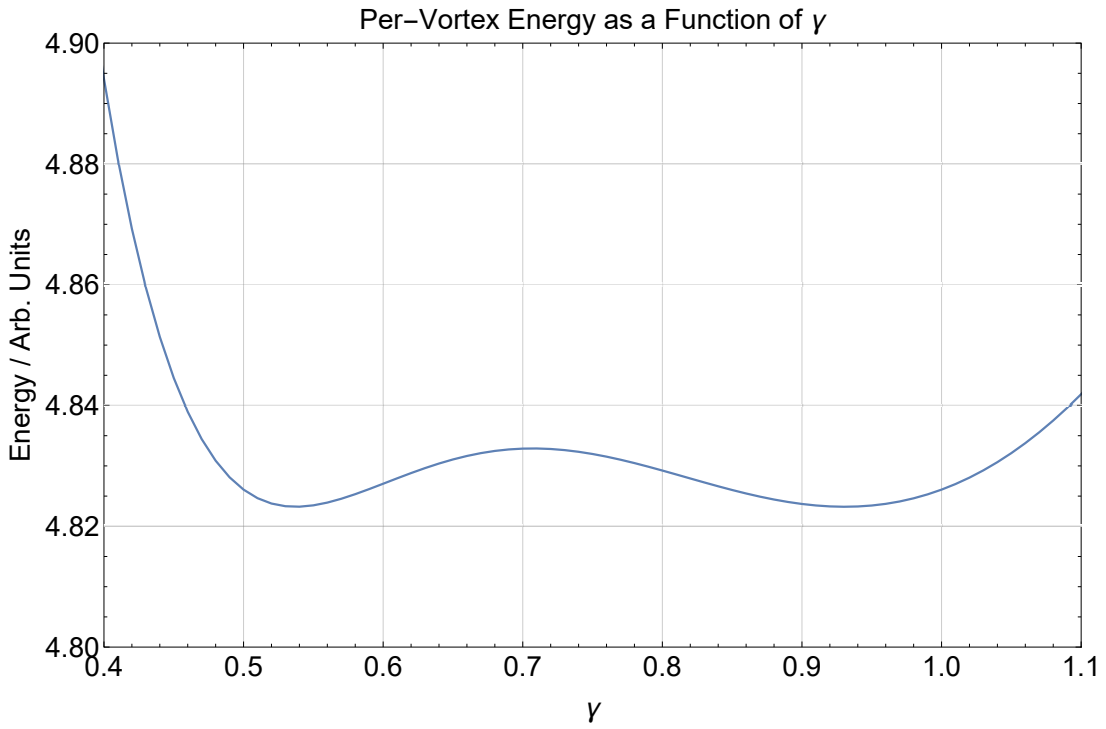

Figure 28: Numerically measured energy as a function of γ. The two minima correspond to the perfect hexatic lattice with values of $\gamma = 1/\sqrt{2\sqrt{3}}$ and $\gamma = \sqrt{3/\sqrt{2}}$. The maximum corresponds to the square lattice where $\gamma = 1/\sqrt{2}$.

Suspecting that the transitions have something to do with the lengths of these vectors, we re-plot the energy with respect to vector length, $L(\gamma) = \sqrt{4\gamma^2 + 1}/2\gamma$, instead making reference to the form of the lattice along the curve. In fig. 29, we find this curve to be parabolic.

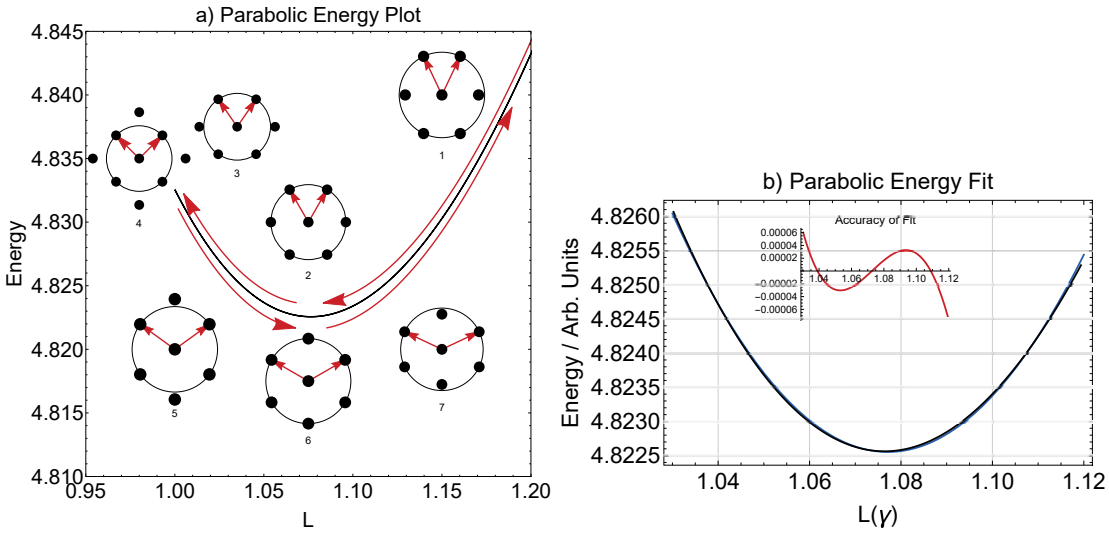

Figure 29: a) Numerically measured energy as a function of vector length. The red arrows indicate the evolution of γ which produces a multi-valued energy curve that essentially overlaps itself. Examples of states from each category are inset. Equivalent definitions of each state exist in terms of γ b) Parabolic fit to the energy curve for $1.03 <= L <= 1.12$, $E(L) \simeq 6.6444 - 3.38278L + 1.57027L^2$. The black and blue curves are the numerical data and fitted function respectively. The fit is performed in this region since we find ground state vector lengths do not exceed this range (except for one case which is accounted for). The accuracy of the fit is inset.

Expressing the category definitions in terms of γ is a matter of solving the original definitions for the generalised lattice.

- (1): $\gamma < 1/\sqrt{2\sqrt{3}}$
- (2): $\gamma = 1/\sqrt{2\sqrt{3}}$
- (3): $1/\sqrt{2\sqrt{3}} < \gamma < 1/\sqrt{2}$
- (4): $\gamma = 1/\sqrt{2}$
- (5): $1/\sqrt{2} < \gamma < \sqrt{\sqrt{3}/2}$
- (7): $\gamma < 1/\sqrt{2\sqrt{3}}$
- (6): $\gamma > \sqrt{\sqrt{3}/2}$

In appendix C, we demonstrate that $E(\gamma) \sim L^2$ with an elastic strain calculation. The parabolic shape is key to solving transition points that are not the result of a global rotation. When the lattice energies are equal, they must either be on the same or opposite sides of the parabola. Since the minimum is exactly halfway between two points at the

same height, each point is a length, d, away from the minimum. The minimum length is given by $\gamma = 1/\sqrt{2\sqrt{3}}$ or $\gamma = \sqrt{\sqrt{3}/2}$, which both give $L = \sqrt{2/\sqrt{3}}$. Between two states, i and j, the energetic equations we solve are when both energies are on the same or opposite side(s) of the parabola. When they are on the same side:

$$L(\alpha, m_i, n_i) = \sqrt{\frac{2}{\sqrt{3}}} \pm d \qquad L(\alpha, m_j, n_j) = \sqrt{\frac{2}{\sqrt{3}}} \pm d. \tag{7.20}$$

Since the right hand sides are equal, these simultaneous equations reduce down to $L(\alpha, m_i, n_i) = L(\alpha, m_j, n_j)$, which is the statement that the lattice vectors are equal in length, so the global rotation transition is recovered. The general solutions to this are:

$$\alpha = \pm \frac{2(n_j m_i + m_j n_i)(m_j m_i + n_j n_i)}{\sqrt{-(m_j - n_j - m_i - n_i)(m_j + n_j + m_i - n_i)(m_j + n_j - m_i + n_i)(m_j - n_j + m_i + n_i)}} \tag{7.21}$$

$$\alpha = \pm \frac{2(n_j m_i - m_j n_i)(m_j m_i - n_j n_i)}{\sqrt{-(m_j + n_j - m_i - n_i)(m_j - n_j + m_i - n_i)(m_j - n_j - m_i + n_i)(m_j + n_j + m_i + n_i)}} \tag{7.22}$$

Provided any of these four solutions gives real and positive results, the transition may be considered.

When the energies are on opposing sides of the parabola, the equations become transcendental:

$$L(\alpha, m_i, n_i) = \sqrt{\frac{2}{\sqrt{3}}} \pm d \qquad L(\alpha, m_j, n_j) = \sqrt{\frac{2}{\sqrt{3}}} \mp d. \tag{7.23}$$

A numerical solution can be derived to arbitrary accuracy with Mathematica's NSolve functionality [9]. Choosing the $(2,1) \rightarrow (3,2)$ transition as an example, we observe the energies on the parabola as α evolves through the transition point in fig. 30.

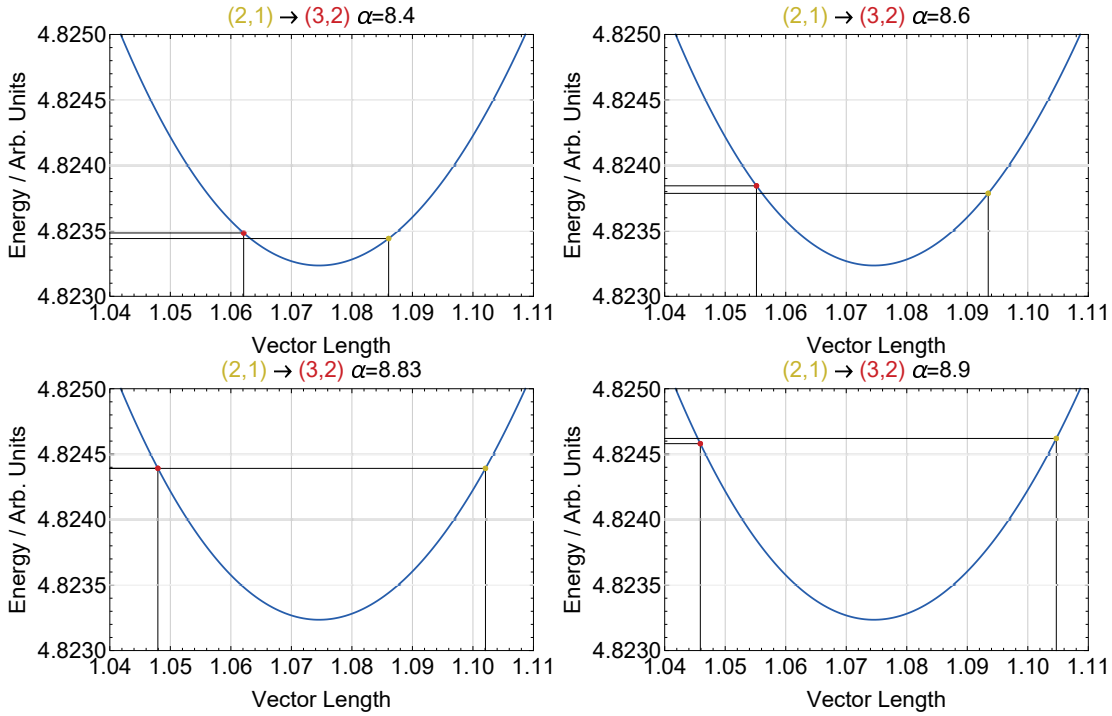

Figure 30: Example of the energy evolution of two states near a transition. The numerically obtained value of $\alpha \simeq 8.83$ for this transition varies from the transcendental value of $\alpha = 8.704$.

The accuracy of this method is subject to the parabolic approximation holding without higher order terms affecting the curve. Since this is an approximation and there is measurable (although small) error, the values of alpha we obtain are approximate. Since the model we use describes the physics of the lattice near the perfect hexagonal lattice, these results are acceptable provided the transitions occur close to $L = \sqrt{2/\sqrt{3}}$ such that the parabolic approximation holds. In all cases we examine, this approximation does hold. Including higher order terms would complicate the model since it relies on a parabolic form.

7.6.3 Algorithm for Finding Ground States

With the developed model for finding transition points, we construct an analytical algorithm that generates the phase space with minimal computational effort. Firstly, we need to ensure that we include all values of m and n that generate perfect lattices in the region of α that we probe.

The perfect lattice with the lowest value of α is $\alpha^-_\triangle = 2(m^2 - mn + n^2)/\sqrt{3}$. If we find the minimum value of $\alpha^-_\triangle$ for a given value of m, we can set the maximum value of m to be one less than what would take $\alpha^-_\triangle$ over the maximum required value. Differentiating with respect to n, while fixing m, gives $\partial\alpha^-_\triangle/\partial n = 2(2n - m)/\sqrt{3} = 0$ which gives $n = m/2$. This is a minimum since $\partial^2\alpha^-_\triangle/\partial n^2 = 4/\sqrt{3} > 0$. Substituting back into the original formula and rearranging gives the formula for the maximum value of m that should be considered:

$$m_{\mathrm{MAX}} = \left\lfloor \sqrt{\frac{2\alpha_{\mathrm{MAX}}}{\sqrt{3}}} \right\rfloor . \tag{7.24}$$

Our results will be in the region $0.5 \leq \alpha \leq 100$, so we use a maximum value of $m = 10$ and sample all valid values of m and n up to it.

The algorithm then generates a list of all values of $\alpha_\triangle$ and sorts them into ascending order. We know the ground state is given at these points; it is a matter of stitching them together with transition points. We argue that for $\alpha = 0$, the cylinder is 1D and the ground state must be a single chain of evenly spaced vortices. The only state we have

that describes this is the (1,1) state which reduces to a single chain if $c = 0$. With this, we set the default ground state for $\alpha = 0$ to be the $(1, 1)$ state, search for the next highest value of $\alpha_{\triangle}$, and find the transition point. This is also readily shown with Monte Carlo simulations of the system provided care is taken to ensure that enough copies of the small cylinder are considered in the periodic boundary condition.

To find the correct transition point, the algorithm compares all solutions for the transition equations between all left and right minima and chooses the lowest value of α which is above the left minimum. An additional check is carried out to see if there are further transitions between the new state to the right minima. This method will largely give the correct ground states, where deviations are due to the breakdown of the parabolic approximation of the energy, and the incorrect state is chosen over another that is nearby. Errors should be confined between energetic minima given by $\alpha_{\triangle}$ since they are well-defined and known to be ground states. The script is shown in appendix D.

7.7 Translating to the Phyllotactic Notation

Expressing these results with the phyllotactic notation puts them into context with existing literature and reveals a clear trend in the structure of states as a function of α.

By observing the energetic sampling graph, we know that the square lattice occurs at a value of α between the two energetic minima of hexagonal lattice (each with a different primitive lattice vector). The square lattice acts as the divider between the two possibilities, so provided we know which side of it we are on, we know which vector to use.

We can find the value of α for which the square lattice forms, $\alpha_{\square}$, by setting $|\mathbf{a}+\mathbf{b}| = |\mathbf{a}-\mathbf{b}|$. We find $\alpha_{\square} = m^2 + n^2$. If $\alpha < \alpha_{\square}$ then $\mathbf{c}^+$ is the primitive vector, or if $\alpha > \alpha_{\square}$ then $\mathbf{c}^-$ is the primitive vector.

7.7.1 Where $\mathbf{c}^-$ is the Primitive Vector

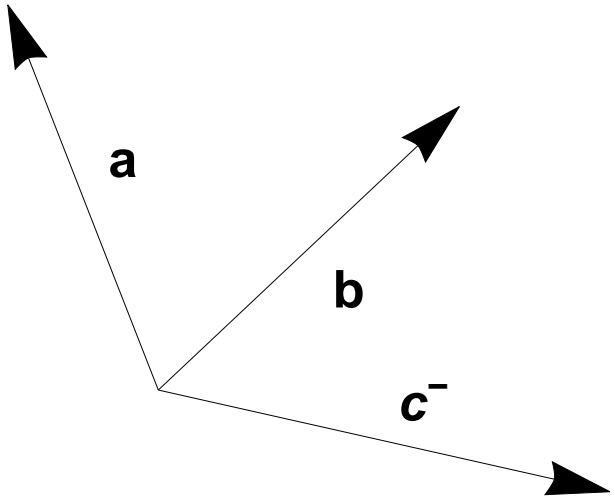

Figure 31: Illustration of $\mathbf{c}^-$ with respect to $\mathbf{a}$ and $\mathbf{b}$.

Given that:

$$\mathbf{c}^- = \begin{pmatrix} (m+n)/\sqrt{\alpha} \\ \frac{-(m+n)\alpha-(m+n)\sqrt{\alpha^2-(m^2-n^2)^2}}{(m^2-n^2)\sqrt{\alpha}} \end{pmatrix}, \tag{7.25}$$

we can see that $\mathbf{c}^-$ subtends the largest angle with the periodicity vector, $\mathbf{V}$. We therefore follow N units of $\mathbf{a}$ and $\mathbf{b}$ such that N units of $\mathbf{c}^-$ form a triangle that includes the point described by $\mathbf{V}$. If we move N units of $\mathbf{a}$ and M units of $\mathbf{c}^-$, where $M < N$, we can

construct $\mathbf{V}$.

$$N\mathbf{a} + M\mathbf{c}^- = \mathbf{V} \tag{7.26}$$

$$N\mathbf{a} + M(\mathbf{b} - \mathbf{a}) = \mathbf{V} \tag{7.27}$$

Using the definition:

$$m\mathbf{a} + n\mathbf{b} = \mathbf{V}, \tag{7.28}$$

we see that $N = m + n$ and $M = m$. From the other way around (moving L units of $-\mathbf{c}^-$):

$$N\mathbf{a} - L\mathbf{c}^- = \mathbf{V} \tag{7.29}$$

$$N\mathbf{a} - L(\mathbf{b} - \mathbf{a}) = \mathbf{V}, \tag{7.30}$$

we get the same result for N and find $L = m$. This translates to the phyllotactic notation of (N, L, M), or $(m + n, m, n)$ as described in fig. 14.

7.7.2 Where $\mathbf{c}^+$ is the Primitive Vector

In this case, we see that:

$$\mathbf{c}^+ = \begin{pmatrix} (m-n)/\sqrt{\alpha} \\ \frac{(m-n)\alpha + (m-n)\sqrt{\alpha^2 - (m^2-n^2)^2}}{(m^2-n^2)\sqrt{\alpha}} \end{pmatrix}. \tag{7.31}$$

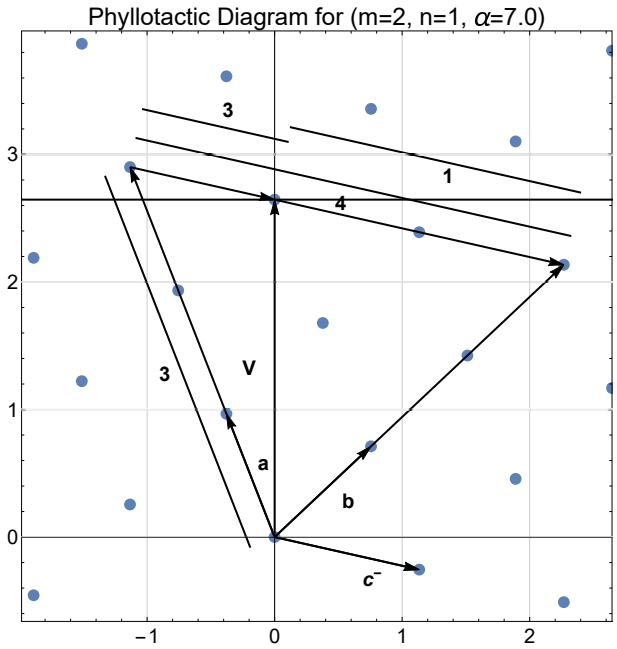

Figure 32: Example of a state where $\mathbf{c}^-$ is the primitive vector. Diagram adapted from [78].

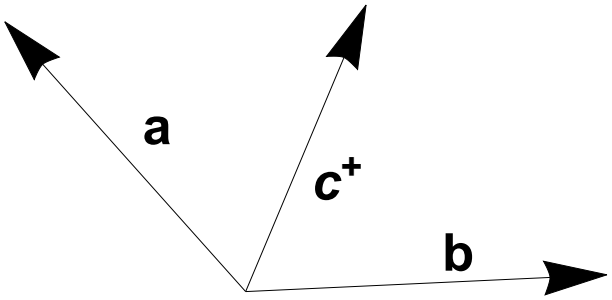

Figure 33: Illustration of $\mathbf{c}^+$ with respect to $\mathbf{a}$ and $\mathbf{b}$.

This leaves $\mathbf{b}$ with the largest angle with respect to $\mathbf{V}$. Similar to before, we follow N units of $\mathbf{a}$ and M units of $\mathbf{b}$. From our previous definition, we immediately find $N = m$ and $M = n$. The other path of N units of $\mathbf{c}^+$ and L units of $-\mathbf{b}$ looks like:

$$N\mathbf{c}^+ - L\mathbf{b} = \mathbf{V} \tag{7.32}$$

$$N(\mathbf{a} + \mathbf{b}) - L\mathbf{b} = \mathbf{V}. \tag{7.33}$$

We see that $L = m - n$ and the phyllotactic notation becomes $(m, n, m - n)$.

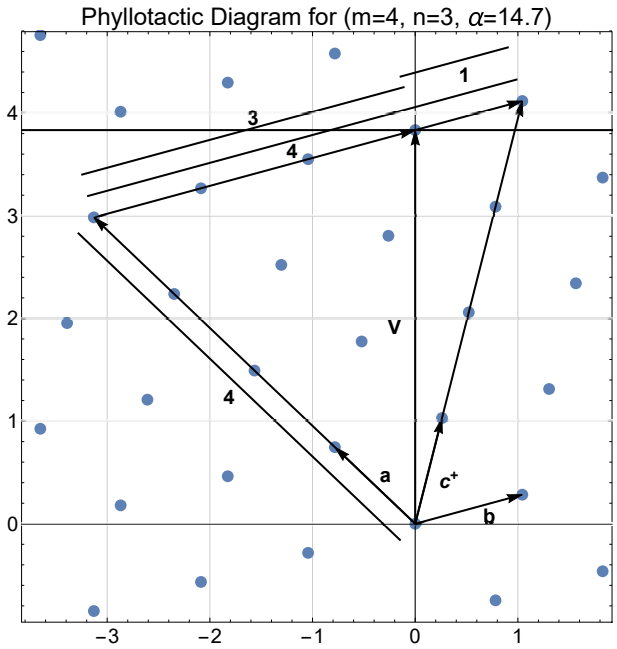

Figure 34: Example of a state where $\mathbf{c}^+$ is the primitive vector. Diagram adapted from [78].

7.8 The Phase Diagram

Using the script presented in appendix D, we generate a list of all transitional values of α up to $\alpha = 60$, shown in fig. 35, and represent the phase diagram up to $\alpha = 25$ in fig. 36.

7.9 Remarks

We have considered a cylindrically confined system of vortices to isolate the effect of width in determining lattice structure in vortex channels. Free from dislocations, we find a progression of row number with width. The dimensionless quantity, α, enables us to scale out the circumference and density, giving us a simpler system to consider. Using geometric and numerical arguments, we find there are two types of transition, one being a sub-set of another. The simpler transition is when two lattices can be globally rotated into one another. The other transition is best considered by calculating the per-particle energy of the lattice as a function of lattice vector length. The energy curve is parabolic;

α_T	(m,n)	Phyllotactic	α_T	(m,n)	Phyllotactic
0	$(1,1)$	$(1,1,0)$	26.5461	$(5,5)$	$(5,5,0)$
2	$(1,1)$	$(2,1,1)$	30	$(3,3)$	$(6,3,3)$
4	$(2,2)$	$(2,2,0)$	31.7613	$(4,2)$	$(6,4,2)$
$8\sqrt{3/5}$	$(2,1)$	$(3,2,1)$	34.0042	$(6,5)$	$(6,5,1)$
8.7042	$(3,2)$	$(3,2,1)$	38.7034	$(6,6)$	$(6,6,0)$
9.1912	$(3,3)$	$(3,3,0)$	$504/\sqrt{143}$	$(4,3)$	$(7,4,3)$
12	$(2,2)$	$(4,2,2)$	43.9001	$(5,2)$	$(7,5,2)$
14.4506	$(3,1)$	$(4,3,1)$	46.0082	$(7,5)$	$(7,5,2)$
14.6765	$(4,3)$	$(4,3,1)$	47.2565	$(7,6)$	$(7,6,1)$
16.7283	$(4,4)$	$(4,4,0)$	$416/3\sqrt{7}$	$(4,4)$	$(8,4,4)$
$160/3\sqrt{7}$	$(3,2)$	$(5,3,2)$	56	$(7,7)$	$(7,7,0)$
23.0956	$(5,4)$	$(5,4,1)$	58.4359	$(6,2)$	$(8,6,2)$

Figure 35: Table of transition points. The value of α_T given is the transition point between the listed state and the one before it, starting from 0 and ascending.

we exploit this property to write down a simple (although transcendental) equation that we numerically solve to arbitrary accuracy.

Since the phase diagram is symmetric under interchange of c and n_L, the problem is strongly dependent on geometry, as opposed to the interaction profile. This is an important fact; these results should apply to many repulsive soft particle systems.

In terms of the wide, confined flow channel, which is of constant width, we know the row-drops are caused at critical values of density and the boundaries play a minor role in determining the positioning of a transition point.

Considering the results of the parabolic channel, first reported in [89] and reproduced in section 4.1, we see that there is a much larger set of possible states that can form on the cylinder. A subset of the states we observe are aligned in the toroidal direction,

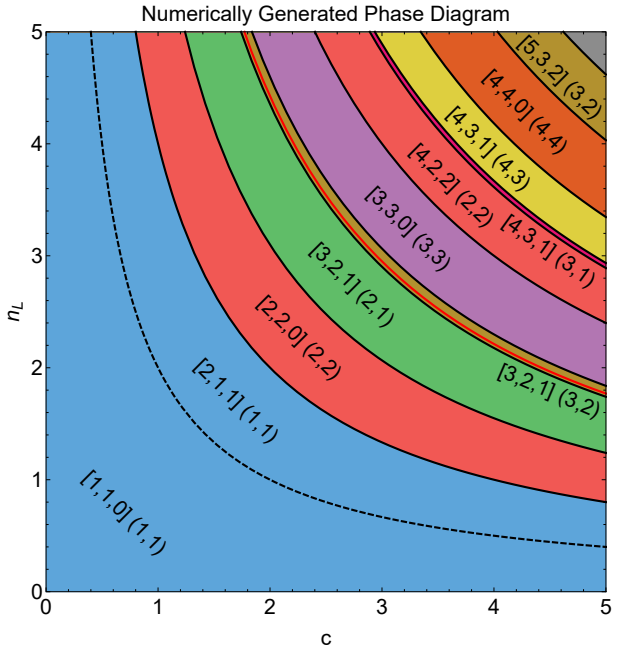

Figure 36: Phase diagram up to $\alpha = 25$. There is a discrepancy between energetic sampling calculations and the result found using eq. (7.23) for the $(2,1) \to (3,2)$ transition. The red line indicates the result from energetic sampling and the black from the analytic solution. The dashed line represents a change of phyllotactic notation, but where the lattice is continuously deforming.

such as the $(2,1,1)$ and $(2,2,0)$ states, which bear closest resemblance to the states in the parabolic channel. Since there is no energetically favourable position due to a background potential on the chains, all remain equally spaced and homogeneous. We use similar techniques of per-particle energetic sampling and constructing states based on the symmetries present to construct the phase diagram numerically and analytically.

In the next section, we study a channel with varying width and density. We are interested to study the effects of varying both, and whether we can control the structure of the lattice by carefully choosing a combination of density and width.

8 Vortex Flow in a Conical Flow Channel

Expressing the general properties of the cylinder in terms of α provides an effective basis for our calculations. If known, α alone dictates the ground state structure on the cylinder. In this section, we generalise α onto a more complicated geometry: one that resembles a cone. Using ideas from continuum flow, we create a lattice flow between a source and sink reservoir to be single phase. Using α as a reference, we demonstrate a defect-free flow, where the density gradient due to the source and sink balances with the varying circumference of a cone.

If the circumference of the cylinder varies linearly, a static lattice with constant density will become unstable as it strains into an energetically unfavourable position. A transition between two phyllotactic states occurs which lowers the energy of the otherwise strained part of the lattice. This picture is reversed in [111, 112], but shows the same effect; the system has a constant width, but the density changes. There is a critical point, where a row-drop transition occurs because the lattice strains too much. This balance between width and density is investigated further in this section. We will focus on the problem of coordinating width and density to guarantee a single phase throughout the system.

Previous results on the channel confined by a pinning array are characterised by:

- Dislocation pairs forming between row-drop transitions due to the incommensurability of two adjacent lattices.

- Geometrically Necessary Dislocations (GNDs) forming along the edges of the channel that interact with row-drop dislocations to reflect them back into the channel and move through to control the transitions.

- Source dislocations formed by the high level of disorder at the ends of the channel that can leak into the main flow.

Since we know that a pinned channel edge causes additional dislocations of GND type, even without a density gradient, we study a cone-like channel which provides a cleaner system to study, much like the cylinder.

We begin by numerically studying the static behaviour to specify which type of transition occurs and how α translates onto the cone. The notion of a number-per-unit length, or 'linear density', works on the cylinder because the vertical dimension is a constant width and therefore scales out. More generally, in terms of the true 2D density, ρ, we find an alternative definition for α. From the definition of $n_L = n/l$ and $\rho = n/cl$, we find $n_L = c\rho$. In a system where c is variable, the *local* value of α at a position x is $\alpha = c^2(x)\rho(x)$.

Analogous to the density driven lattice [111, 112], we employ a source/sink system of vortices to populate and flow along the cone's length. Experimentally, by controlling the local magnetic field strength at these locations, a certain number of vortices will be induced. For example, on the left-hand source, the number of vortices is $N_L = B_L/\Phi_0$. Vortices will extrude themselves through the channel and eventually form a density gra-

dient that will cause the entire lattice to flow from source to sink.

Since we employ an energetic approach to these systems, our interest in dislocations is only to identify them and show that they also control transitions between phyllotactic states (previously described as row-changes). Since we aim to control the flow to be free of dislocations, we do not consider dislocation dynamics. We also investigate the properties of source dislocations when there are no dislocations to remove them. The dislocation removal mechanism is due to the left most row-drop dislocation interacting with a source dislocation, and both combining to a new dislocation with a different Burgers vector (a quantifier of dislocations on regular lattices).

8.1 Periodic Boundary Conditions

When we implement periodic boundary conditions on a cone-like geometry, the meaning of inter-particle distance must be considered. A natural setting would be to calculate geodesics on the surface of the cone to find arc lengths to repeated patterns. This can be problematic near to the ends of the cone as geodesics wrap around the ends and become discontinuous due to the sudden cut-off of the system. Because the surface we model in the related cylindrical system is flat, the geodesic method assumes a curved surface which further complicates the problem. Our aim is to model a flat surface with a periodic boundary condition and increasing width. We instead opt for a simpler scheme that neatly generates a repeated lattice: rotation.

By mapping the lower edge onto the upper edge, we copy over the entire system while maintaining its undistorted structure. Figure 37 shows an example of how this is implemented. Provided we set the system width wide enough, only one image is needed above and below to keep all interactions within the cut-off length. For a cone of length, L, and left and right widths, c_L and c_R, respectively, the scheme is as follows:

- Extend the cone to an isosceles triangle by adding length $c_L L/(c_R - c_L)$ to the trapezium net.
- Apply the extension to a vortex at position $\mathbf{r} \to \mathbf{r} + c_L L/(c_R - c_L)\hat{\mathbf{x}} \equiv \mathbf{r}'$.
- Rotate $\mathbf{r}'$ through angle $\theta = 2\arctan(c_R - c_L)/2L)$ and subtract the excess length: $\mathbf{r}^{\mathrm{u}} = \mathbf{r}' \cdot \mathbf{M}[\theta] - c_L L/(c_R - c_L)\hat{\mathbf{x}}$ and $\mathbf{r}^{\mathrm{d}} = \mathbf{r}' \cdot \mathbf{M}[-\theta] - c_L L/(c_R - c_L)\hat{\mathbf{x}}$. The usual rotation matrix is denoted by $\mathbf{M}$.
- Repeat for all vortices in the system to generate 'channel edges' populated by a lattice of vortices that are interacted with.

New positions of vortices in the original channel are then calculated based on the positions of the images. Although possibly contentious, this scheme is simple and generates results congruent with our cylinder calculations.

8.2 Static Behaviour

Initially, we simulate the system without a source/sink mechanism in order to study ground states when vortices are left to relax. We have already seen in section 7.2, on the cylinder, the ground states are best found using Monte Carlo routines. We populate a

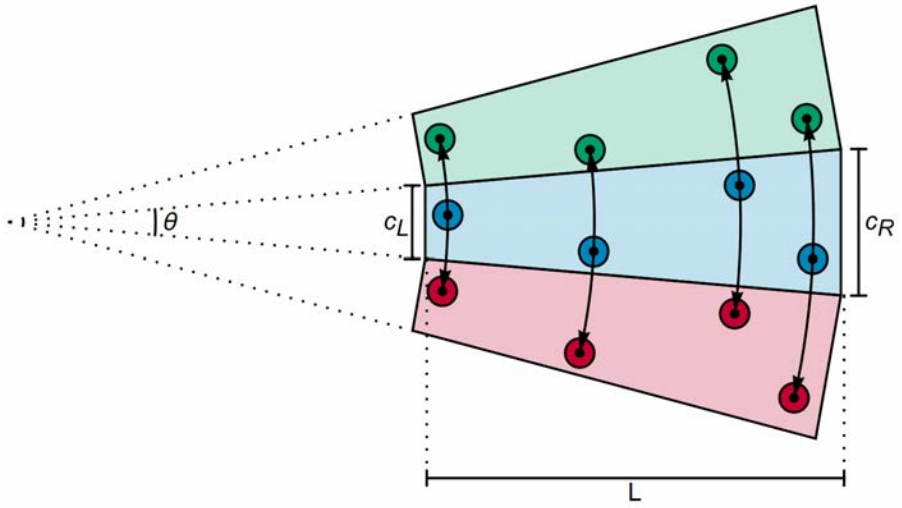

Figure 37: Diagram showing the rotation scheme (not to scale). Vortices are imaged above and below the original channel by extending the trapezium to an isosceles triangle.

range of different channel sizes from $4.0 \leq c_L \leq 10.0$ and $4.5 \leq c_L \leq 10.5$ with a range of vortex numbers from $100 \leq N_v \leq 256$. We anneal a temperature of $T = 0.001$ down to zero and check a set of snapshots outputted during simulation to check which one had the lowest internal energy: this one is selected as the best approximation to the ground state. This is because the state observed when $T = 0$ can be metastable and another state, even at slightly higher temperature, can have a lower internal energy.

The general findings are consistent with the cylinder when we compare the local value of α at a transition with the predictions made in fig. 35. In fig. 38, we see that the expected transition point is $\sim 9\%$ higher than our measurement. This is because there are four competing states with comparable energies in that particular system ($(4,2,2)(2,2)$, $(4,3,1)(3,1)$, $(4,3,1)(4,3)$, and $(4,2,2)(4,2)$). In fig. 39, the transition point is much closer to the expected value and there is only one other competing state nearby. If there are fewer nearby states interfering, the system can relax more cleanly since it has fewer energetically favourable options.

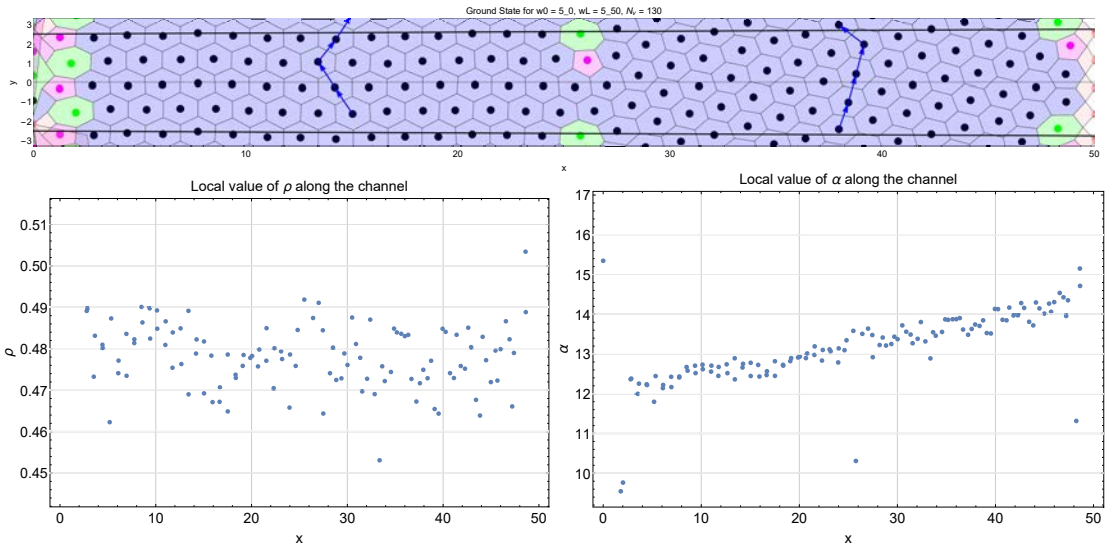

Figure 38: Ground state for $cL = 5.0$, $cR = 5.5$, and $N = 130$. A $(4, 2, 2)$ state on the left is separated by a $(4, 3, 1)$ state on the right by a pair of dislocation vortices at $x \simeq 26$. Referring to the local value of α at the transition point by linear interpolation of the data we find $\alpha \simeq 13.3$. The predicted transition point is $\alpha \simeq 14.5$. The next lowest transition point is $\alpha = 12$ so no additional states are interfering. The density plot shows an average density of $\bar{\rho} \simeq 0.479$ with standard deviation $\sigma \simeq 0.0246$. Only data for $5 < x < 45$ is used for interpolation and averaging due to distortions near the ends.

Previous research indicates the flow induced by a density difference has row-changing transitions mediated by a pair of dislocation vortices [111, 112]. This property is also observed on the conical geometry, as evidenced by fig. 38. Occasionally, an entire grain boundary can form if the angle between two states is sufficiently high, shown in fig. 39. Since dislocations inherently raise the energy of the system, their presence in a non-transient state must lower the energy of the two competing lattices that become strained as they deviate away from perfect hexagonal structures as the width changes.

Since using the notion of a local value of α matches with predictions from the cylinder, we conclude that its use on the cone is sensible and justified. Although the annealing process introduces difficulties when searching for the true ground state, we observe the

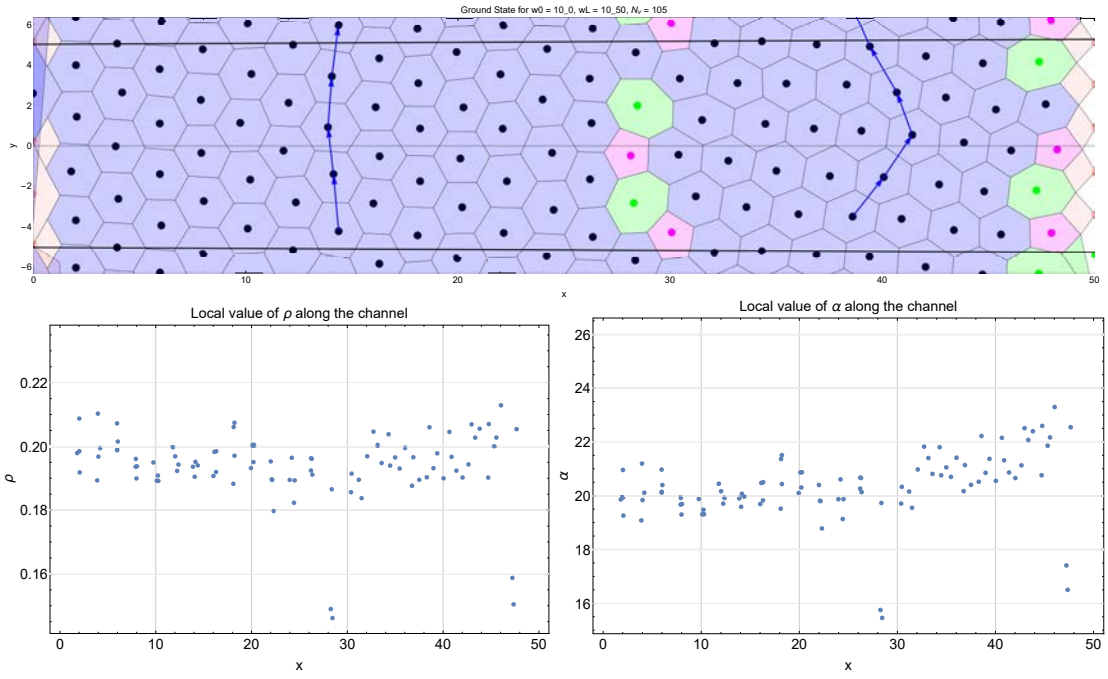

Figure 39: Ground state for $cL = 10.0$, $cR = 10.5$, and $N = 105$. A $(4, 4, 0)$ state on the left is separated by a $(5, 3, 2)$ state on the right by a two pairs of dislocation vortices at $x \simeq 29$. Referring to the local value of α at the transition point by linear interpolation of the data we find $\alpha \simeq 20.5$. The predicted transition point is $\alpha \simeq 20.15$. The density plot shows an average density of $\bar{\rho} \simeq 0.196$ with standard deviation $\sigma \simeq 0.0157$. Only data for $5 < x < 45$ is used for interpolation and averaging due to distortions near the ends.

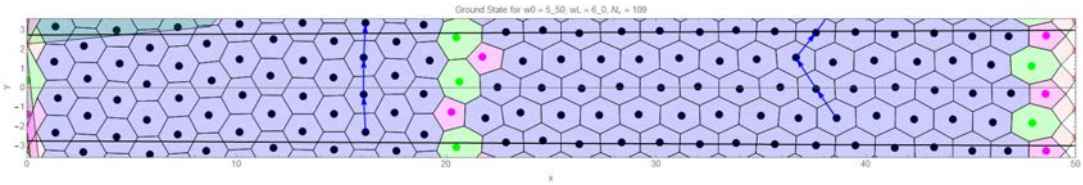

Figure 40: Ground state for $cL = 5.5$, $cR = 6.0$, and $N = 109$. The $(3, 3, 0) \to (4, 2, 2)$ transition occurs over a grain boundary formed of two dislocation pairs.

correct structural states on either side of a transition when the local value of α is compared to predictions in the previous chapter. Since α dictates which state is present and the circumference changes along the channel, if we intend to hold α constant, we must find a way to vary density to balance $\alpha = c^2\rho$.

8.3 Populating the Source and Sink

If we work with a fixed value of α, ρ and c are both required to vary along the channel. Considering an infinitesimal slice of area is given by $c(x)\delta x$, multiplying area and density gives the vortex number. Integrating along the length of the source or sink, starting at x_0 and ending at x_s, the number of vortices required to fix α is as follows:

$$N_s = \int_{x_0}^{x_s} \rho(x)c(x)\mathrm{d}x \tag{8.1}$$

$$= \alpha \int_{x_0}^{x_s} \frac{c(x)}{c^2(x)}\mathrm{d}x \tag{8.2}$$

$$= \alpha \int_{x_0}^{x_s} \frac{\mathrm{d}x}{\left(c_L + \frac{c_R - c_L}{L}x\right)} \tag{8.3}$$

$$= \frac{\alpha L}{c_R - c_L} \log\left[\frac{Lc_L + (c_R - c_L)x_s}{Lc_L + (c_R - c_L)x_0}\right]. \tag{8.4}$$

This formula directly tells us how to populate the source/sink. We must round N_s to the nearest integer which can cause our local values of α to change along the channel. The system is robust enough to work given small changes in α, provided we choose values without many competing states.

Our scheme for vortex placement is to count the number of vortices in the source and sink during each incrementation. We incrementally add or remove vortices, at random, as

required to populate the reservoirs. This process introduces noise into the channel; this scheme will also demonstrate the robustness of the single-phase lattice in the channel from fluctuations. If it is insensitive to a disordered lattice on either end, then the results do not depend on very specific conditions and can be confidently applied to similar systems.

8.3.1 Left and Right Edges

Since the left and right ends of the channel are separate (not connected by a periodic boundary condition), we must find an alternative boundary scheme. We apply a reflective boundary: vortices at the ends of the channel see a reflected image of themselves over the boundary. This image vortex causes additional repulsion that confines vortices inside the channel. Figure 41 shows the left boundary for reference. In reality, vortices are repelled by the boundaries of samples due to flux penetrating around the edges of the sample at lengths below the penetration depth [21]. The vortex image force is actually attractive since an image would be rotating in the opposite direction. Future work should address this issue, although it is minor since vortices are still repelled at the boundary by an exponentially decaying force, similar to a vortex-vortex interaction. Naturally, the unit cells on the ends are distorted away from any lattice that would form in the channel (except for some special cases). This boundary is designed to make sure the unit cells of the end vortices approximately fill the source/sink completely. Hard walls will result in some vortices existing exactly on the edge which means half of their unit cells will leak out of the system, lowering the expected density.

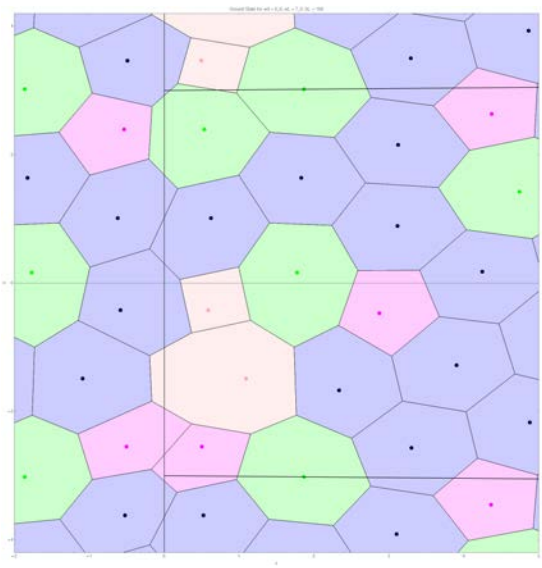

Figure 41: Example of unit cells near to the left end boundary. The lattice is not homogeneous in the source due to the large fluctuations that occur when a vortex is placed or removed. The vortices closest to the end approximately have the same amount of their unit cells outside the boundary as image unit cells do inside the boundary.

8.4 Calibrating the Source and Sink

To ensure α varies as little as possible along the channel, we calculate an analytic expression that enables optimal calibration with minimal variation. We establish an expression for the variance of density using continuous flow ideas and combine with our definition of α and optimise.

8.4.1 Continuous Flow in 2D

In order to get an expectation for how density varies along the channel, we can exactly solve the continuous flow scenario in 2D. The flow from the source to sink is described by the diffusion equation for the continuous density field, $\phi(r, t)$:

$$\nabla^2\phi - \frac{1}{D}\frac{\partial\phi}{\partial t} = 0, \tag{8.5}$$

assuming the diffusion coefficient is constant. Since we are interested in the steady state behaviour, the time derivative is taken as zero and the equation reduces to Laplace's equation. The solutions are found by separation of variables such that $\phi(x, y) = X(x)Y(y)$. Since the terms are separable, $X''/X = -Y''/Y = -\Omega^2$, where Ω is an arbitrary constant that arises due to the essential invariance of the other two terms. Initially solving gives:

$$\phi(x, y) = (a \sin(\Omega x) + b \cos(\Omega x))(c \sinh(\Omega y) + d \cosh(\Omega y)). \tag{8.6}$$

In order to satisfy the left and right boundary conditions, $\phi(0, y) = \phi_L$ and $\phi(L, y) = \phi_R$, Ω must be set to zero to prevent any y dependence. The differential equations then reduce to a simpler form with polynomial solutions: $X'' = -Y'' = 0$. Solving this yields: $\phi(x, y) = (ax + b)(cy + d)$. The boundary conditions mean that $c = 0$ to remove any y dependence. Since d can be absorbed into the other constants, it can be readily shown that:

$$\phi(x, y) = \phi(x) = \frac{\phi_R - \phi_L}{L} x + \phi_L. \tag{8.7}$$

We conclude that the density in a simple flow channel will vary linearly along the length of the channel. For simplicity, we approximate the discrete flow with the continuous expression to give:

$$\rho(x) = \frac{\rho_R - \rho_L}{L} x + \rho_L, \tag{8.8}$$

where ρ_L and ρ_R are the left and right density in the source/sink. For the values we use, the linear term is small ($\rho(x) = 0.01x + 4.0$ for example) and the density appears constant, as it does in figs. 38 and 39.

Similarly, we recall from eq. (8.1) that the variance of $c(x)$ has a similar form to eq. (8.8):

$$c(x) = \frac{c_R - c_L}{L} x + c_L. \tag{8.9}$$

8.4.2 Minimising $\alpha(x)$ Along the Channel

We now have the expressions required to minimise α along the channel. We generate expressions for optimal densities in the source and sink reservoirs needed to maintain an almost-constant $\alpha(x)$. Considering the width dependence on α,

$$\alpha(x) = c^2(x)\rho(x) \tag{8.10}$$

$$= \rho(x) \left[c_L^2 + 2\frac{c_R - c_L}{L} x + \frac{(c_R - c_L)^2}{L^2} x^2 \right]. \tag{8.11}$$

The quadratic term in x is suppressed by a factor of 10000 for our typical values of $c_R - c_L = 0.5$ and $L = 50$. We omit the quadratic term which means we consider only linear variations in $c(x)$. Substituting into eq. (8.8) gives:

$$\alpha(x) = \left(\frac{\rho_R - \rho_L}{L} x + \rho_L \right) \left(c_L^2 + 2\frac{c_R - c_L}{L} x \right) \tag{8.12}$$

To minimise the variation in α, we fix the minimum of α to be in the centre of the channel. Since α is quadratic, the lowest gradients are closest to the extremum, and since it is symmetric about this point, the variance is minimised. Setting $\mathrm{d}\alpha/\mathrm{d}x|_{x=L/2} = 0$, we find:

$$\rho_L = \rho_R \left(1 + \frac{c_R - c_L}{c_L^2}\right). \tag{8.13}$$

Hence there is an optimal ratio of ρ_L and ρ_R that minimises α dependence.

Furthermore, we choose the value of α in the centre of the channel to be a 'stable' value (deep within a single phase where there are as few as possible competing states) such that variation away from this on the phase diagram is minimal. This also enables us to calculate ρ_L and ρ_R that we apply to the simulations.

We define the centre value of α, ρ, and c to be α_C, ρ_C, and c_C respectively. Since $\alpha_C = c_C^2 \rho_C$ and $\rho_C = (\rho_L + \rho_R)/2$:

$$\alpha_C = c_C^2 \frac{\rho_R + \rho_L}{2} \tag{8.14}$$

$$= \rho_R \frac{c_C^2}{2} \left(2 + \frac{c_R - c_L}{c_L^2}\right). \tag{8.15}$$

We now have expressions for the optimal values:

$$\rho_L = \frac{2\alpha_C \left(c_L^2 + c_R - c_L\right)}{c_C^2 \left(2c_L^2 + c_R - c_L\right)} \tag{8.16}$$

$$\rho_R = \frac{2\alpha_C c_L^2}{c_C^2 \left(2c_L^2 + c_R - c_L\right)}. \tag{8.17}$$

For example, if we choose $\alpha_C = 18$, $C_L = 6.0$, and $c_R = 7.0$, we expect the $(4, 4, 0)$ state to form and remain throughout the channel if $\rho_L = 0.43187$ and $\rho_R = 0.42020$. This corresponds to $N_L = 13.01 = 13$ and $N_R = 14.65 = 15$. Simulating this and recording the steady state shows that the theory works in this case, as seen in fig. 42.

8.5 Results

We test our optimised equations by selecting stable values of α for various combinations of c_L and c_R. Single phase flow is readily observed for: $(4, 4, 0)$ near to $\alpha = 18$, $(3, 3, 0)$ near to $\alpha = 10$, $(2, 2, 0)$ near to $\alpha = 5$ and $(4, 2, 2)$ near to $\alpha = 8.5$.

Occasionally, source dislocations leak into the channel. Since there are no other dislocations present in the channel, the source dislocation will flow from end to end unimpeded. It is a matter of further work to find alternative ways to control the source and sink to prevent dislocations leaking out.

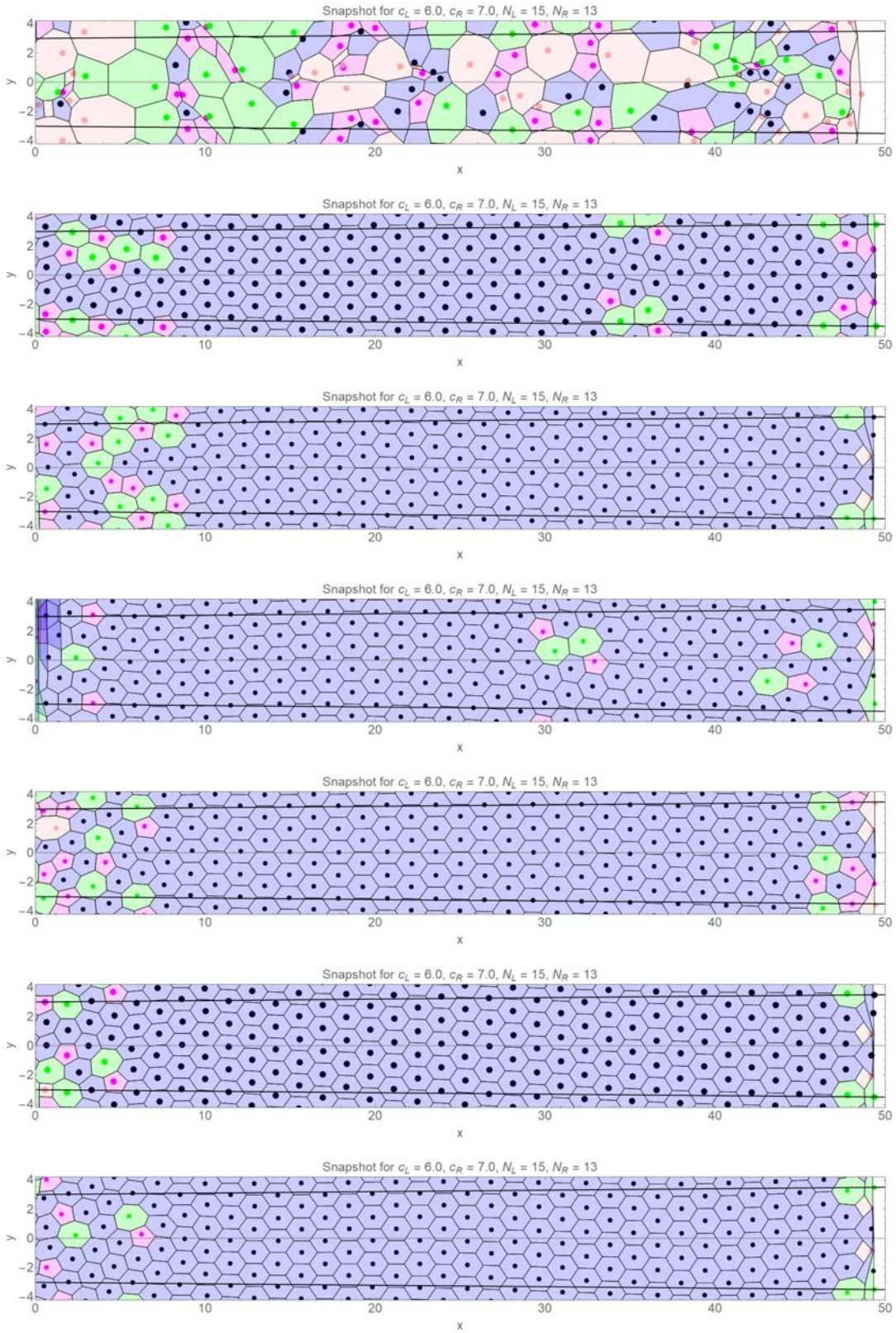

Figure 42: Snapshots of the density driven cone system with $c_L = 6.0$, $c_R = 7.0$, $N_L = 15$, and $N_R = 13$. The evolution of the lattice towards steady state is shown with snapshots separated by $250,000$ time increments. Occasionally, dislocations leave the source and travel through the entire system since there is no mechanism to absorb them, unlike the parabolically confined channel [111, 112]. The single phase in this case is stable for at least $4,500,000$ time increments.

8.6 Remarks

By studying a cone-like geometry with a source and sink mechanism, we have demonstrated the importance of both width and density in confined vortex systems.

Varying width causes a flowing lattice to strain, eventually beyond a critical point, and transition to another phyllotactic state. These transitions are mediated by one or more pairs of dislocation vortices at the interface between the two states. This result is in agreement with [111, 112] where dislocation pairs control the row-drop transition.

We knew from the results on the cylinder that varying density in a constant-width system also induces transitions via lattice strain. By finding a balance between density and width, we have shown that single-phase flow is possible on the conical geometry by controlling source and sink densities. By optimising the source and sink, the variance of α is minimised such that it is always in the region of a single phyllotactic state as shown in section 7.

Given that we have extensively studied the effects of width and density without the additional complication of the shape of the boundaries, we move onto a thin constricted flow channel in section 9.

9 Vortex Flow in a Narrow Channel with a Constriction

We know from our own and previous research [111, 112] that density driven flow leads to dislocation-mediated row-changes. In sections 7 and 8, we have shown we can predict the structures that form and describe them in terms of the phyllotactic notation. We have also demonstrated we can fine-tune the (dis)appearance of dislocations on the cone-like geometry by balancing channel width and density. In this section, we focus on a single, artificially induced dislocation caused by a constriction in an already narrow channel. The channel is three rows wide, and constricts to the width commensurate for a single row.

We study a constricted narrow channel that forces a row drop due to a potential barrier. Flowing vortices jam and build a structure of increasing row numbers that recombine to a single chain. The channel width is commensurate with two or three rows of vortices; dislocation dynamics are therefore not visible in this system. We focus instead on flow patterns and chain structures to classify the properties of multiply-recombining rows. We focus on increasing driving force and global density; source and sink systems are too sensitive to noise for this narrow configuration. The constriction geometry is shown in fig. 43.

Furthermore, we are able to tune this highly controllable system into chaotic flow states and observe discrete versions of stagnation and turbulence. This arises for one of two reasons: the driving force can dominate the dynamical response of the vortices or two competing flow patterns overlap. Competing flow patterns are observed on the phase diagrams we present of Lyapunov exponents and fractal dimensions near to transition lines between patterns, akin to a thermodynamic system going critical near a phase transition.

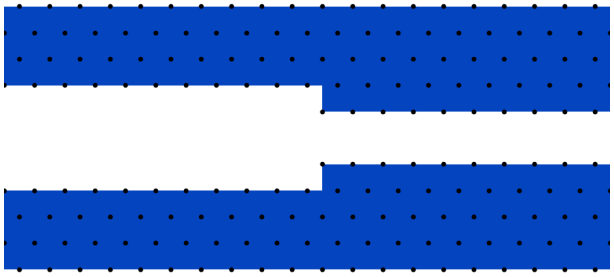

Figure 43: A constriction in a narrow flow channel. At most, three rows of vortices are commensurate with the wider channel, whereas a single row is commensurate with the inner channel. A sudden transition between these rows is expected near the aperture of the inner channel. The sudden constriction adds a potential barrier from left to right that must be overcome with sufficient driving and pressure from the queue of jammed vortices.

Stability can also break down when the driving force dominates over the sensitivity of the order of the flow patterns.

Previous work on constricted soft matter flow, for example the work of Zimmermann et al [125], has studied a hard-wall boundary flow. This leads to differences in response that can be attributed to: their confining potential not having commensurability effects from pinned edges that prevent simple flow, different interaction potentials, and a wider channel. Zimmermann et al use Brownian particles that interact via a power-law potential, $\sim 1/r^3$, in a channel wide-enough for approximately five rows, a row-drop is observed when the constriction is relatively small (approximately the row separation). They also report:

- Blockades in flow for large-enough constrictions.
- Smooth flow for weak interaction strengths.
- Oscillatory flow for higher interaction strengths.

The oscillatory flow is seen in measurements of particle flux through the constriction and

is reported to be stable or transient. We take note of this in our simulations because our observations indicate an unstable oscillatory flow which appears chaotic. Although our systems differ in construction, we still observe stable oscillatory flow over a large area of the parameter space.

Vasylenko et al [110], by contrast, examine the flow of Wigner crystals through a constriction with hard-wall boundaries. Their focus is on average flow rates of particles through the constriction, they present a velocity signal of particles in the constriction that appears chaotic (figure 3 of their paper). They correlate the signal with the number of particles in the constriction and focus on flow rates when the constriction width varies. They find that for thin constrictions, the rate of flow is suppressed. This is intuitive since particles are more likely to jam and interrupt the recombination of multiple rows. Their work is also experimentally accessible, with transport measurements reported in [93] that are reproducible in molecular dynamics simulations.

Further work [15] reports step-like electrical conductance dependence on interaction strengths, also observed in the previously discussed reports. This is due to the row drops forcing particles to slow down to accommodate less space in the constriction. More complicated funnel geometries also show step-like behaviour [68], jamming [81, 96], and ratcheting effects [27]. Funnel geometries are also accessible in superconducting Nb channels [53].

Periodic constrictions can exhibit reversible flow behaviour that is dependent on commensurability [121]. If a series of small constrictions are combined periodically, then the

number of flowing particles can be commensurate with the number of constriction points. The commensurability enhances hysteretic behaviour when driving particles in opposing directions. This work is also experimental and is constructed with a − NbGe and NbN layers - an ideal candidate for a realisation of our system.

A previous report, by Barrozo et al [20], on vortex motion in a wider (five or so rows) channel with a constriction reports a density profile that is similar to coarse-grained continuum flow. Our reported density profiles are similar to those reported in [88], which has a much stronger constriction that reduces multiple rows down to typically one or two.

The overlap between continuum and discrete flow exists somewhere between extremely thin constrictions and wider channels with weak constrictions. We endeavour to search for continuum phenomena in the thin constrictions that haven't been previously reported. In the references we consider, an aspect not reported in the discrete flow is turbulence, where the flow field becomes unstable and gives rise to chaotic effects.

Given that we are studying a row drop transition, we search for simple mechanisms that appear in [111, 112] and study the flow patterns. These simpler flows are usually exempt from chaotic effects and can be used to understand the original row drop transition.

In the remainder of this section, we fully describe the system geometry and the physical quantities we analyse. We then present results which categorise patterns and demonstrate the onset of chaos for certain choices of driving force and density. We also demonstrate

Figure 44: Illustration of the straight channel with length, $L = 100$. Periodic boundary conditions are applied such that the position of a vortex, $\mathbf{r_i}(x = 0, y) = \mathbf{r_i}(x = 100, y)$. The width of the channel at the constriction is $w = \sqrt{3}$ and in the un-constricted part is $w = 2\sqrt{3}$.

the stagnation of vortices near the constriction and calculate the profile of solitons in the constriction. We end this section with a discussion on experimental viability and improvements that can be made to the analysis.

9.1 The Geometry of a Constricted Channel

The most cited study with a constriction involves a brief change of background potential over a few lattice parameters [88]. This is enough to cause queuing and multiple row formation prior to entry of the constriction. With periodic boundary conditions, there is the possibility that a strong feedback mechanism exists between either side of the constriction. Although interesting in itself, we wish to avoid a structural feedback mechanism and limit the feedback to just the flux of vortices returning to the constriction, with no correlation to previous structure. Reducing the possibility that the constriction causes correlations in structure, the behaviour of vortices entering the channel is simplified and local effects which can be studied with low interference.

We study a channel with a long constriction, 50 lattice spacings long, that represents the very thin channel, with the non-constricted part being a wider, but still thin, channel (also 50 lattice spacings long). Vortices flowing in the constriction are single file and undergo Sine-Gordon flow. Figure 44 shows the straight channel that we study. We set the overall

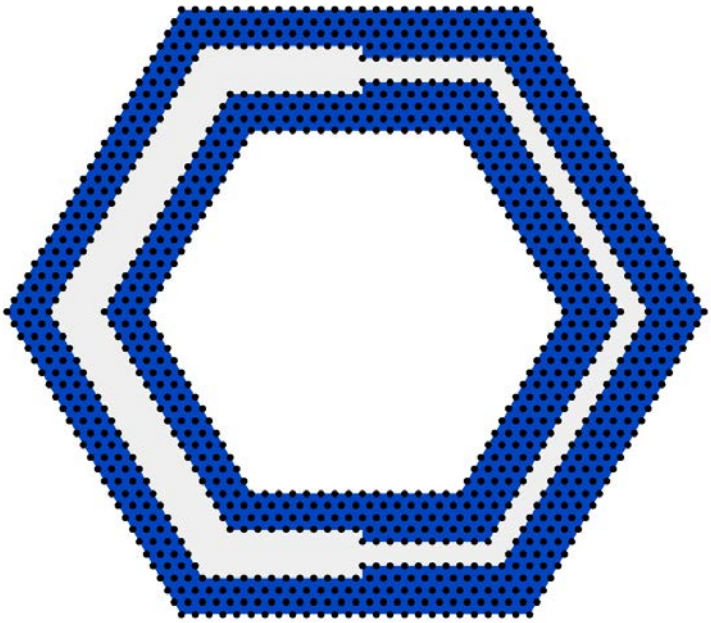

Figure 45: Illustration of the hexagonal channel for $L_0 = 20a_0$. The widths of the channel are designed to be the same as the straight channel; the constricted width is $w = \sqrt{3}$ and the un-constricted width is $2\sqrt{3}$. Vortices are driven in a clockwise direction in the results presented in this section.

length to be 100 lattice spacings long. Since we know that thin channels are dependent on density, we choose to change the number of vortices and keep length constant to keep the study limited to one straight geometry.

We also study a hexagonal geometry that removes the need for a periodic boundary condition, shown in fig. 45. If vortices flow in a ring, we raise the possibility of an experimentally realisable system that can passively maintain itself (without the need to actively remove and replace vortices at the end of a channel). A hexagonal channel lacks the vertical symmetry of the straight channel, so we expect results to differ between each case. Since the corners of the hexagon also play a role in the flow, we study different sizes of channel. Smaller channels have the edges closer to the constriction; we can discern which aspects of the flow are due to edges by studying small, medium, and large sized channels

equivalent to a straight channel of length 60, 120, and 180 lattice spacings long, respectively. We define a side-length, L_0, which is the length of one side of the hexagon drawn directly through the centre of the flow channel. Since we structure pins in a triangular lattice, we can construct the hexagonal flow channel to be commensurate with the pinned lattice. We consider a small ($L_0 = 10a_0$), medium ($L_0 = 20a_0$), and large ($L_0 = 30a_0$) flow channel for this thesis. More sizes can be simulated, but we find that three case studies are enough to show chaos and see the effects of the edges.

Applying a driving force in the hexagonal channel is no longer as straightforward as a global perpendicular current applied to the straight channel. Instead, a radial current is applied to the entire system, radiating from the centre of the hexagon. Considering the continuity equation for a point current source at the centre of a cylinder of radius, r, and thickness, D [34]:

$$\oint \mathbf{J} \cdot \mathrm{d}\mathbf{S} = -\mathbf{J}_{\mathrm{IN}} \tag{9.1}$$

$$2\pi r D\mathbf{J} = -\mathbf{J}_{\mathrm{IN}} \tag{9.2}$$

Since the thickness is constant, the current decays as $1/r$. The force applied to a vortex closer to the centre will be greater than one closer to the outer edge. The larger the hexagon is, the weaker this effect will be. The straight edges of the hexagon also mean that the force is only perpendicular at six parts of the channel.

To ensure results scale onto the straight channel, the force applied to a vortex at po-

sition $\mathbf{r_i}$ is:

$$\mathbf{F_{D,\mathrm{hex}}}(\mathbf{r_i}) = \hat{\mathbf{n}}_\mathbf{i} \frac{F_D L_0}{|\mathbf{r_i}|} \tag{9.3}$$

where $\hat{\mathbf{n}}_\mathbf{i}$ is the unit vector perpendicular to $\mathbf{r_i}$ in the anticlockwise direction.

$$\hat{\mathbf{n}}_\mathbf{i} = \begin{pmatrix} -\sin\left(\tan^{-1}\left(y_i, x_i\right)\right) \\ \cos\left(\tan^{-1}\left(y_i, x_i\right)\right) \end{pmatrix} \tag{9.4}$$

where $\tan^{-1}(y, x)$ is the quadrant preserving inverse tangent function [4]. The individual components of the vortex position are x_i and y_i. The inclusion of the L_0 term means that a numerical value of F_D in any simulation gives the same driving force at aperture entry and exit.

The contrasting effects of driving and channel symmetry mean we can search for differences and similarities in the straight and hexagonal channels. If we observe similar behaviour, chaotic or not, in both types of channel, then we have a more general result that should be applicable to other constricted systems.

9.1.1 Fabrication of the Hexagonal Channel

We consider a hexagonal channel because vortices can be driven around it periodically. Experimentally, this is realisable by attaching a conducting plate below the superconducting material to carry a radial current that drives the vortices. The periodic boundary

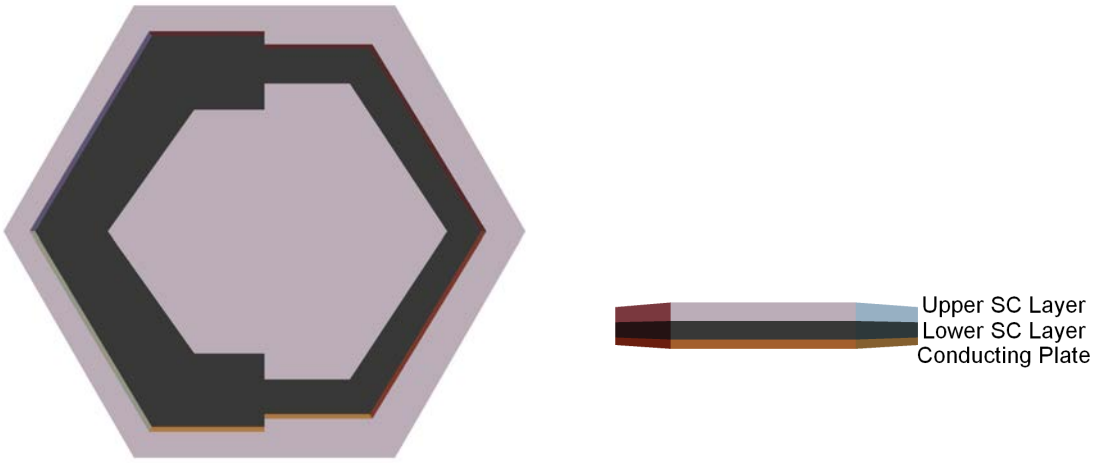

Figure 46: 3D rendering of the hexagonal channel. The left image shows the two layered superconductors and the constriction occupying half the channel. The right image shows the additional conducting plate on the base of the hexagon. A current is applied centrally and grounded at a number of points on the outer edges.

condition we apply to the straight channel makes realisation difficult since an active mechanism of replacing vortices that leaves the channel must be developed. Vortices in the hexagonal channel loop around, simplifying the issue of the periodic boundary condition. Figure 46 shows an example of how this can be achieved.

9.2 Simulation Procedures

The parameter space of these systems is limited by the maximum number of vortices that can be placed inside without any escaping the confining lattice. If too many are present, or the driving force is too high, then vortices will be forced out of the system. The simulation software performs frequent checks to ensure all vortices are in the active parts of the channel; if a vortex leaves the channel, then the software terminates and a log of system failures is made. We limit this to $\mathbf{F}_{\mathbf{D},\max} = 0.8$; all results presented have complete confinement of all vortices. This way, we can be sure that any chaotic signatures

are due to the dynamics, not a system failure.

Simulations are initiated by randomly placing vortices in the channel and allowing them to relax. Driving force is incremented by 0.01 every 10^5 time steps until vortices escape the channel or $F_D = 1.0$. We generally coarse grain any position data we choose to output. Outputting $2 \times N_v \times 10^7$ double-precision coordinates would result in a file size of the order of ten Gigabytes per run. Data can be coarse grained for animation purposes, but analysis is done on-the-fly during simulation, with processed data outputted in much smaller files.

First and fourth order integration routines are implemented with no qualitative difference observed initially. The data for the straight channel is presented from fourth order routines; all hexagonal channel results are from first order routines. The range of parameters is limited by escaping vortices at high drives and uneventful data at low drives. For all channels, we simulate the same range of driving forces: $0.20 \leq F_D \leq 0.80$. The lowest drive is just higher than the depinning force required to cause collective motion of vortices and the highest drive is just below that which causes vortices to escape the channel easily. Checks are in place during simulations to ensure no vortices escape the channel. All data presented is for complete containment of vortices. For the straight channel, we simulate vortex numbers: $90 \leq N_v \leq 110$. For the hexagonal channels, we simulate: $55 \leq N_v \leq 70$, $120 \leq N_v \leq 140$, and $190 \leq N_v \leq 210$ for $L_0 = 10$, $L_0 = 20$, and $L_0 = 30$ respectively.

9.3 Chaotic Signatures from Time-Series Data

For systems with many degrees of freedom, calculating coefficients of chaos is computationally and philosophically difficult. Elementary methods typically use simple maps or differential equations with a low number of degrees of freedom which means that the phase space needed to analyse the system is typically low-dimensional and easy to construct. Conversely, when a complex system of many degrees of freedom, such as this one, is considered, there is no clear mapping or low dimensional differential equation that can generate a chaotic set of data.

With time-series data without a simple generator, numerical techniques are used to reconstruct phase space portraits and associated quantities instead. In this section we describe the time-series we generate and the algorithms used to analyse it. We use two quantifiers of chaos to ensure our results are consistent: Fractal dimension and Lyapunov exponents.

9.3.1 Choice of Time-Series Quantity

In order to analyse chaotic behaviour, a time-series is needed. We find the average amplitude of vortices is an effective quantity that we can sample every time-step:

$$A(t) = \frac{1}{N_v} \sum_{i=1}^{N_v} |y_i(t)|, \tag{9.5}$$

where y is the distance away from the central line running through the channel. In the straight channel, this is the distance away from the line $y = 0$. In the hexagonal channels, the closest distance to the imaginary centre line running through the channel which forms a regular hexagon is used. This quantity is continuous and provides a clear picture of

when chaos emerges. Figure 47 shows some amplitude data from simulations for reference.

The attractor is reconstructed from the time-series data. This is done by calculating the vector, $(A(t), A(t+\tau), A(t+2\tau), \cdots, A(t+(N-1)\tau))$ [102, §9.7]. This $N-$dimensional vector will trace out the phase space portrait of the system when time is evolved. The delay time, τ, must be carefully chosen in consideration with the data. If the delay time is too low, the attractor will constrict and resemble a line because each point on the attractor will have similar $(x, y, z, \cdots)$ values. We find using the average time between vortices entering the constriction to work well as a period since it scales well with driving force and the time increment in the simulation. We have modified our delay times by up to factors of 4 and have seen little difference in speculative results. Figure 47 shows attractors next to their respective amplitude data for some simulation results.

'Whiteney's Embedding Theorem' [115] tells us how many dimensions are needed to embed an attractor. In order to avoid any overlaps of phase space trajectories (uniqueness), the attractor must be embedded in a dimension of $2N + 1$, where N is the dimension. Technically, the number of degrees of freedom is at least twice the number of vortices in the channel due to each having two degrees of spatial freedom, which would mean uncomputably large embedding dimensions to guarantee no overlaps. We find that we can recover signals well in as few as 3 dimensions, although there is some associated noise. Analysing in higher dimensions will take significantly longer, with no guarantee of higher quality results.

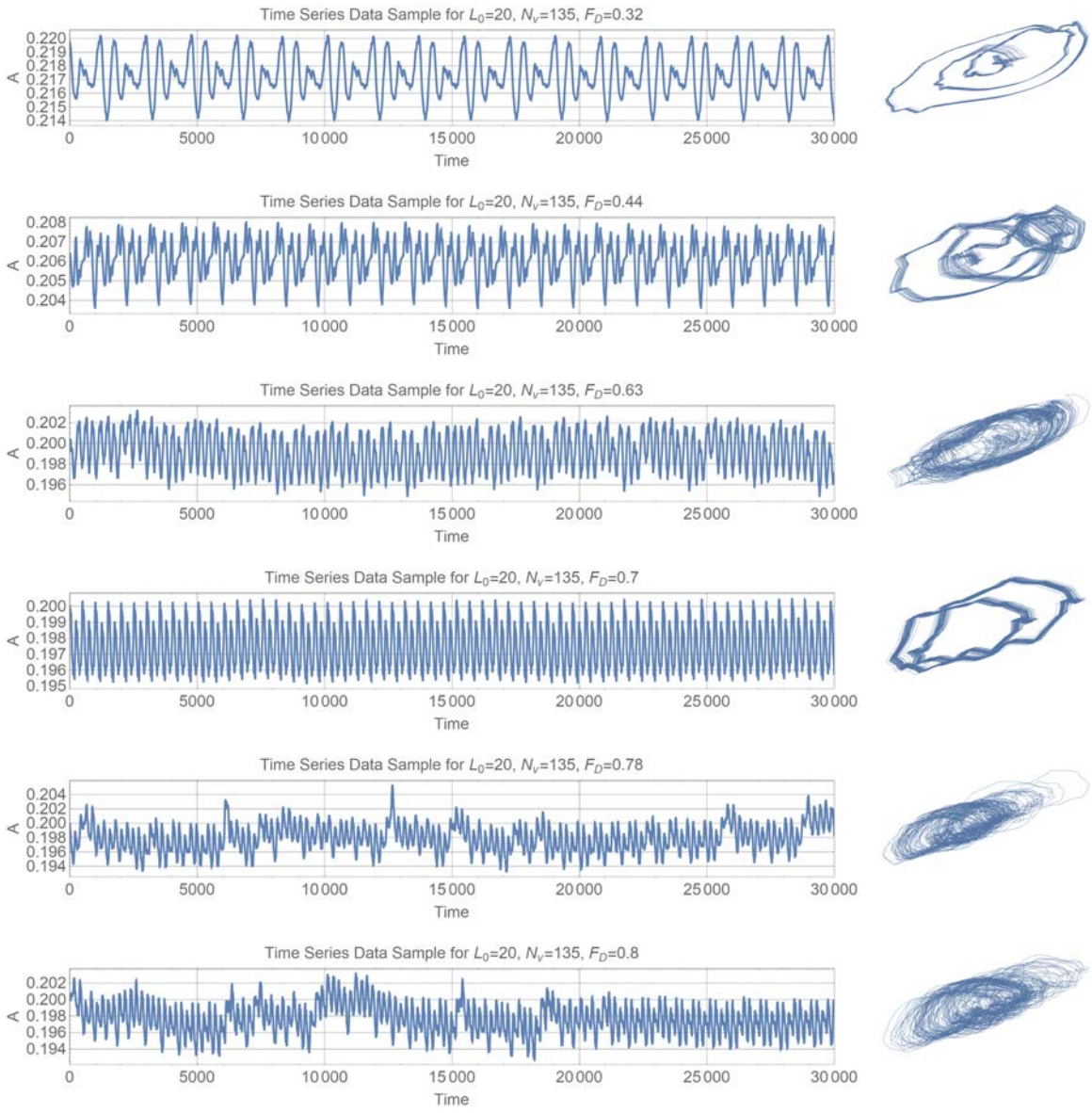

Figure 47: Some examples of amplitude data and the reconstructed attractors projected in two dimensions. The widths of nearby trajectories on attractors that appear non-chaotic are due to low-frequency feedback loops caused by the periodic nature of the channel.

9.3.2 Box Counting (Fractal) Dimension

There are several types of fractal dimension that can be used to show an attractor is fractal, and hence the system chaotic [102]. We calculate the box counting dimension; an indicator of fractal structure which considers the structure of a set of points on many length scales.

In order to find fractal structures in a finite set of Euclidean points, a series of boxes are mapped onto the phase space portrait. These boxes divide the system into sub-spaces which may or may not have members of the set in. As the division increases, the ratio of the logarithms of the number of boxes with points present, $N(s)$ and the logarithm of $1/s$, where s is the box length, is recorded. The fractal dimension of the set is given by [102, §12.2]:

$$D = \lim_{s \to 0} \frac{\log\left(N(s)\right)}{\log\left(1/s\right)} \tag{9.6}$$

Since our data set is finite, this ratio will plateau at a certain scale. A gradient of $\log\left(N(s)\right)$ versus $\log\left(1/s\right)$ is taken before this point to determine the fractal dimension of the attractor. For example, a set of points that draw out a square structure in 2D should have a dimension of 1 since it is a set of straight lines. If we construct such a square out of 100 evenly spaced points, and plot points, we see the line plateau in fig. 48 once the scale goes beyond the resolution of our data.

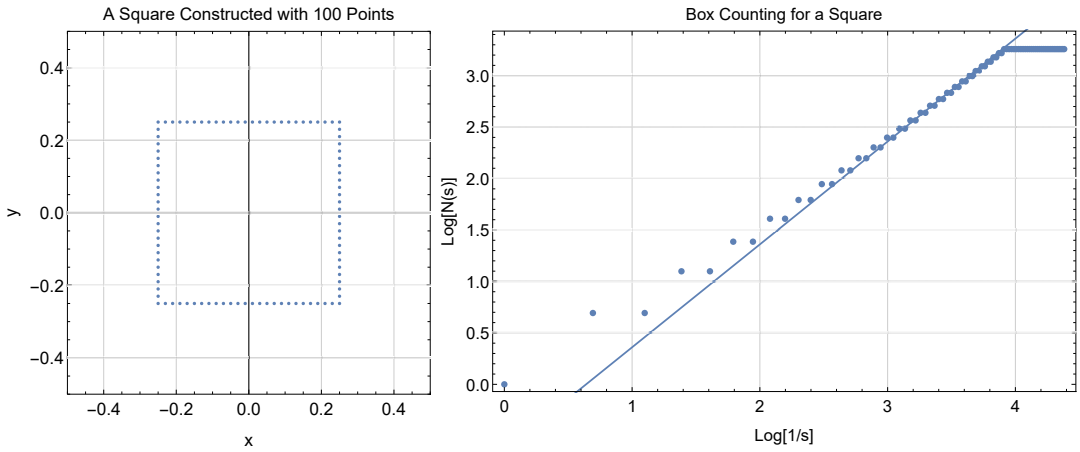

Figure 48: Box counting for a set of points on the edge of a square. The gradient of the plotted line approaches the correct dimension of 1 but plateaus before this due to the finite set of data. The plotted line has gradient 1 to demonstrate the tendency towards it.

Our data sets are considerably more populous than this example set, although we still ensure that the scale doesn't go far beyond the resolution of the points.

Searching for points in each box is computationally intense once the scale gets to fine resolutions, but is easily parallelisable since a single thread can search in a different box concurrently with any other.

9.3.3 Lyapunov Exponents

The Lyapunov Exponent is a measure of the divergence of the evolution of two infinitesimally separated points on an attractor. If the separation of the points is $\sim e^{\Lambda t}$, then Λ is the Lyapunov Exponent. If $\Lambda < 0$, then two nearby points will tend towards each other as time evolves and the system tends towards stability (no chaos). If $\Lambda = 0$ then the points always remain at the same separation and no chaos is present [47, §2.1]. If $\Lambda > 0$, then the two points diverge, which is the definition of chaos. Since we have data that we are

unable to naturally model with equations of motion, we "have a much harder task" [102, p. 253] to find the Lyapunov exponent than if we had a simpler set of equations. We apply a well established method that can approximately calculate the Lyapunov exponent [117].

Systems typically have a spectrum of Lyapunov Exponents, $\{\Lambda_1, \Lambda_2, \cdots, \Lambda_n\}$ [117]. If any one of these exponents are positive, the system is chaotic; chaos is determined by the largest exponent. Since only the largest exponent is needed to determine chaos, we employ a method that approximates the largest exponent.

We implement the method which approximates the largest Lyapunov Exponent of the system by examining nearby trajectories in phase space [117]. Since the number of degrees of freedom is so high, it is difficult to perturb the system without guaranteeing the particular vortex is close to an unstable part of the trajectory.

Provided enough amplitude data is recorded, a phase space portrait can be generated that should have nearby trajectories at different times. If two are sufficiently close enough, then we can look at the divergence (or convergence) of the two paths to determine Λ. This should be done on a small scale since the exponent is defined for infinitesimally small differences.

Following the method presented in [117], one follows a trajectory in phase space, locates the closest neighbouring trajectory that is temporally separated by at least a full cycle, and records the separation, $|\delta s|$, of the two paths over a few increments. Before

the separation gets too large, a new closest trajectory should be found and the process continued. A best fit is found of $\log(t)$ against $|\delta s|$ which is assumed linear; the gradient of the separation is the Lyapunov exponent at that point [102, §10.4]. A long-time average of these is taken and the Lyapunov Exponent is derived.

There are other methods to calculate Λ. They generally require a large data set to ensure trajectories have close enough neighbours which is cumbersome for frequent lookups and comparisons. Our calculations keep 20000 points on the attractor and a single exponent calculation takes approximately ten minutes with our script. To increase the embedding dimension or include more points is a matter for further research since the time constraint requires further optimisation.

9.4 Flow Patterns

We require a method to extract non-temporal information from the data to indicate how vortices are flowing. This is useful because we can cross-reference flow patterns with Lyapunov exponent and fractal dimension data to confirm chaotic behaviour and discuss its nature.

We record the order of which vortices enter the constriction, cross-referenced with their height at $x = 24.5$ for the straight channel and $x = -0.5$ for the hexagonal channels. This shows clear patterns of ordered entry. When the patterns break down or start to compete with one-another, we can compare with Lyapunov exponent and fractal dimension data

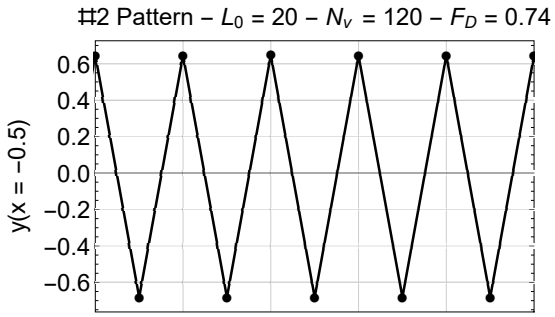

Figure 49: The 2 state can be thought of as an inverse zig-zag transition. The horizontal axis is arbitrary; all points are equally separated to show the *order* of vortices flowing into the constriction.

to find out if chaos is present.

We also show the trace of vortices over a simulation run which, in coordination with the flow-pattern data, gives a detailed indication of the trajectories of individual vortices on separate chains. Figure 50 shows an example of a trace for a zig-zag state transitioning down to a single chain at the aperture of constriction.

9.5 Categorisation of Flow Patterns

We observe a number of different flow patterns, including chaotic ones, all categorised in this section. All figures depicting the patterns show the sequential order of vortices on the $x-$axis plotted against their previous position one unit away from the aperture of constriction.

9.5.1 2−Cycles

A single type of 2−cycle is possible which is a repeated up/down pattern of vortices from two chains merging into one alternatively. Figure 49 show the sequential positioning of

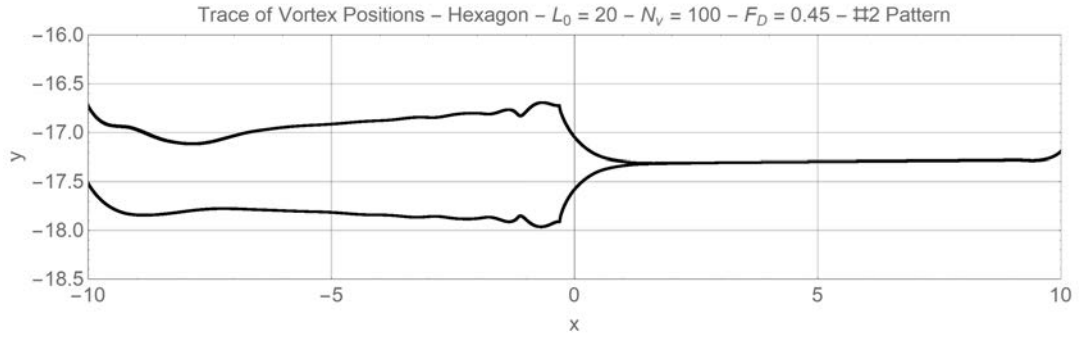

Figure 50: Example of the trace of vortex trajectories for two chains of flowing vortices merging into one. The asymmetry is due to the corner of the hexagon; vortex paths curve around towards the straight edge leading to the constriction.

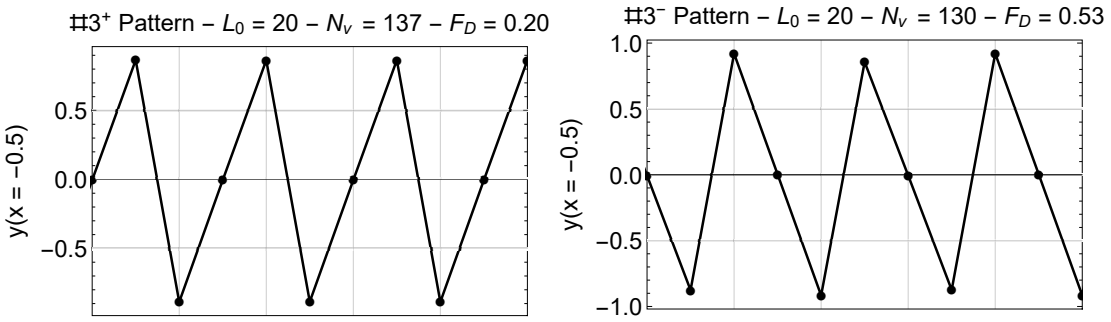

Figure 51: The $3^{\pm}$ states indicate a flow pattern where the top and bottom rows merge, followed by a vortex from the middle row. If the top vortex enters the aperture of constriction first, then the state is considered positive, otherwise it is considered negative. The horizontal axes are arbitrary; all points are equally separated to show the *order* of vortices flowing into the constriction.

vortices one lattice parameter before they enter the channel. Figure 50 shows the trace of this type of pattern.

9.5.2 3−Cycles

All 3−cycles are vertical symmetry broken and are observed in two possibilities. In the hexagonal channels, the broken vertical symmetry causes one of the possibilities to be more favourable than the other. In the straight channel, both possibilities are possible and are observed equally as often in repeated runs or in nearby regions of the phase di-

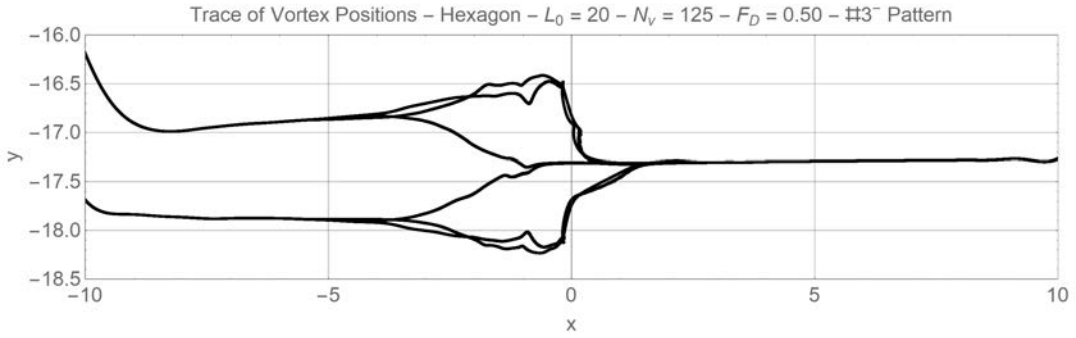

Figure 52: Trace of trajectories for the 3^- pattern. Vortices alternate in a top-centre-bottom pattern. The asymmetry of the pattern is clear in the trace. The 3^+ pattern is a reflection of this trace through the central axis.

agram. Typically, once the symmetry is broken, the pattern will remain in that broken phase until a transition to another $n-$cycle occurs.

9.5.3 $4-$Cycles

We observe several different patterns that repeat every 4 cycles. Their naming includes subscripts to differentiate them, usually indicating an alphabetical letter that the pattern resembles.

The 4_S state is the merging of top, bottom, top-centre, and bottom-centre rows of vortices in a straightforward pattern. The centre row is bifurcated and the top rows move single-file. The 4_S^- pattern is a symmetry broken version where the bottom-centre row becomes a top-bottom row.

The 4_W^- state is the merging of top-top, bottom-top, top-bottom, and bottom-bottom rows in a straightforward patter. The top and bottom rows are both bifurcated, and the

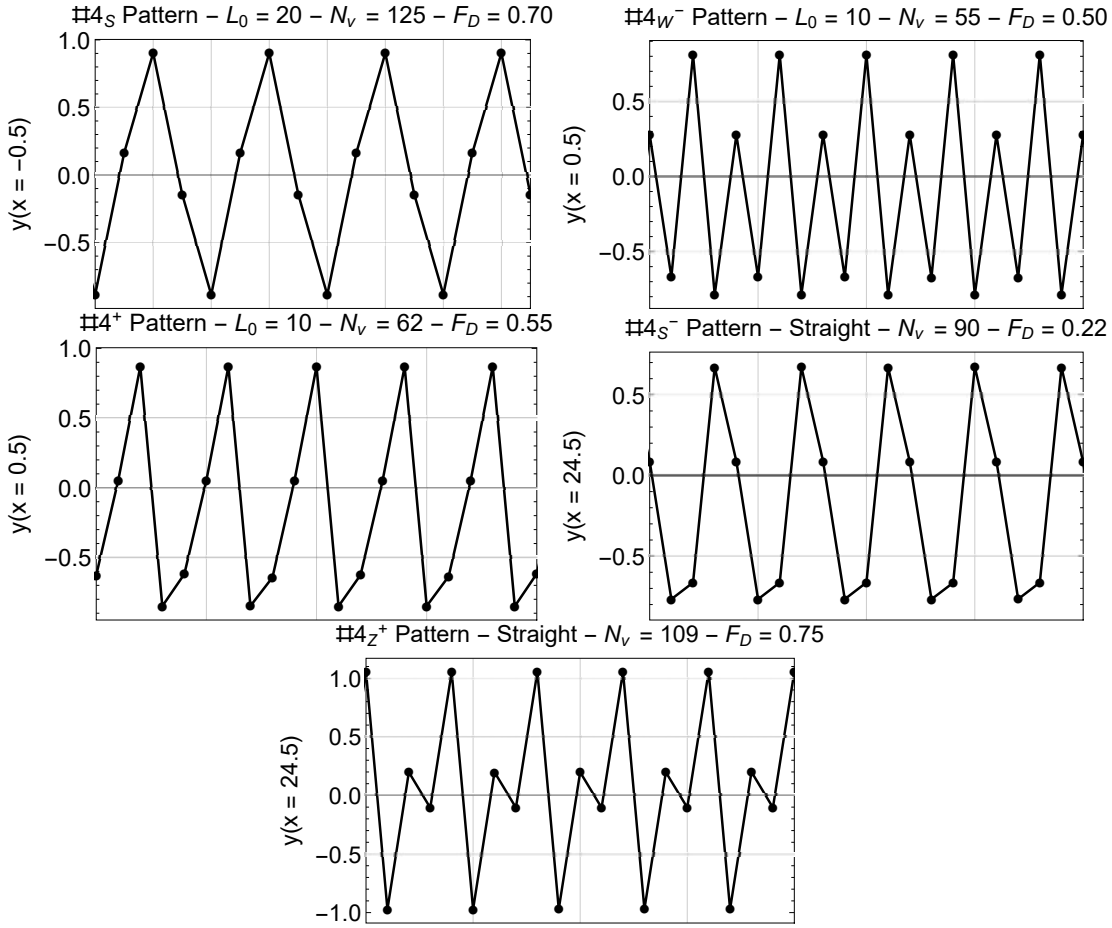

Figure 53: Examples of 4−cycle patterns. The subscript, S, indicates the pattern follows an approximate sinusoid; W, indicates the pattern resembles the letter W; and Z, indicates the pattern resembles a distorted letter Z. The non-subscripted state resembles a sawtooth function. The horizontal axes are arbitrary; all points are equally separated to show the *order* of vortices flowing into the constriction.

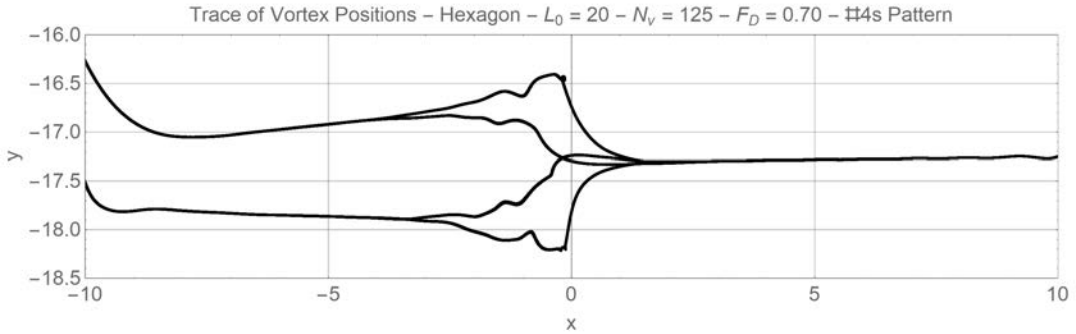

Figure 54: Trace of the trajectories for the 4_S pattern. This flow pattern is symmetric and there are four distinct flow lines that can be cross-referenced to the pattern in section 9.5.3.

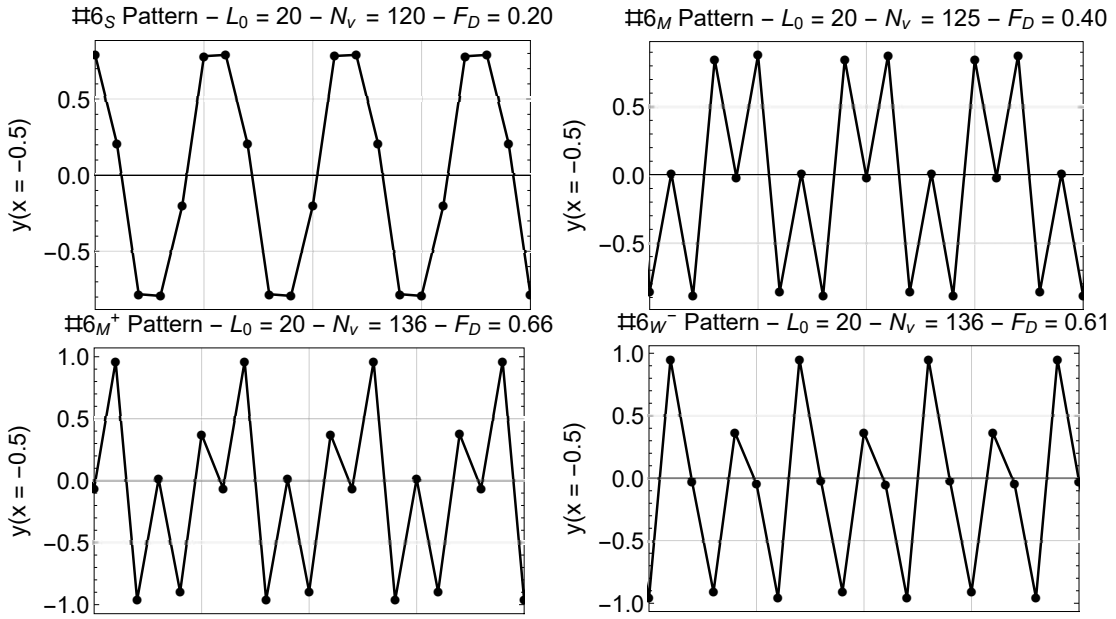

Figure 55: Examples of 6−cycle patterns. The subscript, S, indicates the pattern follows an approximate sinusoid; M, indicates the pattern follows alternating M and W patterns; and W, indicated the pattern resembles the letter W. The horizontal axes are arbitrary; all points are equally separated to show the *order* of vortices flowing into the constriction.

top rows are more separated than the bottom rows.

The 4^+ pattern is similar to the 4_W^- state in that one can consider the row separation of the top rows to be so great that the bottom-top row appears almost central. The ordering changes to a lowest-to-highest order.

The 4_Z^+ pattern has the same row structure are the 4_S pattern, but with a different ordering.

9.5.4 6−Cycles

The 6_M pattern is commonly observed. Its symmetry holds well, even in the hexagonal channels. We observe a symmetry broken variation of it that we denote 6_M^+ due to a rough

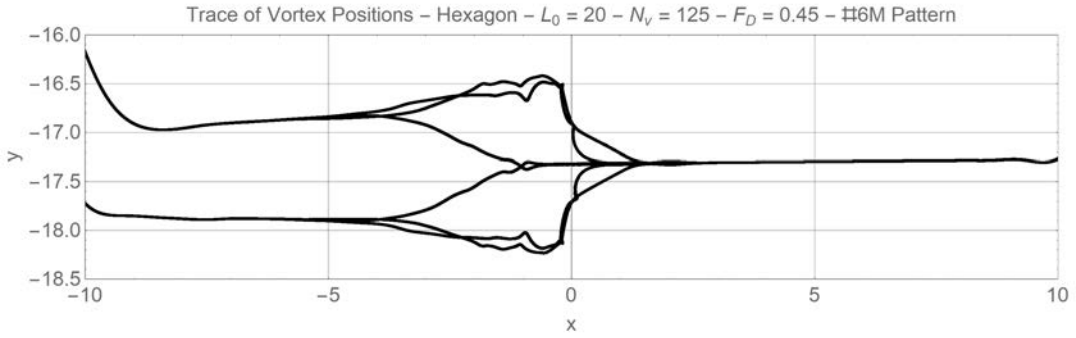

Figure 56: Trace of the trajectories for a 6_M pattern. This pattern appears to be a superposition of a 3^- and a 3^+ pattern which restores the symmetry that the individual competences break.

positive gradient one could fit the points in a cycle to. We only observe the 6_M^+ state in the hexagonal channels and don't observe the 6_M^- counter-part.

The 6_W^- state is another symmetry broken state only observed in the hexagonal channels. Again, we don't observe the 6_W^+ state. We predict that if the driving force direction was flipped, then the unobserved flow patterns should be observed instead.

The 6_S pattern is symmetric and observed in the straight and hexagonal channels.

9.5.5 12−Cycle

A single 12−cycle is observed which is a alternating combination of the 6_W^+ and 6_W^- patterns. This state is rarely observed (2 points exist on the $L_0 = 20$ phase diagram) and is surrounded by chaotic regions. To maintain such a complicated pattern is energetically difficult; most of the chaotic patterns observed nearby this state is a fluctuating version of the 12 state.

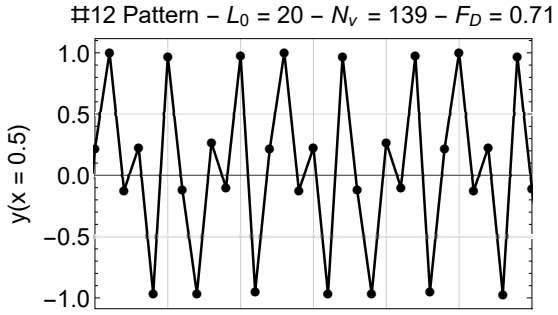

Figure 57: The 12−cycle is the most complex pattern (aside from chaotic) we observe. The horizontal axis is arbitrary; all points are equally separated to show the *order* of vortices flowing into the constriction.

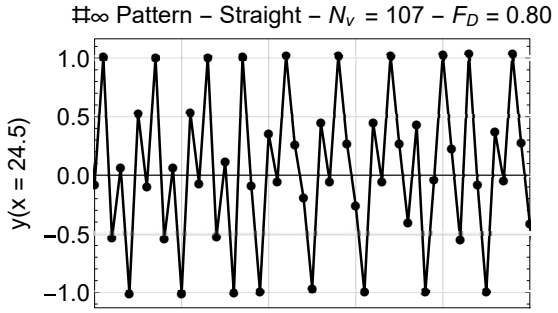

Figure 58: The chaotic patterns have a high variance in their form depending on which part of the phase diagram is it taken from. The horizontal axis is arbitrary; all points are equally separated to show the *order* of vortices flowing into the constriction.

9.5.6 ∞−Cycles (Chaos)

When a repeated pattern is unidentifiable, it is chaotic. We can quantify the chaos by calculating the fractal dimension of the attractor generated by plotting the set of points $(y_i, y_{i+\tau})$ where τ can be any integer. We find the delay time makes little difference for this data as the dimension found for the ordered states is always very close to zero and the chaotic states is significantly higher than zero, which makes identification of chaos straightforward.

Previously, we discussed two reasons why chaos occurs. The straight channel is more prone than the others to chaotic behaviour near to transition lines due to competition

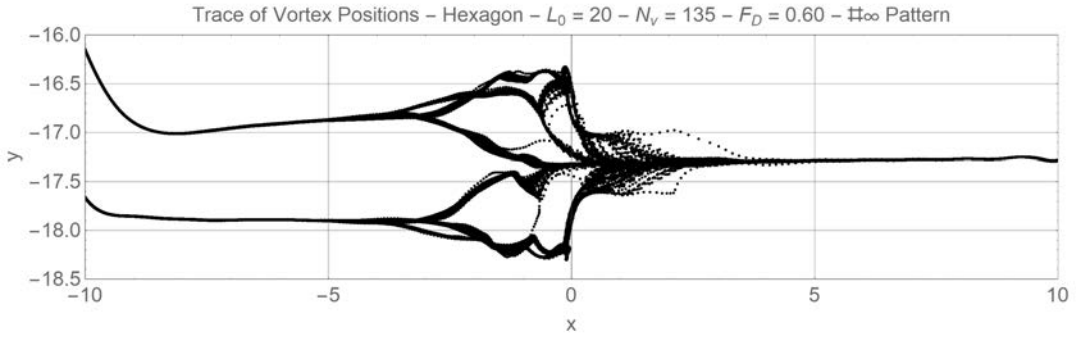

Figure 59: Trace of trajectories for a chaotic flow. Although there are some dominant flow paths, vortices often lose their tracking which causes a chaotic signature.

between two states. This is due to the energetic competition between each state and the ability to access both given the fluctuations associated with multiple rows splitting and recombining. This isn't easily seen in the box-counting dimension since we may only add a few extra points to the attractor which won't cause much difference.

In the straight channel, there are regions where the broken symmetry flow pattern is degenerate. We typically observe a single flow for a long time which can occasionally change to the other equivalent pattern. Because this happens so rarely, the attractor is strongly zero-dimensional and chaos is not measurable with our technique.

9.6 Phase Diagrams for Flow Patterns

We inspect each flow pattern by eye and derive the phase diagram for flow patterns on a discrete grid. They are presented next to the phase diagrams for fractal dimension and Lyapunov exponents in order to highlight the similarities for each geometry.

9.6.1 Fractal Dimension Phase Diagrams for Flow Patterns

We generate phase diagrams for the fractal dimensions of the attractor generated by plotting the set of points (y_i, y_{i+1}), where y is the distance away a vortex is from the centre of the channel one lattice spacing before the aperture. This generates a low-dimension Poincaré section from which the fractal dimension can be efficiently calculated. There are several orders of magnitude needed to see the structure easily, so we present multiple zooms for each diagram.

These diagrams show similar structures to the flow pattern portraits. The regions of non-zero fractal dimension suggest different flow patterns have a certain fractal dimension associated with them. The regions where we clearly identify chaos by eye have significantly higher fractal dimensions. The similarities between the fractal dimension diagrams and phase patterns means we can be confident that there is chaos present for certain values of drive and density.

9.6.2 Lyapunov Exponents

We can further confirm the onset of chaos by calculating the Lyapunov exponent for the amplitude data as previously discussed. There are some drawbacks with the method we implement: the method assumes the largest exponent is positive and the phase space trajectories are not separated by a infinitesimal distance. Despite this, we still recover chaotic signals that map on to the fractal dimension and pattern plots adding credence to the chaotic nature of some of the flow.

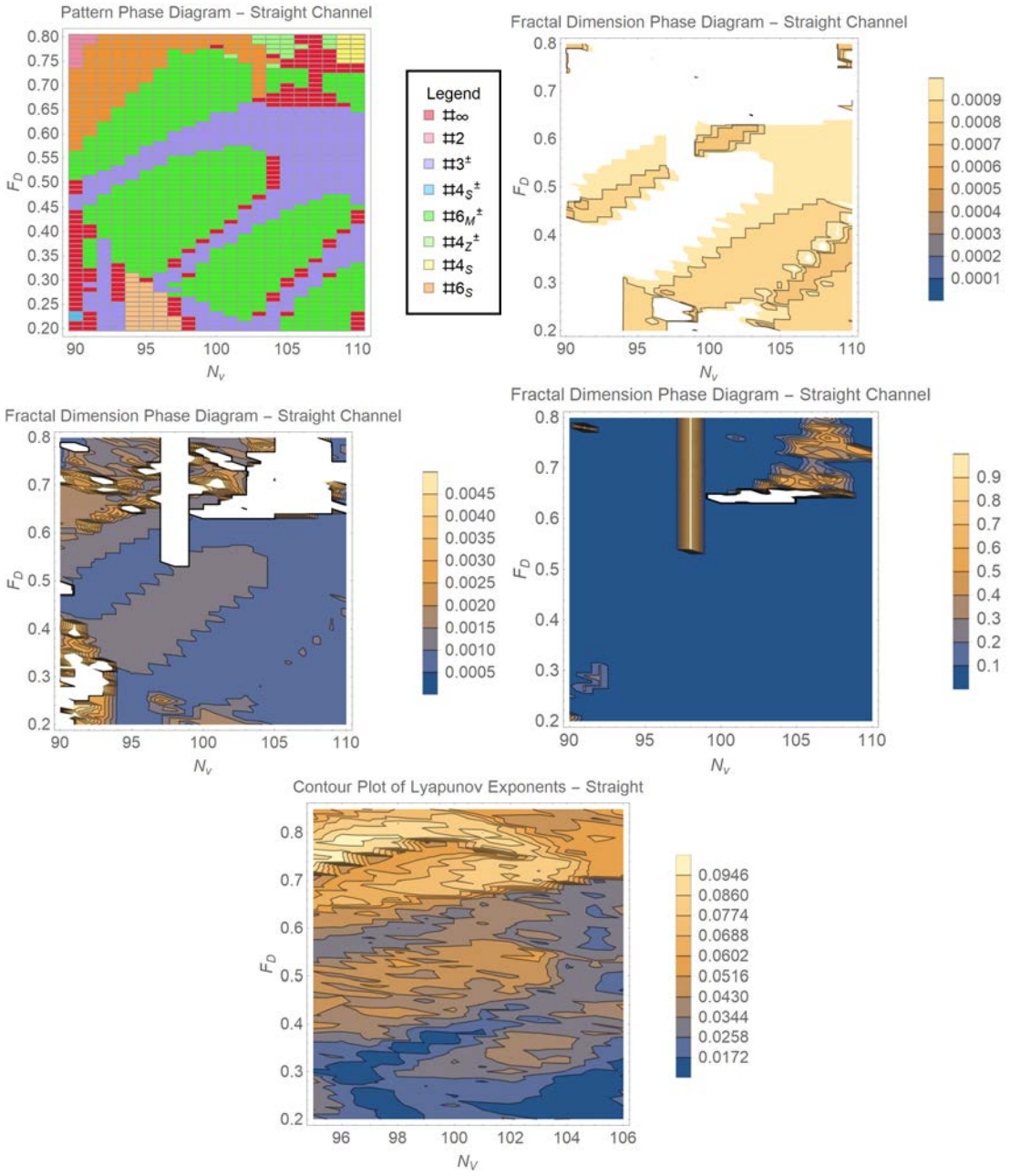

Figure 60: Phase diagrams for the straight channel. The straight channel is more prone to chaos than other channel geometries because of the additional competition of degenerate symmetry-broken states near transitions.

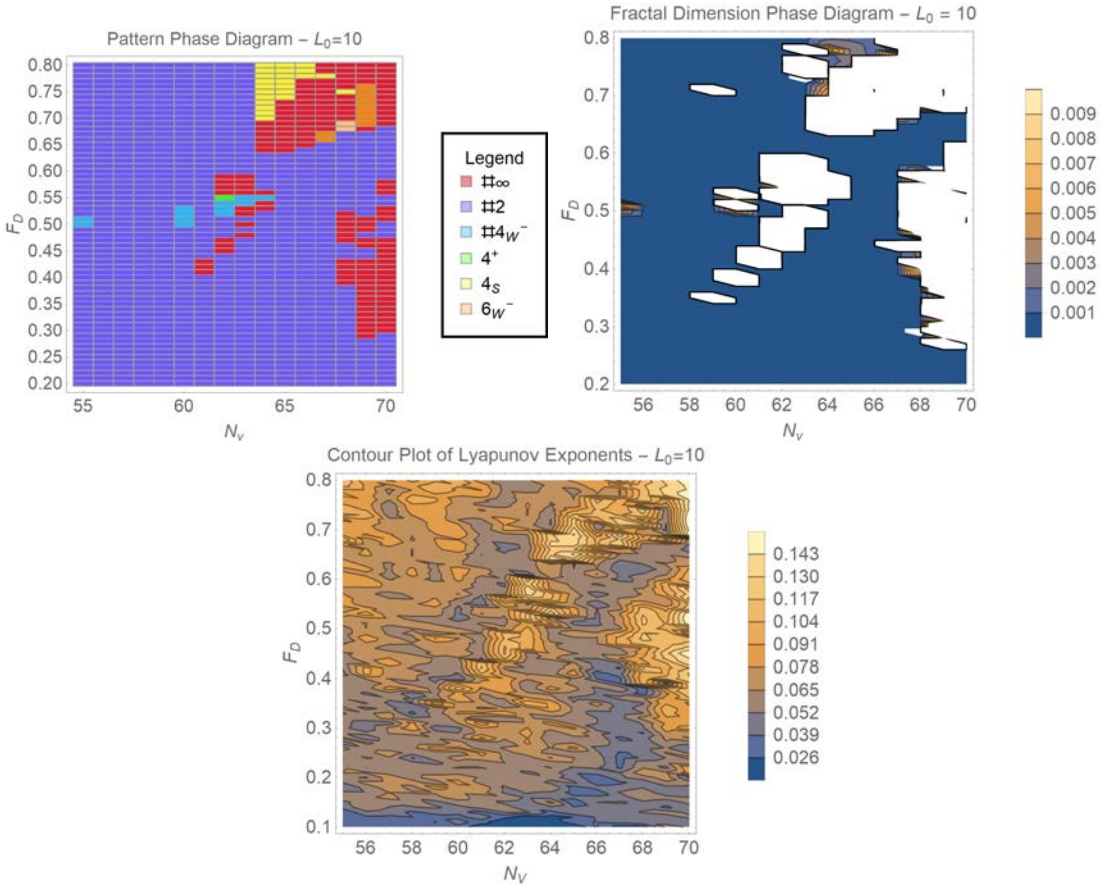

Figure 61: Fractal dimensions for the hexagonal channel with $L_0 = 10$. This case shows the smallest range of states and is either dominated by the #2 state or chaos.

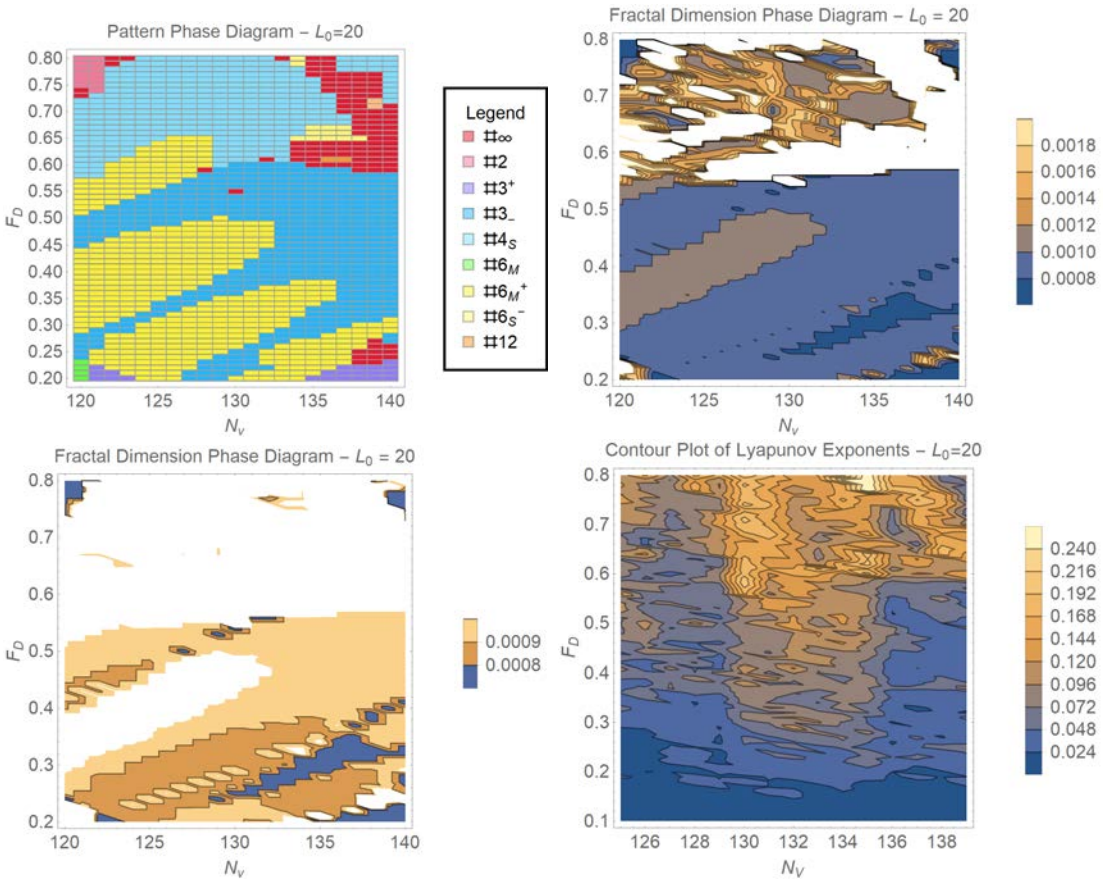

Figure 62: Phase diagrams for the hexagonal channel with $L_0 = 20$. This geometry and the straight channel have very similar features of peninsula-like structures of certain states in a "sea" of 3-cycle patterns.

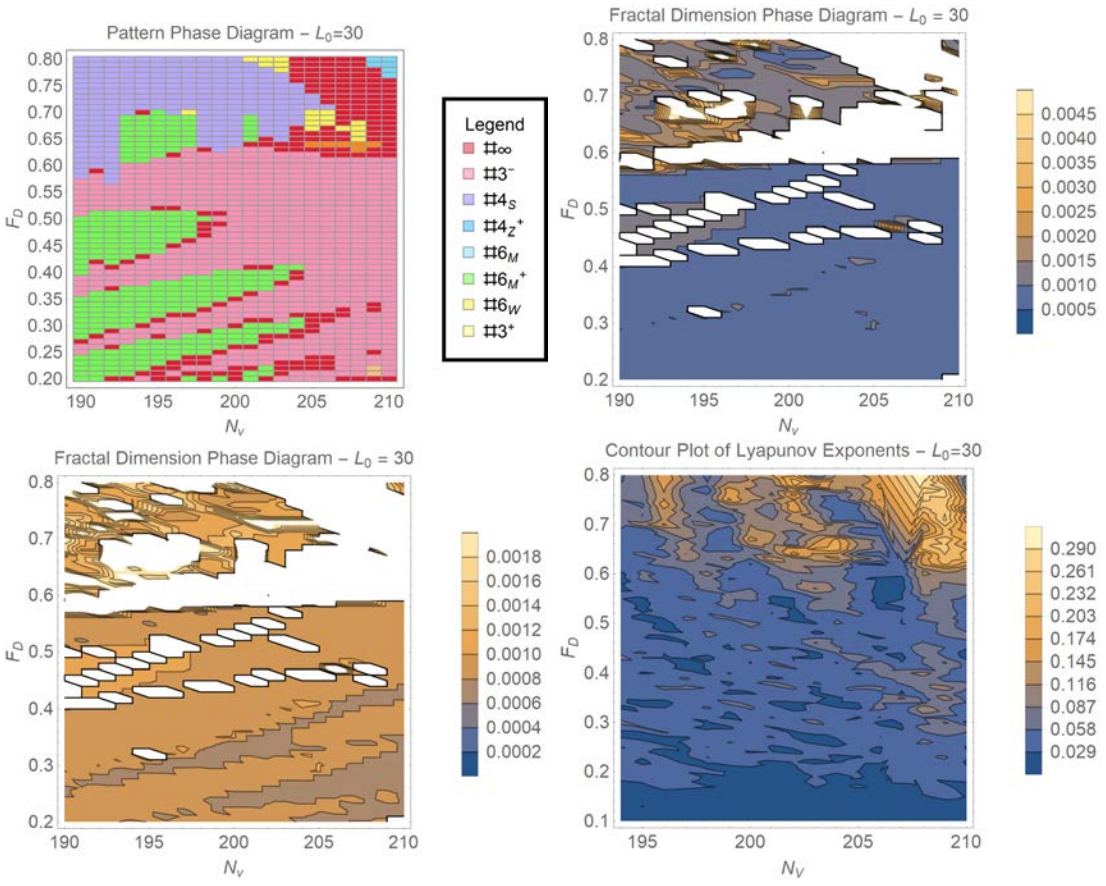

Figure 63: Phase diagrams for the hexagonal channel with $L_0 = 30$. The peninsula-like structures are, again, present, which similar features appearing across all three types of phase diagram.

The smallest channel has an additional level of complexity in the analysis due to a significant amount of noise in the amplitude data. This is primarily caused by the proximity of the aperture of constriction and the corners of the hexagon which leads to large interactions of corner vortices nearby. The asymmetry of the corners further complicates the issue.

We find that a low-pass filter, with a cut-off of 0.1 in the relative units of our data is an effective way to clean the data without removing any chaotic frequencies that are typically at least an order of magnitude lower. Since the chaos manifests on the scale of several maxima, these low frequency signatures will remain unchanged by the filter.

Despite the removal of noise, the channel is the most chaotic of the ones chosen for this study due to the strongest interactions with corners and the shortest feedback time of a vortex cycling around the channel.

9.7 Repeatability of Results

Due to the large time requirements of calculating Lyapunov exponents, we will calculate the error bars in the Lyapunov exponents for one particular system over a range of driving forces. we choose the $L_0 = 20$ hexagon for $N_v = 135$ and present a plot of the mean Lyapunov exponent with error bars spanning one standard deviation of the data in fig. 64.

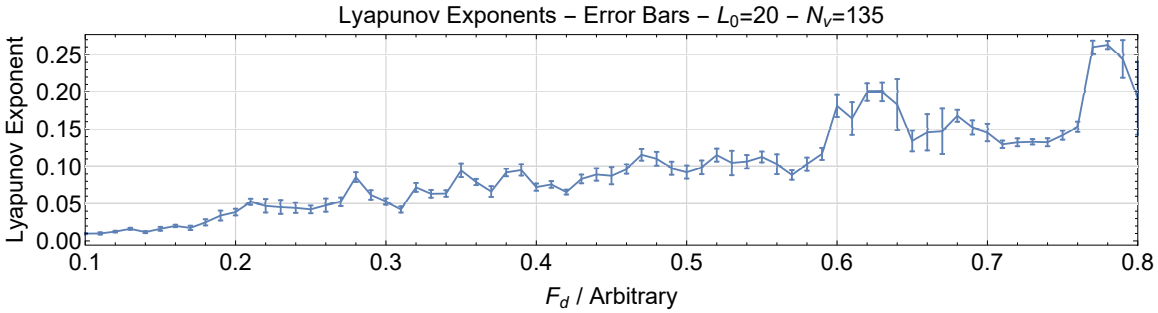

Figure 64: Errors in Lyapunov exponent measurements for ten separate simulations with randomised initial conditions.

9.8 Observation of Stagnation near the Constriction

Another effect of chaos and turbulence is stagnation. In a continuous flowing system, a stagnation point is where there is zero flow field, typically encircled by a 'vortex' of fluid. We put quotation marks on 'vortex' currents to distinguish them from the flux vortex. For instance, the continuum flow shown in fig. 5 shows stagnation near the ends of the constriction where there is a point where the fluid velocity is zero. Other studies that report stagnation in chaotic systems include eccentric journal bearing studies [51] or more generally in two eccentric cylinders rotating to cause a shear flow [16]. In the discrete system, a stagnation point can be a single vortex that doesn't flow, an example of this is shown in fig. 65.

Occasionally, we observe a single vortex tracing out a loop, as shown in fig. 66, which we consider to be a temporary stagnation of a particular vortex. This effect can occur asymmetrically in the straight channel, where a symmetry breaking mechanism causes a bias in flow and looping vortices are observed in either just the upper or lower parts of the channel.

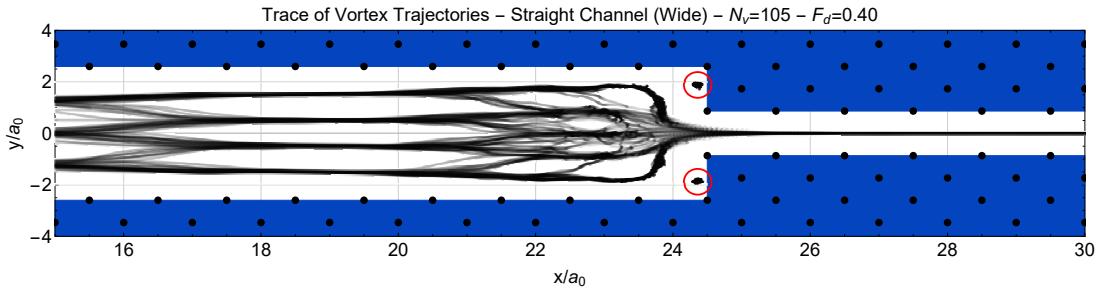

Figure 65: Trace of a simulation of a wide constricted channel where two vortices permanently stagnate (shown circled in red).

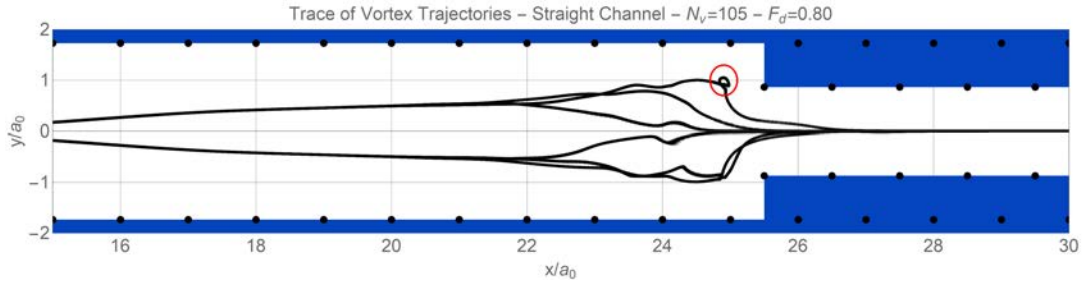

Figure 66: Trace of a simulation of the narrow constricted channel where vortices in the top row loop around before entering the aperture of constriction (shown circled in red).

In order to cause a vortex to permanently stagnate, we study a wider version of the flow channel where the constricted part is the usual width, but the un-constricted part is an additional two pinned rows wider. This additional width, depending on the configuration of the pinning array, has indentations that can trap a vortex which acts like the missing pin and allows other vortices to smoothly flow past it.

9.9 A Note on Soliton Flow

As discussed in section 4, we expect solitons to form in the narrow part of the constriction. A non-linear density gradient forms along the length of the entire channel, peaking when vortices jam at the aperture, reaching a minimum as vortices leave the constriction. Since the standard soliton calculations assume a constant density [23], we expect our results to differ.

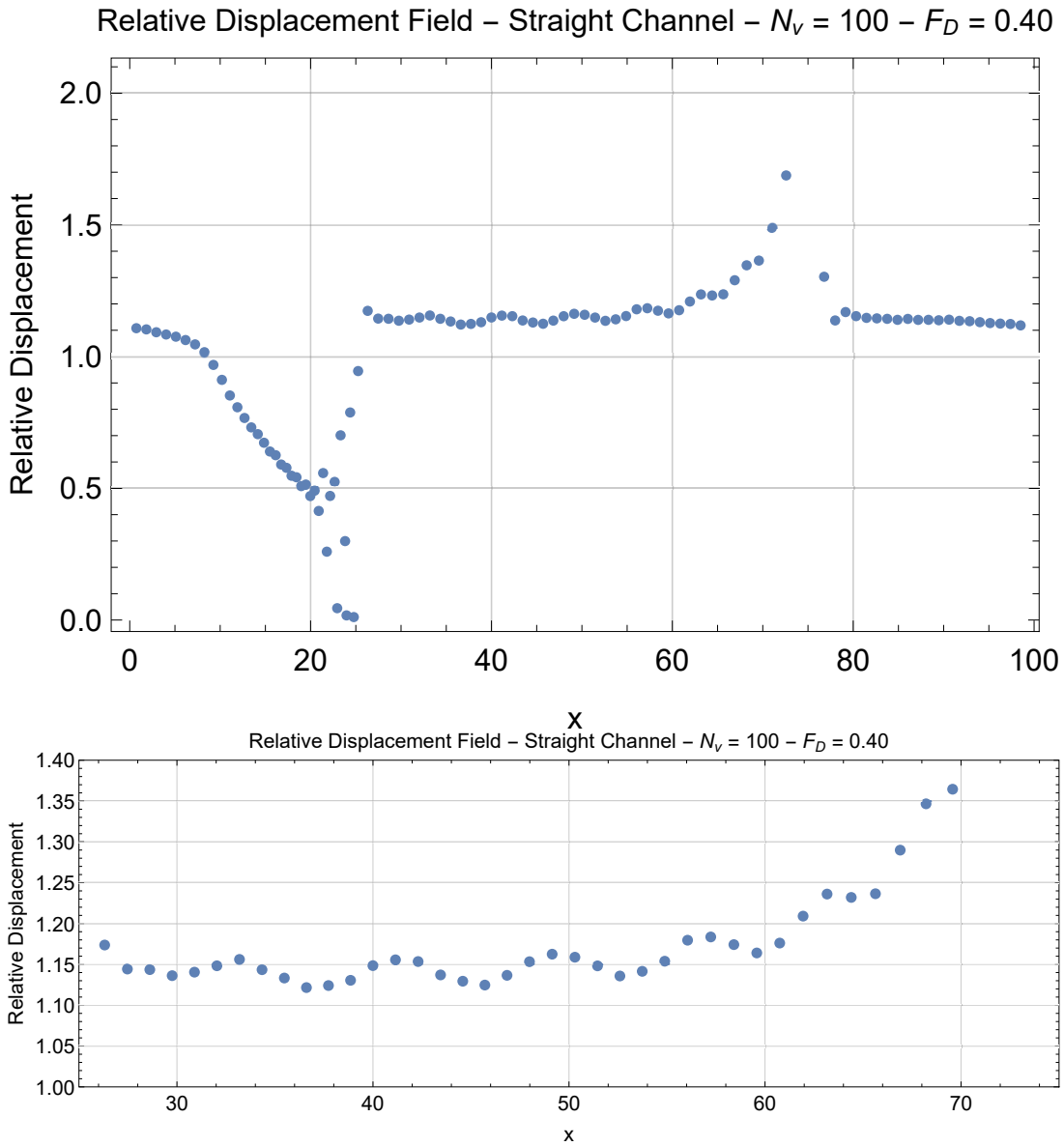

Figure 67: Representative plots of the relative displacements of neighbouring vortices along the straight channel. The lower figure focusses on just the narrow part of the channel to show the form of the soliton.

Figure 67 shows an example of the solitonic profile in the channel. The characteristic peaks, that flow against the direction of vortex flow, no longer represent the number of interstitial vortices in the channel. In [108], we identified a peak for each interstitial vortex; since the distribution of vortices is no longer uniform, this idea breaks down in the constriction. If one looks locally, between $30 < x < 50$, there are 17 vortices (thus three interstitials) and three peaks in fig. 67. We note that the distance between peaks varies along the constriction and three peaks is an approximation. The density drop off at the end of the constriction is responsible for the break down of the soliton chain; locally, it is well formed.

9.10 Remarks

We have studied a narrow constricted vortex flow channel to investigate the transition from two or three chains to a single chain by forcing a row-drop to occur at the aperture of constriction. Originally, we intended to investigate flow patterns and recombination mechanisms, but discovered the onset of chaos for specific drives and densities.

We categorised the flow patterns based on their previous positions along the channel and mapped a phase diagram for each of the four different channels we simulated. These phase diagrams have similar features to the phase diagrams of fractal dimension and Lyapunov exponents, quantifying which states are chaotic.

The signatures of chaos are present for high driving forces and critical points where a

reordering transition occurs. To improve the accuracy of results, smaller time steps and longer run times of the simulations will give more detailed data. Analysis will take significantly longer and there is no guarantee that the noise seen on the Lyapunov exponents will decrease significantly. Further work on this system warrants the exploration of more sophisticated techniques that quantify chaos more accurately.

Notably, we observe results in a discrete system that are common features of continuum flow: stagnation and turbulence. This is surprising since the fundamental physics of discrete flow can now be mapped onto equivalent fluid systems. As further work, the results in our system should be compared, in detail, with continuum flow systems, including pipes [99], to search for universality between them.

These results indicate the row-drop mechanism is more complex than originally thought. Whether chaos is detectable for row-drops in the wide channel is debatable since noise and fluctuations may dominate over chaos. As further work, the onset of chaos needs to be studied in the original density driven flow channel [111, 112] that inspired this work.

10 Conclusions

In conclusion, we have studied three systems of vortices in order to investigate row-changing mechanisms in the context of a parabollically confined channel. The purpose was to understand the cause of row-changing mechanisms in terms of the width of the channel, without the additional complexity of pinned vortices causing dislocations.

The cylindrical system was solved by discovering that circumference (acting as the channel width) and density can be scaled into a single parameter, α. Since α alone dictates the ground state structure, we know that a width and density have an equal role dictating structure. We found a set of phyllotactic states form, with increasing row number, as α increases. This increase in row number is previously understood to be a feature of confined systems with increasing density.

Our analytical methods for simplifying the energetic behaviour of the cylindrically confined system of vortices involves considering the system from an unusual perspective. We derive α through the symmetry in the phase diagram, which enables us to scale a 2D problem into 1D. The parabolic energy curve appears when we plot energy as a function of vector length, discovered by continued probing of the system numerically. Combined, these methods enable us to solve the structural phase diagram at zero temperature.

We extended the definition of α in the conical system to be a local quantity, and by optimising continuum flow, in coordination with the source and sink densities, we generated single-phase flow across the entire channel. We also demonstrated that the critical

values of α in the cylindrical system correspond to transition points on the cone for local values of α. An extension of this work relates back to an early motivator of this project: if the pinned vortex channel is set up in a 'funnel' structure, where the width is constantly changing, can a single phase flow be generated?

We studied the constricted channel to investigate row-drops in very thin channels. We observed and categorised flow patterns, reconstructed attractors from numerical data, and calculated fractal dimension and Lyapunov exponents. The emergence of chaos for particular choices of driving force and density shows that the mechanisms in wider channels are not easily scaled to thin channels. The results come from less contemporary techniques of quantifying chaos and further work should focus on using modern techniques to verify and increase understanding. Additionally, relating back to the original motivation, further research should investigate the possibility of chaos in the wider channel.

A Nearest Neighbour Model for the Single Bifurcating Chain

A.1 Introduction

Taking inspiration from ealier work [108], we set up an argument using a nearest-neighbour interaction and parabolic approximation to the background potential in the narrow channel to predict the behaviour of the amplitude parameter, A_y:

$$A_y = \sqrt{\frac{\sum_{i=0}^{N+n} y_i^2}{N+n}}. \tag{A.1}$$

We consider the static system with zero interstitial vortices ($n = 0$) and commensurate channel edges ($\Delta x = 0$). We have empirically observed through simulation that the positions of the i^{th} vortex is given by $\mathbf{r}_i = (i - 0.5, \pm(-1)^i A_y)$. For $A_y = 0$, the chain is one-dimensional (1D) and for $A_y > 0$, the chain is in the bifurcated zig-zag state.

Using the vortex-vortex interaction potential between two vortices separated by a distance r [23]:

$$V(r) = \log\left(\frac{r_c}{r}\right) + \left(\frac{r}{r_c}\right)^2 - \frac{1}{4}\left(\frac{r}{r_c}\right)^4 - \frac{3}{4}, \tag{A.2}$$

where $r_c = 3.33$ is the interaction cut-off length. The background confining potential along any line of constant x, for which $x \pmod 1 = 0.5$ (i.e. the line where the vortices can move along), is parabolic:

$$V_{\text{con}}(y) = \zeta(w) + \beta(w) y^2, \tag{A.3}$$

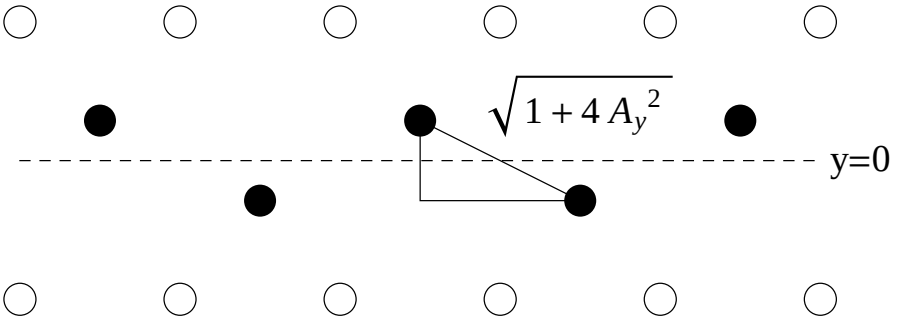

Figure 68: Nearest-Neighbour Distance in the Zig-Zag State.

where ζ and β are functions to be derived and w is the width of the channel. By sampling the potential energy along the line of constant x for various widths, we can numerically extract the variance of ζ and β with respect to width:

$$\zeta(w) \simeq 3.6 - 2.5(w) + 0.49(w)^2 \tag{A.4}$$

$$\beta(w) \simeq 2.7 - 0.75(w). \tag{A.5}$$

A.2 Ground State Solutions for A_y

We can work using the energy per vortex since the periodicity will take a summation of N identical energies. Figure 68 shows the distance between nearest neighbour vortices to be $\sqrt{1+4A_y^2}$. The total potential energy (with constants omitted) is:

$$U(A_y, w) \simeq -\frac{1}{2}\log\left(1+4A_y^2\right) + \frac{1+4A_y^2}{r_c^2} - \frac{1}{4}\left(\frac{(1+4A_y^2)^2}{r_c^4}\right) + \zeta(w) + \beta(w)A_y^2 \tag{A.6}$$

To find the ground state configuration, we find the energetic minimum by solving

$\partial U/\partial A_y = 0$.

$$\frac{\partial U}{\partial A_y} = \frac{-4A_y}{1+4A_y^2} + \frac{8A_y}{r_c^2} - \frac{4A_y(1+4A_y^2)}{r_c^4} + 2\beta(w)A_y = 0 \tag{A.7}$$

Multiplying through by $r_c^4(1+4A_y^2)$ yields:

$$A_y\left[(4r_c^2 - 2r_c^4 - 2 + r_c^4\beta(w)) + A_y^2(16r_c^2 - 16 + 4r_c^4\beta(w)) - 32A_y^4\right] = 0. \tag{A.8}$$

We can immediately see the trivial solution, $A_y = 0$, which is always true. The finite solution is obtained by solving the quadratic equation in A_y^2:

$$A_y^2 = \frac{1}{64}\left[16(1-r_c^2) - r_c^4\beta(w) \pm \sqrt{r_c^4\beta(w)(96 + 32r_c^2 + r_c^4\beta(w))}\right]. \tag{A.9}$$

This expression must be positive in order for A_y to be real. We search for the point where A_y^2 becomes zero to obtain the critical confinement strength. By setting the right hand side equal to zero, rearranging, squaring, and rearranging again we see:

$$\begin{aligned} 16(1-r_c^2) - r_c^4\beta_c &= \mp\sqrt{r_c^4\beta_c(96 + 32r_c^2 + r_c^4\beta_c)} \\ \Rightarrow 2(1-r_c^2)^2 - r_c^4\beta_c &= 0 \end{aligned} \tag{A.10}$$

which leads us to the expression for the critical confining strength:

$$\beta_c = \frac{2(1-r_c^2)^2}{r_c^4} \tag{A.11}$$

We can find the critical channel width using the approximation in equation (A.5) to be $w_c = 1.4$, which is within 5% of the result obtained numerically.

A.3 Order of the Zig-Zag Transition

To find the order of the transition, we compare the energies of the single and bifurcated chain at the critical point. The energy of the single chain, with $A_y = 0$, is:

$$U(A_y = 0, w) = \frac{1}{r_c^2} - \frac{1}{4r_c^4} + \zeta(w). \tag{A.12}$$

The bifurcated chain, at w_c, also has $A_y = 0$, which means the energy must be identical in both chains at this point. In this case, the first derivative of the ground state energy at $\beta(w_c)$ is non-diverging, thus the transition is not first order.

The first derivative of the single chain is:

$$\frac{\partial U}{\partial(w)} = \zeta'(w) \tag{A.13}$$

Provided the first derivative of the bifurcated chain's energy is not $\zeta'(w)$, there is a discontinuity which leads to a divergence in the second order derivative of the ground state energy implying a second order phase transition. The energy of the bifurcated chain

is given by:

$$
\begin{aligned}
&U(A_y > 0, w) = \\
&-\frac{1}{512 r_c^4}\Big[64 r_c^6 \beta(w)(1+2\beta(w)) + r_c^8 \beta^2(w)(1+8\beta(w)) \\
&+ 32\left(16 + \sqrt{r_c^4\beta(w)(96+32r_c^2+r_c^4\beta(w))}\right) \\
&- 48 r_c^4 \beta(w)\left(32 + \sqrt{r_c^4\beta(w)(96+32r_c^2+r_c^4\beta(w))}\right) \\
&+ 8\beta^2(w)\left(16 + \sqrt{r_c^4\beta(w)(96+32r_c^2+r_c^4\beta(w))}\right) \\
&- r_c^4\left(-640 + \beta(w)(-16 + \sqrt{r_c^4\beta(w)(96+32r_c^2+r_c^4\beta(w))}\right) \\
&+256 r_c^4 \log\left(\frac{1}{16}\left(32 - 16r_c^2 - r_c^4\beta(w) + \sqrt{r_c^4\beta(w)(96+32r_c^2+r_c^4\beta(w))}\right)\right)\Big] + \zeta(w).
\end{aligned}
\tag{A.14}
$$

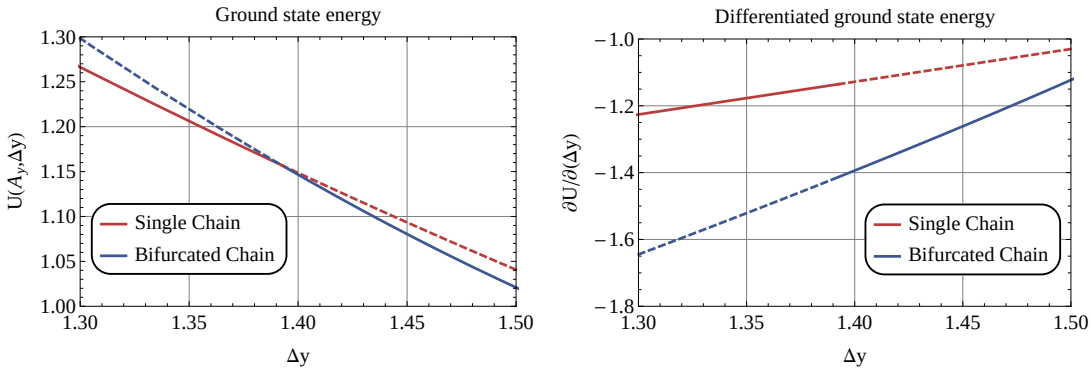

Figure 69: Ground state energy and its differential. Solid lines represent the system's preferred state and dashed lines show the continuation of the energies to clarify the energetic crossover at the transition. The discontinuity in the first derivative leads to a divergence in the second derivative implying a second order phase transition at $\beta(w_c)$.

This expression can be differentiated with respect to w and its value at w_c can be found to be:

$$\left.\frac{\partial U}{\partial(w)}\right|_{w_c} =$$

$$\zeta_c' + \beta_c' \Big(-12 r_c^{16} \beta_c^5 + 4096 \left(r_c^2 - 1\right)^2 \left(r_c^2 + 3\right) \sqrt{r_c^4 \beta_c \left(r_c^4 \beta_c + 32 r_c^2 + 96\right)}$$

$$- r_c^{12} \beta_c^4 \left[-12 \sqrt{r_c^4 \beta_c \left(r_c^4 \beta_c + 32 r_c^2 + 96\right)} + r_c^4 + 704 r_c^2 + 1376 \right]$$

$$- 128 r_c^4 \beta_c \left[-3 r_c^4 \left(3 \sqrt{r_c^4 \beta_c \left(r_c^4 \beta_c + 32 r_c^2 + 96\right)} - 128 \right) \right.$$

$$\left. -2 r_c^2 \left(7 \sqrt{r_c^4 \beta_c \left(r_c^4 \beta_c + 32 r_c^2 + 96\right)} + 64 \right) + 7 \sqrt{r_c^4 \beta_c \left(r_c^4 \beta_c + 32 r_c^2 + 96\right)} + 128 r_c^6 - 384 \right]$$

$$- r_c^8 \beta_c^3 \left[-r_c^4 \left(\sqrt{r_c^4 \beta_c \left(r_c^4 \beta_c + 32 r_c^2 + 96\right)} - 11376 \right) \right.$$

$$\left. -512 r_c^2 \left(\sqrt{r_c^4 \beta_c \left(r_c^4 \beta_c + 32 r_c^2 + 96\right)} - 68 \right) - 800 \sqrt{r_c^4 \beta_c \left(r_c^4 \beta_c + 32 r_c^2 + 96\right)} + 80 r_c^6 + 23552 \right]$$

$$- 64 r_c^4 \beta_c^2 \left[-r_c^4 \left(73 \sqrt{r_c^4 \beta_c \left(r_c^4 \beta_c + 32 r_c^2 + 96\right)} - 16 \right) \right.$$

$$- 8 r_c^2 \left(13 \sqrt{r_c^4 \beta_c \left(r_c^4 \beta_c + 32 r_c^2 + 96\right)} + 448 \right) + 48 \left(7 \sqrt{r_c^4 \beta_c \left(r_c^4 \beta_c + 32 r_c^2 + 96\right)} + 64 \right)$$

$$\left. -r_c^6 \left(\sqrt{r_c^4 \beta_c \left(r_c^4 \beta_c + 32 r_c^2 + 96\right)} - 592 \right) + 32 r_c^8 \right] \Big) \Big/$$

$$\left(128 r_c^4 \beta_c \left(r_c^4 \beta_c + 32 \left(r_c^2 + 3\right) \right) \left(r_c^4 \beta_c - \sqrt{r_c^4 \beta_c \left(r_c^4 \beta_c + 32 r_c^2 + 96\right)} + 16 r_c^2 - 32 \right) \right) \tag{A.15}$$

where $\zeta_c' = \partial\zeta/\partial(w)|_{w_c} \simeq -1.2$ and $\beta_c' = \partial\beta/\partial(w)|_{w_c} \simeq 0.75$. This expression can be evaluated numerically, setting $r_c = 3.33$ to give $\partial U/\partial(w)|_{w_c} \simeq 0.62$. Since we also know $\partial U/\partial(w)|_{w_c} = \zeta_c' \simeq -1.2$ for the single chain, there is a discontinuity in the first derivative at the critical point. There is a divergence in the second derivative of the free energy and so the transition is second order.

A.4 Critical Exponent for A_y in the Vicinity of w_c

Since we search for the critical exponent that describes A_y close to the transition, we divide out the overall factor of A_y in equation (A.7) and ignore the quartic term left in the expression. Rearranging gives an approximate expression for the amplitude:

$$A_y = \sqrt{\frac{2r_c^4 - 4r_c^2 + 2 - r_c^4\beta(w)}{16r_c^2 - 16 + 4r_c^4\beta(w)}}. \tag{A.16}$$

Setting the numerator equal to zero will give the critical channel width, which for the particular approximation of $\beta(w)$ gives $w_c \simeq 1.39$, which still agrees well with numerical calculations in [108]. Substituting in the expression for $\omega(w)^2$ and numerical values to 2 decimal places yields:

$$A_y \simeq \sqrt{\frac{0.35 - 0.25(w)}{(w) - 4.04}} = \sqrt{-0.25 - \frac{0.66}{(w) - 4.04}}. \tag{A.17}$$

Writing the remaining fraction in a form suitable for a geometric series expansion gives:

$$A_y = \sqrt{-0.25 + 0.16(1 - 0.25(w))^{-1}}. \tag{A.18}$$

Since $w \sim 1$, we are in a valid region for expansion, which to first order gives us:

$$A_y \simeq \sqrt{0.041(w) - 0.086}. \tag{A.19}$$

This expression gives a larger critical width, $w_c \simeq 2.10$. Figure 70 shows plots for higher order expansions which get closer to the transition point. The square root dependence is

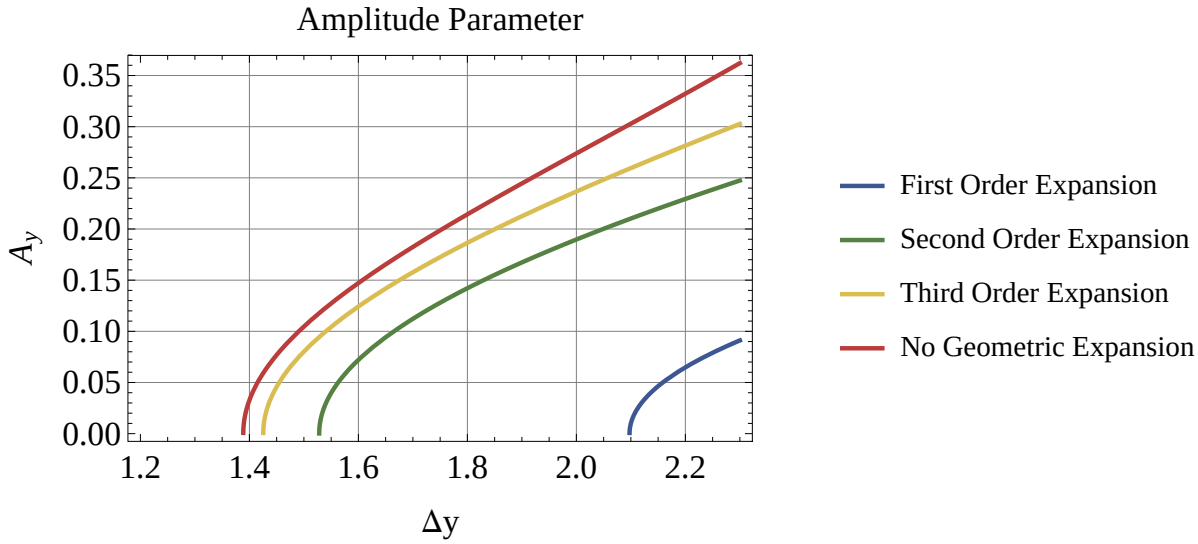

Figure 70: Plots for the amplitude parameter.

still visibly clear in all of these plots. This suggests, to leading order, that $A_y \sim \sqrt{w - w_c}$.

A.5 Energetic Stability of the Chains

We now analyse the stability of equation (A.6). Differentiating equation (A.7) at the energetic extrema yields:

$$\frac{\partial^2 U}{\partial A_y^2} = -\frac{4}{1+4A_y^2} + A_y^2\left(\frac{32}{(1+4A_y^2)^2} - \frac{48}{r_c^4}\right) - \frac{4}{r_c^4} + \frac{8}{r_c^2} + 2\beta(w). \tag{A.20}$$

For the single chain, we have already seen that $A_y = 0$ is a solution for all values of w. The stability of the extrema at this point is given by:

$$\left.\frac{\partial^2 U}{\partial A_y^2}\right|_{A_y=0} = \frac{8}{r_c^2} - \frac{4}{r_c^4} - 4 + 2\beta(w). \tag{A.21}$$

Previously we calculated the critical channel width from equation (A.16). In terms of $\beta(w)$, we could consider the critical strength, β_c, which is given by:

$$\beta_c = 2 - \frac{4}{r_c^2} + \frac{2}{r_c^4}. \tag{A.22}$$

We can now see that equation (A.21) is greater than zero (representing a stable minimum) if $\beta(w) > \beta_c$ (i.e. below w_c) and less than zero (representing an unstable maximum) if $\beta(w) < \beta_c$ (i.e. above w_c). This corresponds physically to the single chain being stable if $w < w_c$ and unstable if $w > w_c$. This result is also shown in [29] for a similar model, although it is presented without the derivation we provide.

Next, we consider the bifurcated chain for $w > w_c$, were we expect it to be stable. We study equation (A.20) and find where it is greater than zero:

$$-\frac{4}{1+4A_y^2} + A_y^2\left(\frac{32}{(1+4A_y^2)^2} - \frac{48}{r_c^4}\right) - \frac{4}{r_c^4} + \frac{8}{r_c^2} + 2\beta(w) > 0 \tag{A.23}$$

Substituting in equation (A.16) and imposing $\beta(w) = 2 - (4/r_c^4) + (2/r_c^2) - \epsilon < \beta_c$, where $0 < \epsilon \ll 1$.

$$\frac{-2\epsilon((12+\epsilon)r_c^4 + 3(\epsilon-4)r_c^8 + (\epsilon-2)^2 r_c^{12} - 4)}{(r_c^4-1)^2(2+(\epsilon-2)r_c^4)} > 0 \tag{A.24}$$

The numerator of this expression is dominated by the r_c^{12} term, which leads to an overall negative value. The denominator is overall negative due to the dominance of the r_c^4 term in the second bracket. The entire expression is therefore positive, indicating a local

minimum for the bifurcated chain (i.e. the bifurcated chain is stable above the critical width, or below the critical strength). Noticing that on the other side of the critical point, ϵ will become negative, the stability will change due to the overall factor of ϵ in the expression, so below the critical width the bifurcated chain is unstable.

B Expression for the Potential due to a Vortex Chain

B.1 Single Chain

We wish to calculate a convenient expression for the potential due to a chain of evenly spaced vortices in 2D.

$$V(x,y) = \sum_{n=-\infty}^{\infty} K_0\left(\sqrt{(x-na)^2+y^2})/\lambda\right). \tag{B.1}$$

Here, a is the vortex spacing and λ is the penetration depth. Using generalised functions and integrating, we can write this as:

$$V(x,y) = \int_{-\infty}^{\infty} \sum_{n=-\infty}^{\infty} \delta(z-(x-na)) K_0\left(\sqrt{z^2+y^2}/\lambda\right) \mathrm{d}z. \tag{B.2}$$

Writing this as a convolution:

$$V(x,y) = \left(\sum_{n=-\infty}^{\infty} \delta(x-na)\right) * K_0\left(\sqrt{x^2+y^2}/\lambda\right). \tag{B.3}$$

Noting the rule [104, p. 258]:

$$\mathcal{F}\{f*g\}_k = \tilde{f}(k)\tilde{g}(k), \tag{B.4}$$

we now use the Fourier transform on the sum of delta functions:

$$\mathcal{F}\left\{\sum_{n=-\infty}^{\infty} \delta(x-na)\right\}_k = \frac{2\pi}{a} \sum_{n=-\infty}^{\infty} \delta(k-2n\pi/a). \tag{B.5}$$

We now examine the Fourier transform of the Bessel function alone. Using the following definition for the Bessel function [32, §10.32.10]:

$$K_\nu(z) = \frac{1}{2}\left(\frac{1}{2}\right)^\nu \int_0^\infty \exp\left\{\left(-t - \frac{z^2}{4t}\right)\right\}\frac{\mathrm{d}t}{t^{\nu+1}}. \tag{B.6}$$

So for $\nu = 0$:

$$K_0(z) = \frac{1}{2}\int_0^\infty \frac{e^{-t-z^2/4t}\mathrm{d}t}{t}. \tag{B.7}$$

Calculating $\tilde{K}_0(k, y)$:

$$\tilde{K}_0(k, y) = \frac{1}{\sqrt{2\pi}}\frac{1}{2}\int_0^\infty \frac{e^{-t}}{t}\mathrm{d}t \int_{-\infty}^\infty e^{-ikx}e^{-(x^2+y^2)/4t\lambda^2}\mathrm{d}x. \tag{B.8}$$

$$= \frac{1}{\sqrt{2\pi}}\frac{1}{2}\int_0^\infty \frac{e^{-t}}{t}e^{-y^2/4t\lambda^2}\mathrm{d}t \int_{-\infty}^\infty e^{-ikx-x^2/4t\lambda^2}\mathrm{d}x. \tag{B.9}$$

The integral over x is solved by completing the square in the exponent and using the standard Gaussian integral:

$$\int_{-\infty}^\infty e^{-ikx-x^2/4t\lambda^2}\mathrm{d}x = \int_{-\infty}^\infty \exp\left\{\left(-\left(\left[\frac{x}{2\sqrt{t}\lambda} + ik\sqrt{t}\lambda\right]^2 + k^2t\lambda^2\right)\right)\right\}\mathrm{d}x. \tag{B.10}$$

$$= 2\sqrt{\pi}\sqrt{t}\lambda e^{-k^2t\lambda^2}. \tag{B.11}$$

Following on from here, $\tilde{K}_0(k,y)$ becomes:

$$\tilde{K}_0(k,y) = \frac{1}{\sqrt{2}} \int_0^\infty e^{-t(1+k^2\lambda^2)} e^{-y^2/4t\lambda^2} \frac{\mathrm{d}t}{\sqrt{t}}. \tag{B.12}$$

Using the substitution $t' = t(1+k^2\lambda^2)$, we are left with:

$$\tilde{K}_0(k,y) = \frac{\lambda}{\sqrt{2(1+k^2\lambda^2)}} \int_0^\infty \exp\left\{ \left(-t' - \frac{y^2(1+k^2\lambda^2)}{4\lambda^2 t'} \right) \right\} t'^{\,-1/2} \, \mathrm{d}t'. \tag{B.13}$$

Referring back to our previous definition of the Bessel Function, we see the solution relates to a fractional index Bessel function:

$$K_{-\frac{1}{2}}(z) = \frac{1}{2}\sqrt{\frac{2}{z}} \int_0^\infty e^{-t-z^2/4t} \frac{\mathrm{d}z}{\sqrt{z}}, \tag{B.14}$$

and so,

$$\tilde{K}_0(k,y) = \sqrt{\frac{y\lambda}{\sqrt{1+k^2\lambda^2}}} K_{-\frac{1}{2}} \left(\frac{y\sqrt{1+k^2\lambda^2}}{\lambda} \right). \tag{B.15}$$

We now substitute this into our previous expression and transform back:

$$V(x,y) = \frac{1}{\sqrt{2\pi}} \int_{-\infty}^\infty e^{ikx} \frac{2\pi}{a} \sum_{n=-\infty}^\infty \delta(k - 2n\pi/a) \sqrt{\frac{y\lambda}{\sqrt{1+k^2\lambda^2}}} K_{-\frac{1}{2}} \left(\frac{y\sqrt{1+k^2\lambda^2}}{\lambda} \right) \mathrm{d}k. \tag{B.16}$$

$$= \frac{\sqrt{2\pi\lambda}}{a} \sum_{n=-\infty}^\infty \int_{-\infty}^\infty e^{ikx} \delta(k - 2n\pi/a) \sqrt{\frac{y}{\sqrt{1+k^2\lambda^2}}} K_{-\frac{1}{2}} \left(\frac{y\sqrt{1+k^2\lambda^2}}{\lambda} \right) \mathrm{d}k. \tag{B.17}$$

The delta function does the integral over k:

$$V(x,y) = \frac{\sqrt{2\pi\lambda}}{a} \sum_{n=-\infty}^{\infty} e^{2n\pi i x/a} \sqrt{\frac{y}{\sqrt{1+(2n\pi\lambda/a)^2}}} K_{-\frac{1}{2}} \left(\frac{y\sqrt{1+(2n\pi\lambda/a)^2}}{\lambda} \right). \quad \text{(B.18)}$$

Now we are left with a Fourier series. Terms tend to zero quickly as $n \to \infty$ since [32, §10.25.3]:

$$K_\nu(z) \sim \sqrt{\frac{\pi}{2z}} e^{-z}. \quad \text{(B.19)}$$

So we have:

$$V(x,y) \simeq \frac{\sqrt{2\pi\lambda}}{a} \sqrt{y} K_{-\frac{1}{2}} \left(\frac{y}{\lambda} \right). \quad \text{(B.20)}$$

$$+ \sum_{n=1}^{\infty} \left[\frac{2\sqrt{2\pi\lambda}}{a} \cos\left(\frac{2m\pi x}{a} \right) \sqrt{\frac{y}{\sqrt{1+(2m\pi\lambda/a)^2}}} K_{-\frac{1}{2}} \left(\frac{y\sqrt{1+(2m\pi\lambda/a)^2}}{\lambda} \right) \right]. \quad \text{(B.21)}$$

We take the $m = \{0, \pm 1\}$ terms to get:

$$V(x,y) \simeq \frac{\sqrt{2\pi\lambda}}{a} \sqrt{y} K_{-\frac{1}{2}} \left(\frac{y}{\lambda} \right) + \frac{2\sqrt{2\pi\lambda}}{a} \cos\left(\frac{2\pi x}{a} \right) \sqrt{\frac{y}{\sqrt{1+(2\pi\lambda/a)^2}}} K_{-\frac{1}{2}} \left(\frac{y\sqrt{1+(2\pi\lambda/a)^2}}{\lambda} \right). \quad \text{(B.22)}$$

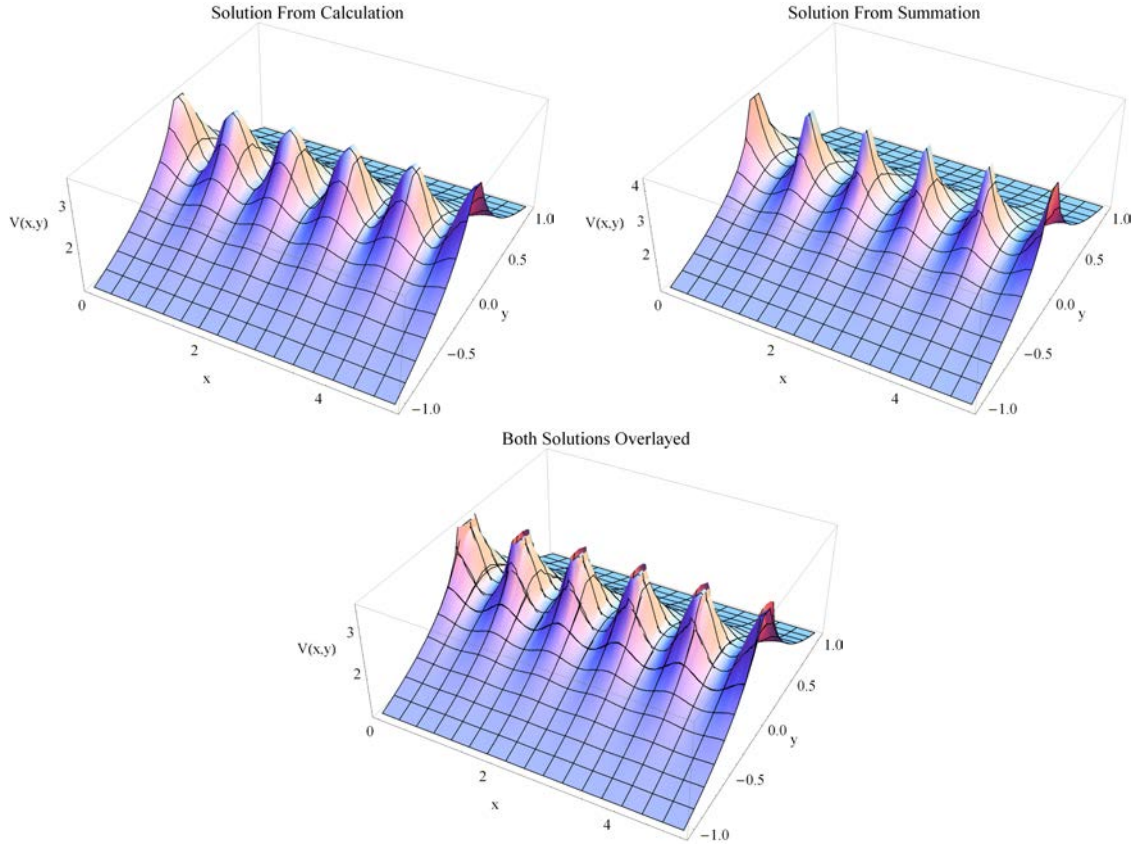

B.2 Two Commensurate Chains

The potential for two vortex chains is:

$$V^{\mathrm{T}}(x,y) = V\left(x, \frac{w}{2} - y\right) + V\left(x + \frac{\mu a}{2\pi}, \frac{w}{2} + y\right). \tag{B.23}$$

The first term represents the upper chain, and the second represents the lower chain, with an offset of $\mu a/2\pi$. We define:

$$V^{\mathrm{T}}(x,y) = V_0\left(\frac{w}{2} - y\right) + V_0\left(\frac{w}{2} + y\right) \tag{B.24}$$

$$+ \sum_{n=1}^{\infty}\left[V_m\left(\frac{w}{2} - y\right)\cos\left(\frac{2\pi n x}{a}\right) + V_m\left(\frac{w}{2} + y\right)\cos\left(\frac{2\pi n}{a}\left(x + \frac{\mu a}{2\pi}\right)\right)\right].$$

(B.25)

Where:

$$V_0(z) = \frac{\sqrt{2\pi\lambda}}{a}\sqrt{z}K_{-\frac{1}{2}}\left(\frac{z}{\lambda}\right). \tag{B.26}$$

$$V_m(z) = \frac{\sqrt{2\pi\lambda}}{a}\sqrt{\frac{z}{\sqrt{1+(2\pi m\lambda/a)^2}}}K_{-\frac{1}{2}}\left(\frac{z\sqrt{1+(2\pi m\lambda/a)^2}}{\lambda}\right). \tag{B.27}$$

For the un-sheared chains, we expect minima at $(m + a/2, 0)$, where $m \in \mathbb{Z}$. To check this, we consider:

$$V^{\mathrm{T}}(x,0) = V_0\left(\frac{w}{2}\right) + 2\sum_{m=1}^{\infty}\left[V_m\left(\frac{w}{2}\right)\cos\left(\frac{2\pi mx}{\lambda}\right)\right]. \tag{B.28}$$

The first term is constant along $y = 0$ and the second term is extremised by the cosine at integer values of $a/2$, or $x = na/2$ where $n \in \mathbb{Z}$. This can be seen by noticing that for $m = 1$ the extrema lie on these values. Higher order values of m have more extreme values, and the ones at $na/2$ are still there. Other extrema are suppressed by the quick decay of the Bessel Functions and so the $m = 1$ term dominates. The to find which are minima, we differentiate twice. We consider the case of half-integer values of a and integer values of a.

$$\left.\frac{\partial^2 V^T(x,0)}{\partial x^2}\right|_{x=na} = \frac{-8\pi^2}{a^2}\sum_{m=1}^{\infty}\left[m^2 V_m\left(\frac{w}{2}\right)\right]. \tag{B.29}$$

Here, the entire sum is positive, leaving the overall result negative. This means that on integer values of a, we have maxima, which is expected.

$$\left.\frac{\partial^2 V^T(x,0)}{\partial x^2}\right|_{x=(2n+1)a/2} = \frac{-8\pi^2}{a^2}\sum_{m=1}^{\infty}\left[m^2 V_m\left(\frac{w}{2}\right)(-1)^m\right]. \tag{B.30}$$

Here, the oscillating signs need to be taken into account. The $m = 1$ case leaves an overall positive contribution to the result, then the $m = 2$ term leaves an overall negative contribution, but is suppressed via the Bessel function, and each subsequent term is suppressed. Therefore, the overall sign is positive and thus we have minima at $x = (n + 1/2)a$ as expected.

B.3 Two Vortex Chains with a Shear

We search for the minima when there is a shear between two rows of chains.

$$V^{\mathrm{T}}(x,y) = V\left(x, \frac{w}{2} - y\right) + V\left(x + \frac{\mu a}{2\pi}, \frac{w}{2} + y\right). \tag{B.31}$$

Exact result is horrendous, need to see if approximations can be made. At least should be able to show that y position is non-zero.

B.4 Gaussian Potential

Although it appears rarely in physical situations, it is useful to calculate with Gaussian potentials due to their convenient forms. The calculation for the single chain is simpler

with Gaussian functions.

$$V(x,y) = \sum_{m=-\infty}^{\infty} e^{-(x-ma)^2-y^2}. \tag{B.32}$$

Following very similar steps we find:

$$V(x,y) = \frac{\sqrt{\pi}}{a} e^{-y^2} \left(1 + 2\sum_{n=1}^{\infty} \left[\cos\left(\frac{2n\pi x}{a}\right) e^{-n^2\pi^2/a^2}\right]\right). \tag{B.33}$$

These terms decay quickly (not as quickly as the Bessel function case) and we get a good approximation truncating at $n = 1$.

$$V(x,y) = \frac{\sqrt{\pi}}{a} e^{-y^2} \left(1 + 2\cos\left(\frac{2\pi x}{a}\right) e^{-\pi^2/a^2}\right). \tag{B.34}$$

B.5 Parabolic Approximation in the Un-sheared Channel

We are in a position to find an analytic approximation to the potential along $y = 0$ with two chains at $y = \pm w/2$. Writing the potential taking approximations where previously discussed:

$$V^T(x,y) = V_0\left(\frac{w}{2} - y\right) + V_0\left(\frac{w}{2} + y\right) + \left[V_1\left(\frac{w}{2} - y\right) + V_1\left(\frac{w}{2} - y\right)\right]\cos\left(\frac{2\pi x}{a}\right). \tag{B.35}$$

The V_0 and V_1 sums are even, which means we expect to find coefficients in even powers of y.

$$V^T(x,y) \simeq a_{0,0} + a_{0,2}y^2 + [a_{1,0} + a_{1,2}y^2]\cos\left(\frac{2\pi x}{a}\right). \tag{B.36}$$

We begin by expanding V_0. Using the approximate form of the modified Bessel function we get:

$$\begin{aligned} V_0\left(\frac{w}{2} \pm y\right) &= \frac{\sqrt{2\pi\lambda}}{a}\sqrt{\frac{w}{2} \pm y}K_{-\frac{1}{2}}\left(\frac{w/2 \pm y}{\lambda}\right) \\ &= \frac{\sqrt{2\pi\lambda}}{a}\sqrt{\frac{w}{2} \pm y}\sqrt{\frac{\pi\lambda}{2(w/2 \pm y)}}e^{-w/2\lambda}e^{\mp y/\lambda} \\ &= \frac{\pi\lambda}{a}e^{-w/2\lambda}\left(1 \mp \frac{y}{\lambda} + \frac{y^2}{2\lambda^2}\right). \end{aligned} \tag{B.37}$$

Thus summing both V_0 terms yields:

$$a_{0,0} = \frac{2\pi\lambda}{a}e^{-w/2\lambda} \tag{B.38}$$

$$a_{0,2} = \frac{\pi}{a\lambda}e^{-w/2\lambda}. \tag{B.39}$$

Likewise, for the V_1 terms, we take a similar approach, noting more complicated coefficients.

$$\begin{aligned} V_1\left(\frac{w}{2}\pm y\right) &= \frac{\sqrt{2\pi\lambda}}{a}\sqrt{\frac{w/2\pm y}{\sqrt{1+(2\pi\lambda/a)^2}}}K_{-\frac{1}{2}}\left(\frac{(w/2\pm y)\sqrt{1+(2\pi\lambda/a)^2}}{\lambda}\right) \\ &= \frac{\sqrt{2\pi\lambda}}{a}\sqrt{\frac{w/2\pm y}{\sqrt{1+(2\pi\lambda/a)^2}}}\sqrt{\frac{\pi\lambda}{2(w/2\pm y)\sqrt{1+(2\pi\lambda/a)^2}}}e^{-(w/2\pm y)\sqrt{1+(2\pi\lambda/a)^2}/\lambda} \\ &= \frac{\pi\lambda}{a\sqrt{1+(2\pi\lambda/a)^2}}e^{-w\sqrt{1+(2\pi\lambda/a)^2}/2\lambda}e^{\mp y\sqrt{1+(2\pi\lambda/a)^2}/\lambda} \\ &= \frac{\pi\lambda}{a\sqrt{1+(2\pi\lambda/a)^2}}e^{-w\sqrt{1+(2\pi\lambda/a)^2}/2\lambda}\left(1\mp y\frac{\sqrt{1+(2\pi\lambda/a)^2}}{\lambda}+y^2\frac{1+(2\pi\lambda/a)^2}{2\lambda^2}\right). \end{aligned} \tag{B.40}$$

Again, summing both the V_1 terms yields:

$$a_{1,0} = \frac{2\pi\lambda}{a\sqrt{1+(2\pi\lambda/a)^2}}e^{-w\sqrt{1+(2\pi\lambda/a)^2}/2\lambda} \tag{B.41}$$

$$a_{1,2} = \frac{\pi\sqrt{1+(2\pi\lambda/a)^2}}{a\lambda}e^{-w\sqrt{1+(2\pi\lambda/a)^2}/2\lambda}. \tag{B.42}$$

We can check the validity of this parabolic form by plotting. The approximation works well, and we are in a strong position to calculate things.

B.6 Variation with Channel Width

We have previously calculated transition points using a purely numerical approximation to the potential with changing channel width in appendix A. With this information, we can now calculate an analytical approximation. For this particular calculation, we are

interested in a stationary system, with a commensurate number of vortices. The single chain will form in the x minima, so we apply a minus sign to the cosine part of the potential. We search for a form of the potential that looks like:

$$V(y) = \zeta(w') + \beta(w')y^2. \tag{B.43}$$

We use $w' = w - \sqrt{3}$ because it keeps the methodology consistent between the two papers, and since we will Taylor expand about $w = \sqrt{3}$, the prime notation works as an 'additional width' parameter.

Writing down our form of the potential, we have:

$$V(y) = \left[\frac{2\pi\lambda}{a}e^{-w/2\lambda} - \frac{2\pi\lambda}{a\sqrt{\gamma}}e^{-w\sqrt{\gamma}/2\lambda}\right] + \left[\frac{\pi}{a\lambda}e^{-w/2\lambda} - \frac{\pi\sqrt{\gamma}}{a\lambda}e^{-w\sqrt{\gamma}/2\lambda}\right]y^2, \tag{B.44}$$

where $\gamma = 1 + (2\pi\lambda/a)^2$. We investigate the potential as the width deviates away from its natural length, $w = \sqrt{3}$, so we Taylor expand about this point.

$$\begin{aligned}
\zeta(w - \sqrt{3} = w') &= \frac{2\pi\lambda}{a}e^{-\sqrt{3}/2\lambda}\left(1 - \frac{w-\sqrt{3}}{2\lambda} + \frac{(w-\sqrt{3})^2}{8\lambda^2}\right) \\
&\quad - \frac{2\pi\lambda}{a\sqrt{\gamma}}e^{-\sqrt{3\gamma}/2\lambda}\left(1 - \frac{\sqrt{\gamma}}{2\lambda}(w-\sqrt{3}) + \frac{\gamma}{8\lambda^2}(w-\sqrt{3})^2\right) \\
&= \frac{2\pi\lambda}{a}e^{-\sqrt{3}/2\lambda}\left(1 - \frac{w'}{2\lambda} + \frac{(w')^2}{8\lambda^2}\right) \\
&\quad - \frac{2\pi\lambda}{a\sqrt{\gamma}}e^{-\sqrt{3\gamma}/2\lambda}\left(1 - \frac{\sqrt{\gamma}}{2\lambda}w' + \frac{\gamma}{8\lambda^2}(w')^2\right)
\end{aligned} \tag{B.45}$$

$$\begin{aligned}\beta(w') = &\frac{\pi}{a\lambda} e^{-\sqrt{3}/2\lambda} \left(1 - \frac{w'}{2\lambda}\right) \\ &- \frac{\pi\sqrt{\gamma}}{a\lambda} e^{-\sqrt{3\gamma}/2\lambda} \left(1 - \frac{\sqrt{\gamma}}{2\lambda}(w')^2\right).\end{aligned} \tag{B.46}$$

Previously, we took ζ to second order and β to first order. We can now compare these coefficients with ones we already calculated. Note that they were calculated for an approximate form of the interaction potential, with multiple rows of vortices so we expect this result to differ from eqs. (A.4) and (A.5).

$$\zeta(w') = 3.19237 - 1.42696w' + 0.303853w'^2 \tag{B.47}$$

$$\beta(w') = 1.21541 - 0.324894w'. \tag{B.48}$$

Although these results differ from those presented in appendix A, we would need to consider additional terms in the expansion to accurately substitute $w' = w - \sqrt{3}$ back in.

C Calculating the Elastic Strain of the Lattice Confined to a Cylinder

C.1 Introduction

In this appendix, we demonstrate the parabolic nature of the internal energy of the generic cylinder model when expressed as a function of lattice vector length. We take inspiration from the methods presented in [100, §1.2.4] and [64, §1-5], which are adapted to the triangular lattice. We construct a 2D lattice using the following vectors:

$$\mathbf{a} = \begin{pmatrix} -\gamma \\ \frac{1}{2\gamma} \end{pmatrix} \qquad \mathbf{b} = \begin{pmatrix} \gamma \\ \frac{1}{2\gamma} \end{pmatrix}. \tag{C.1}$$

The parameter γ can take any value larger than 0 and generates a lattice with unit cell of size unity. The vector length is $L = \sqrt{4\gamma^4 + 1}/2\gamma$. Constructing a lattice using these vectors and applying a repulsive particle-particle interaction, we find an energy-per-particle dependence on vector length that appears parabolic. The energy per particle is given by:

$$E(\gamma) = \sum_{m,n} V(|m\mathbf{a} + n\mathbf{b}|) \qquad \forall (m \neq 0) \vee (n \neq 0), \tag{C.2}$$

where $V(r)$ is an interaction potential. The $m = n = 0$ term is omitted since it is a self-interaction and can induce a singularity depending on the form of the potential. When numerically calculating the energy, we choose a sensible cut-off length at the point where the distance causes the potential to yield a value lower than the working numerical

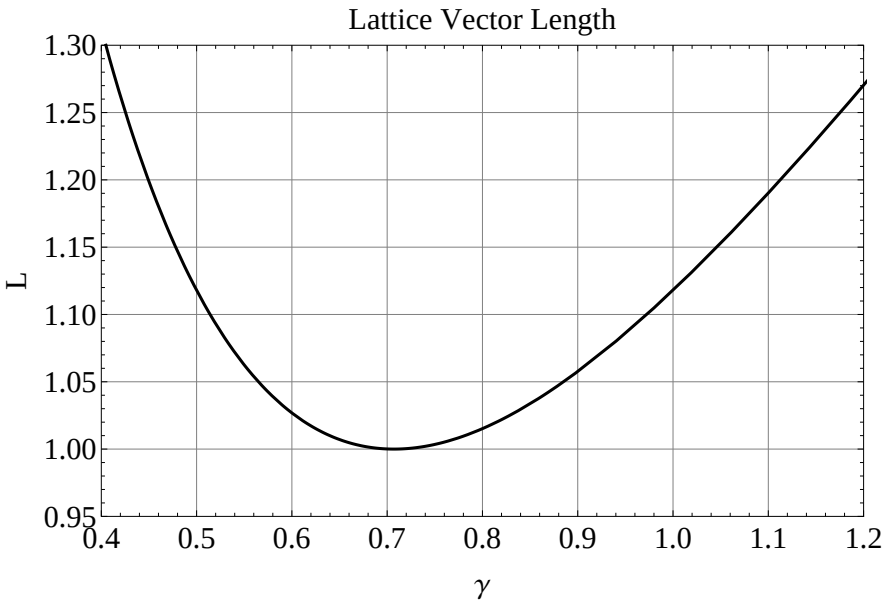

Figure 71: Plot of $L = \sqrt{4\gamma^4 + 1}/2\gamma$. Note that there are generally two solutions to $L = \gamma$ meaning that the internal energy curve is multivalued. Both values of interest are addressed individually in this section.

precision (typically $\sim 10^{-16}$). Since the energy is calculated as a truncated infinite summation, direct expansion is difficult (although has been done with some success) and a different argument is needed to show the origin of the parabolic form. We consider small deformations of the perfect lattice (where the energetic minimum is) and construct a strain tensor of the lattice point deviations away from hexagonality. Given the symmetries and form of the lattice vectors, we can parameterise the deformation in terms of the change in lattice vector length, δ_L, and angle of deviation away from perfect hexagonality, δ_θ. We consider both minima values of γ separately.

C.2 $\gamma = 1/\sqrt{2\sqrt{3}}$

Consider Figure 74, inspired by the methods in: Deviations away from the perfect lattice as γ increases are shown while retaining the defined symmetries of the lattice.

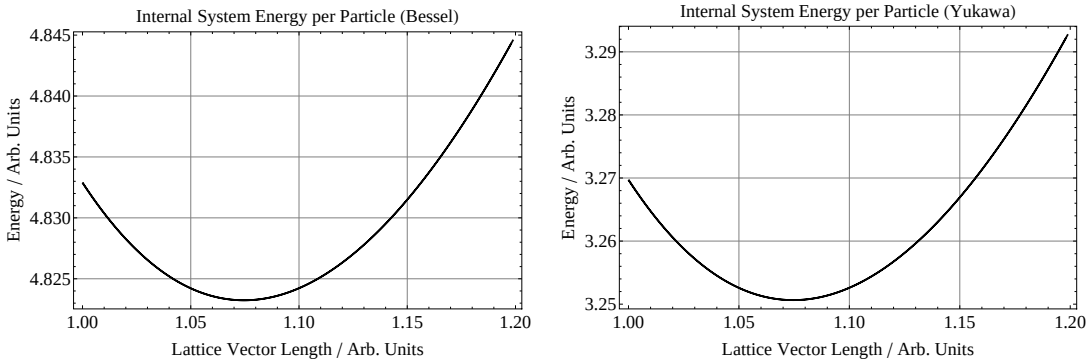

Figure 72: Parabolic form of the energy for the interacting potentials $K_0(r)$ and e^{-r}/r. The energetic minimum occurs when the lattice is perfectly hexagonal with values of $\gamma = 1/\sqrt{2\sqrt{3}}$ and $\gamma = \sqrt{\sqrt{3}/2}$. There is an end-point on the far left of the curve where, as γ increases, the curve retraces itself.

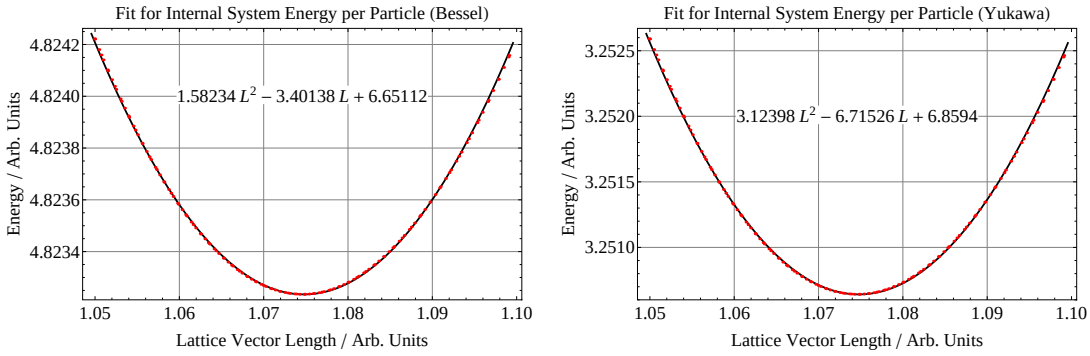

Figure 73: Numerically obtained quadratic fits for the energy curves within a range of ± 0.025 of the minimum. Most transitions occur in this range.

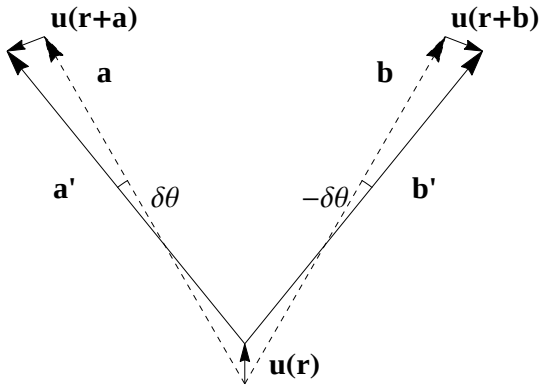

$$\mathbf{a} = \begin{pmatrix} -\sqrt{\frac{1}{2\sqrt{3}}} \\ \sqrt{\frac{\sqrt{3}}{2}} \end{pmatrix} \qquad \mathbf{b} = \begin{pmatrix} \sqrt{\frac{1}{2\sqrt{3}}} \\ \sqrt{\frac{\sqrt{3}}{2}} \end{pmatrix}$$

$$|\mathbf{a}'| = |\mathbf{b}'| = |\mathbf{a}|(1+\delta_L) = |\mathbf{b}|(1+\delta_L)$$

Figure 74: Illustration of an infinitesimal deformation of the lattice.

We express the new vectors in terms of their angle and length, while using $|\mathbf{a}| = |\mathbf{b}| \equiv a$.

$$\mathbf{a}' = a(1+\delta_L) \begin{pmatrix} \cos(2\pi/3 + \delta_\theta) \\ \sin(2\pi/3 + \delta_\theta) \end{pmatrix} \tag{C.3}$$

$$\mathbf{b}' = a(1+\delta_L) \begin{pmatrix} \cos(\pi/3 - \delta_\theta) \\ \sin(\pi/3 - \delta_\theta) \end{pmatrix}. \tag{C.4}$$

Considering $\mathbf{a}'$ first, we make use of the multiple angle formulae for trigonometric functions:

$$\mathbf{a}' = a(1+\delta_L) \begin{pmatrix} \cos(2\pi/3)\cos(\delta_\theta) - \sin(2\pi/3)\sin(\delta_\theta) \\ \sin(2\pi/3)\cos(\delta_\theta) + \cos(2\pi/3)\sin(\delta_\theta) \end{pmatrix} \tag{C.5}$$

$$= \frac{a(1+\delta_L)}{2} \begin{pmatrix} -\cos(\delta_\theta) - \sqrt{3}\sin(\delta_\theta) \\ \sqrt{3}\cos(\delta_\theta) - \sin(\delta_\theta) \end{pmatrix}. \tag{C.6}$$

Taking small-angle approximations and expressing $\mathbf{a}'$ as the original vector plus a perturbation:

$$\mathbf{a}' = \frac{a(1+\delta_L)}{2}\begin{pmatrix} -1-\sqrt{3}\delta_\theta \\ \sqrt{3}-\delta_\theta \end{pmatrix} \tag{C.7}$$

$$= \frac{a}{2}\begin{pmatrix} -1 \\ \sqrt{3} \end{pmatrix} + \frac{a}{2}\begin{pmatrix} -\delta_L-\sqrt{3}\delta_\theta \\ \sqrt{3}\delta_L-\delta_\theta \end{pmatrix}. \tag{C.8}$$

Next, we express the new vectors in terms of the displacement $\mathbf{u}$ and the old vectors and take the Taylor expansion of $\mathbf{u}(\mathbf{r}+\mathbf{a})$.

$$\mathbf{a}' = \mathbf{a} + \mathbf{u}(\mathbf{r}+\mathbf{a}) - \mathbf{u}(\mathbf{r}) \tag{C.9}$$

$$= \mathbf{a} + (\mathbf{a}\cdot\nabla)\mathbf{u}(\mathbf{r}) \tag{C.10}$$

$$= \mathbf{a} + \left(-\gamma\frac{\partial}{\partial x} + \frac{1}{2\gamma}\frac{\partial}{\partial y}\right)\mathbf{u}(\mathbf{r}). \tag{C.11}$$

We now have two equations to be solved:

$$-\gamma\frac{\partial u_x}{\partial x} + \frac{1}{2\gamma}\frac{\partial u_x}{\partial y} = \frac{a}{2}(-\delta_L - \sqrt{3}\delta_\theta) \tag{C.12}$$

$$-\gamma\frac{\partial u_y}{\partial x} + \frac{1}{2\gamma}\frac{\partial u_y}{\partial y} = \frac{a}{2}(\sqrt{3}\delta_L - \delta_\theta). \tag{C.13}$$

We can find the remaining two equations needed to find all the $\partial u_i/\partial x_j$ elements by considering the same prescription for $\mathbf{b}'$.

$$\mathbf{b}' = \frac{a}{2}\begin{pmatrix} 1 \\ \sqrt{3} \end{pmatrix} + \frac{a}{2}\begin{pmatrix} \delta_L + \sqrt{3}\delta_\theta \\ \sqrt{3}\delta_L - \delta_\theta \end{pmatrix} \tag{C.14}$$

$$= \mathbf{b} + \left(\gamma\frac{\partial}{\partial x} + \frac{1}{2\gamma}\frac{\partial}{\partial y}\right)\mathbf{u}(\mathbf{r}). \tag{C.15}$$

$$\gamma\frac{\partial u_x}{\partial x} + \frac{1}{2\gamma}\frac{\partial u_x}{\partial y} = \frac{a}{2}(-\delta_L + \sqrt{3}\delta_\theta) \tag{C.16}$$

$$\gamma\frac{\partial u_y}{\partial x} + \frac{1}{2\gamma}\frac{\partial u_y}{\partial y} = \frac{a}{2}(\sqrt{3}\delta_L - \delta_\theta). \tag{C.17}$$

We construct the strain tensor, $u_{ik} = (\partial u_i/\partial x_k + \partial u_k/\partial x_i)/2$, with the solutions for $\partial u_i/\partial x_j$ [64]:

$$u_{ik} = \begin{pmatrix} \frac{\delta_L}{\sqrt{3}} + \delta_\theta & 0 \\ 0 & \sqrt{3}\delta_L - \delta_\theta \end{pmatrix}. \tag{C.18}$$

We next find u_{ik} for the other minima before analysing the energetics of both minima concurrently.

C.3 $\gamma = \sqrt{\sqrt{3}/2}$

The prescription is similar when the hexatic bond angle is $2\pi/3$.

$$\mathbf{a}' = a(1+\delta_L)\begin{pmatrix} \cos(5\pi/6+\delta_\theta) \\ \sin(5\pi/6+\delta_\theta) \end{pmatrix} \tag{C.19}$$

$$\mathbf{b}' = a(1+\delta_L)\begin{pmatrix} \cos(\pi/6-\delta_\theta) \\ \sin(\pi/6-\delta_\theta) \end{pmatrix}. \tag{C.20}$$

Following the identical method, we generate the following equations to solve:

$$-\gamma\frac{\partial u_x}{\partial x} + \frac{1}{2\gamma}\frac{\partial u_x}{\partial y} = \frac{a}{2}(-\sqrt{3}\delta_L - \delta_\theta) \tag{C.21}$$

$$-\gamma\frac{\partial u_y}{\partial x} + \frac{1}{2\gamma}\frac{\partial u_y}{\partial y} = \frac{a}{2}(\delta_L - \sqrt{3}\delta_\theta) \tag{C.22}$$

$$\gamma\frac{\partial u_x}{\partial x} + \frac{1}{2\gamma}\frac{\partial u_x}{\partial y} = \frac{a}{2}(-\sqrt{3}\delta_L + \delta_\theta) \tag{C.23}$$

$$\gamma\frac{\partial u_y}{\partial x} + \frac{1}{2\gamma}\frac{\partial u_y}{\partial y} = \frac{a}{2}(\delta_L - \sqrt{3}\delta_\theta). \tag{C.24}$$

Following from this, we find:

$$u_{ik} = \begin{pmatrix} \delta_L + \frac{\delta_\theta}{\sqrt{3}} & 0 \\ 0 & \delta_L - \sqrt{3}\delta_\theta \end{pmatrix}. \tag{C.25}$$

C.4 Relating δ_L to δ_θ

Since the lattice vectors depend on a single variable, there must be a one-to-one mapping between δ_L and δ_θ. An exact result may be unhelpful in finding a small-length scale or angular dependence. In the following steps, we make small-angle approximations where

appropriate. Considering the perturbed lattice to be a rotation and rescaling of the perfect lattice:

$$\begin{pmatrix} \cos(\delta_\theta) & -\sin(\delta_\theta) \\ \sin(\delta_\theta) & \cos(\delta_\theta) \end{pmatrix} \begin{pmatrix} \gamma \\ \frac{1}{2\gamma} \end{pmatrix} (1+\delta_L) = \begin{pmatrix} \gamma' \\ \frac{1}{2\gamma'} \end{pmatrix} \tag{C.26}$$

Using the small-angle approximation, we generate two equations enabling us to eliminate γ':

$$\gamma' = \left(\gamma - \frac{\delta_\theta}{2\gamma}\right)(1+\delta_L) \tag{C.27}$$

$$\frac{1}{2\gamma'} = \left(\delta_\theta\gamma + \frac{1}{2\gamma}\right)(1+\delta_L).. \tag{C.28}$$

Substituting and rearranging yields a quadratic equation in δ_θ:

$$\delta_\theta^2 + \delta_\theta\left[\frac{1}{2\gamma^2} - 2\gamma^2\right] + \left[\frac{1}{(1+\delta_L)^2} - 1\right] = 0. \tag{C.29}$$

Solving gives:

$$\delta_\theta = \frac{(4\gamma^4-1)(1+\delta_L) \pm \sqrt{(1+\delta_L)^2(4\gamma^4+1)^2 - 16\gamma^4}}{4(1+\delta_L)\gamma^2}. \tag{C.30}$$

Once each value is substituted, the solution we choose is the one such that $\delta_\theta(\delta_L = 0) = 0$.

C.5 $\gamma = 1/\sqrt{2\sqrt{3}}$

The expression reduces to:

$$\delta_\theta = -\frac{1+\delta_L \pm \sqrt{1+4\delta_L(2+\delta_L)}}{\sqrt{3}(1+\delta_L)}. \tag{C.31}$$

The negative square root satisfies the boundary condition.

$$\delta_\theta = \frac{1}{\sqrt{3}}\left[1 - \frac{\sqrt{1+4\delta_L(2+\delta_L)}}{1+\delta_L}\right]. \tag{C.32}$$

Taking Maclaurin expansions of the numerator and denominator and taking the lowest order term (since $\delta_L \ll 1$):

$$\delta_\theta = \frac{1}{\sqrt{3}}\left[1 - (1+4\delta_L + O(\delta_L^2))(1-\delta_L + O(\delta_L^2))\right] \tag{C.33}$$

$$\simeq -\sqrt{3}\delta_L. \tag{C.34}$$

C.6 $\gamma = \sqrt{\sqrt{3}/2}$

This time, the expression reduces to:

$$\delta_\theta = \frac{1+\delta_L \pm \sqrt{1+4\delta_L(2+\delta_L)}}{\sqrt{3}(1+\delta_L)}. \tag{C.35}$$

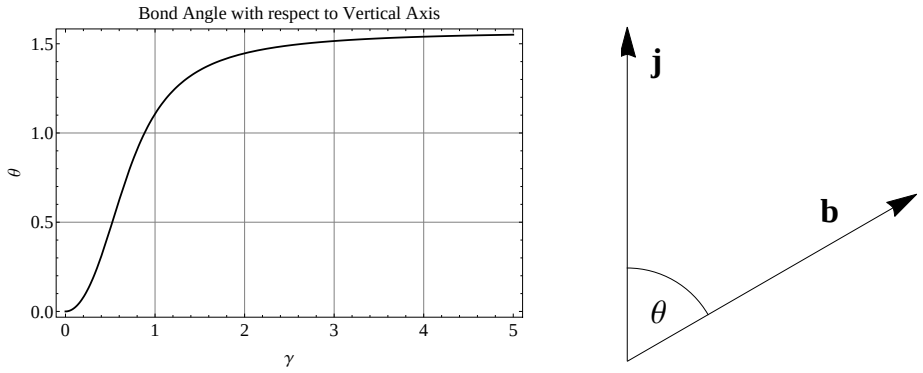

Figure 75: Plot and diagram showing the bond angle, θ, between $\hat{\mathbf{j}}$ and $\mathbf{b}$ as γ varies.

Again, the negative square root is used. This has identical form to the other case with an overall minus sign, leading us immediately to the approximate form:

$$\delta_\theta \simeq \sqrt{3}\delta_L. \tag{C.36}$$

We can explain the sign difference by referring back to Figure 71. We see that depending on which side of $\gamma = 1/\sqrt{2}$ the system is on, L is either decreasing or increasing. Additionally, by construction, the bond angle increases with γ; we can see this by calculating the bond angle with respect to the vertical direction with $\mathbf{b} \cdot \hat{\mathbf{j}}$:

$$\theta = \cos^{-1}\left(\frac{1}{\sqrt{4\gamma^4 + 1}}\right). \tag{C.37}$$

Plotting this clearly shows an entirely positive gradient meaning $\delta_\theta > 0$.

When $\gamma = 1/\sqrt{2\sqrt{3}}$, since the bond angle is increasing and bond length is decreasing with respect to γ, the minus sign we derive is justified. Similarly, when $\gamma = \sqrt{\sqrt{3}/2}$, the bond angle and length are both increasing with respect to γ so the positive proportionality is

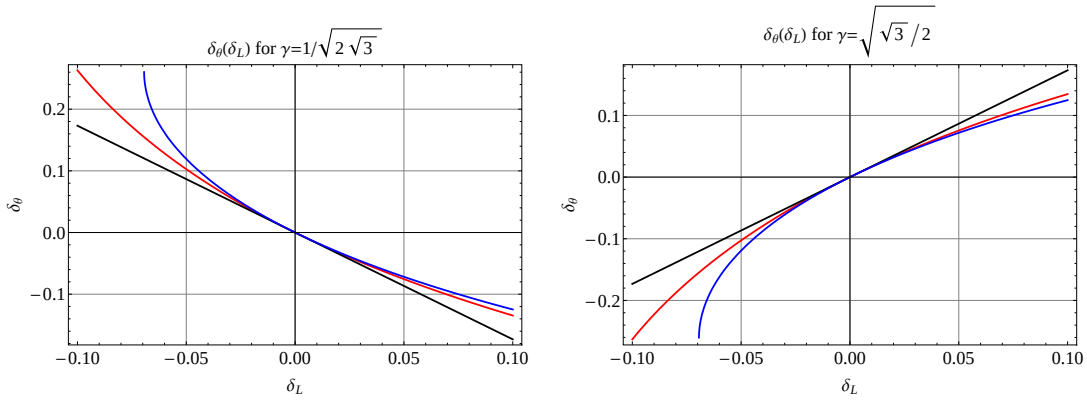

Figure 76: Plots of $\delta_\theta(\delta_L)$. Exact solutions are blue, small-angle solutions are red, and the linear expansion is black.

justified.

The validity of these approximations can be seen by plotting.

C.7 Energetics

We now consider the free energy of a system under elastic strain in 2D. The free energy is given by [64, §4]:

$$F = \mu(u_{ij} - \frac{1}{2}\delta_{ij}u_{kk})^2 + \frac{1}{2}Ku_{kk}^2, \tag{C.38}$$

where μ is the shear modulus and K is the bulk modulus. Expanding the bracket and substituting in the terms from the strain tensor yields:

$$F = \mu(u_{ij}u_{ij} - u_{kk}^2 + \frac{1}{4}\delta_{ij}\delta_{ij}u_{kk}^2) + \frac{1}{2}Ku_{kk}^2 \tag{C.39}$$

$$= \frac{1}{2}(\mu + K)u_{kk}^2 \tag{C.40}$$

$$= \frac{1}{2}(\mu + K)\left(\frac{\partial u_x}{\partial x}^2 + \frac{\partial u_y}{\partial y}^2\right) \tag{C.41}$$

$$F\left(\gamma = 1/\sqrt{2\sqrt{3}}\right) = \frac{1}{2}(\mu + K)\left(\left(\delta_L + \frac{\delta_\theta}{\sqrt{3}}\right)^2 + \left(\delta_L - \sqrt{3}\delta_\theta\right)^2\right) \tag{C.42}$$

$$= 2(\mu + K)\delta_L^2 \tag{C.43}$$

$$F\left(\gamma = \sqrt{\sqrt{3}/2}\right) = \frac{1}{2}(\mu + K)\left(\left(\frac{\delta_L}{\sqrt{3}} + \delta_\theta\right)^2 + \left(\sqrt{3}\delta_L - \delta_\theta\right)^2\right) \tag{C.44}$$

$$= \frac{8}{3}(\mu + K)\delta_L^2. \tag{C.45}$$

C.8 Exact Solution for $\delta_\theta(\delta_L)$

For completeness, we derive the exact form of $\delta_\theta(\delta_L)$. Again, starting with a rotation matrix and scaling, but keeping the trigonometric form:

$$\gamma' = \left(\cos(\delta_\theta)\gamma - \frac{\sin(\delta_\theta)}{2\gamma}\right)(1 + \delta_L) \tag{C.46}$$

$$\frac{1}{2\gamma'} = \left(\sin(\delta_\theta)\gamma + \frac{\cos(\delta_\theta)}{2\gamma}\right)(1 + \delta_L). \tag{C.47}$$

Eliminating γ' leaves:

$$\frac{1}{2(1+\delta_L)^2} = \left(\cos(\delta_\theta)\gamma - \frac{\sin(\delta_\theta)}{2\gamma}\right)\left(\sin(\delta_\theta)\gamma + \frac{\cos(\delta_\theta)}{2\gamma}\right) \tag{C.48}$$

$$= \frac{1}{2}\left[\sin(2\delta_\theta)\left(\gamma^2 - \frac{1}{4\gamma^2}\right) + \cos(2\delta_\theta)\right] \tag{C.49}$$

$$= \frac{1}{2}\left[\Gamma\sin(2\delta_\theta) + \sin\left(2\delta_\theta + \frac{\pi}{2}\right)\right] \tag{C.50}$$

$$= \frac{\pm\sqrt{1+\Gamma^2}}{2}\sin\left(2\delta_\theta + \sin^{-1}\left(\frac{1}{\pm\sqrt{1+\Gamma^2}}\right)\right), \tag{C.51}$$

where $\Gamma = \gamma^2 - 1/4\gamma^2$. We take the positive value of the square root, with the signs accounted for explicitly outside the roots; there are four possible solutions at this stage $(++, +-, -+, --)$. The inverse sine term represents the phase of the superposed functions on the previous line. Rearranging, taking the inverse sine, and using the identity $\sin^{-1}(1/x) \equiv \csc^{-1}(x)$ we find:

$$\delta_\theta(\delta_L) = \frac{1}{2}\left[\pm\csc^{-1}\left((1+\delta_L)^2\sqrt{1+\Gamma^2}\right) \pm \csc^{-1}\left(\sqrt{1+\Gamma^2}\right)\right]. \tag{C.52}$$

For each case, $\sqrt{1+\Gamma^2} = 2/\sqrt{3}$, so $\csc^{-1}\left(2/\sqrt{3}\right) = \pi/3$. With the boundary condition, $\delta_\theta(\delta_L = 0) = 0$, we narrow down the solutions to two possibilities $(+-, -+)$:

$$\delta_\theta(\delta_L) = \frac{1}{2}\left[\pm\csc^{-1}\left(\frac{2(1+\delta_L)^2}{\sqrt{3}}\right) \mp \frac{\pi}{3}\right]. \tag{C.53}$$

Finally, we choose the solution that matches the expected sign of the gradient from previous arguments. The inverse cosec of a positive argument always has negative gradient,

so we choose:

$$\delta_\theta\left(\delta_L;\gamma=1/\sqrt{2\sqrt{3}}\right)=\frac{1}{2}\left[\csc^{-1}\left(\frac{2(1+\delta_L)^2}{\sqrt{3}}\right)-\frac{\pi}{3}\right] \tag{C.54}$$

$$\delta_\theta\left(\delta_L;\gamma=\sqrt{\sqrt{3}/2}\right)=\frac{1}{2}\left[\frac{\pi}{3}-\csc^{-1}\left(\frac{2(1+\delta_L)^2}{\sqrt{3}}\right)\right]. \tag{C.55}$$

These functions fit to numerically calculated angles as expected. Furthermore, a Maclaurin expansion of these functions gives us the same linear approximation we derived from the small-angle approximation.

D Script for Finding Structural Ground States on the Cylinder

The script, as it appears in the Mathematica GUI environment, is included below. It succesfully runs in version 11.0.

In[1]:=
```
Clear[m, n, Alpha];

AlphaMinus[m_, n_] := 2 (m^2 - m n + n^2)/Sqrt[3];
AlphaPlus[m_, n_] := 2 (m^2 + m n + n^2)/Sqrt[3];
LatticeVector[m_, n_] :=
  If[m != n, {-n, (m Alpha - n Sqrt[Alpha^2 - (m^2 - n^2)^2])/(m^2 -
        n^2)}/Sqrt[Alpha], {-m/Sqrt[Alpha], Sqrt[Alpha]/(2 m)}];
VectorLength[x_] := Sqrt[x[[1]]^2 + x[[2]]^2];
L[x_, y_] := Sqrt[x^2 + y^2];
RealQ[x_] := If[Re[x] - x == 0, True, False];

AlphaMax = 100;
AlphaMin = 0.5;
NumTolerance = 0.05;(*Tolerance for numerical checks*)
mMax = Floor[Sqrt[2 AlphaMax/Sqrt[3]]]
CandidateStates = {};
For[m = 1, m <= mMax, m++,
  For[n = 1, n <= m, n++, AppendTo[CandidateStates, {m, n}]]];
HexaticMinima = {};
For[i = 1, i <= Length[CandidateStates], i++,
  m = CandidateStates[[i, 1]];
  n = CandidateStates[[i, 2]];
  If[AlphaMinus[m, n] <= AlphaMax,
   AppendTo[HexaticMinima, {N[AlphaMinus[m, n]], m, n}]];
  If[AlphaPlus[m, n] <= AlphaMax,
   AppendTo[HexaticMinima, {N[AlphaPlus[m, n]], m, n}]];
  ];


HexaticMinima =
 Sort[HexaticMinima](*Numerical values required for sorting algorithm \
to work*)

Transitions = {{0, 1, 1}};
LeftMin =
 HexaticMinima[[2,
   1]];(*Start from second minima since there are no transitions \
before it*)
RightMin = HexaticMinima[[4, 1]];(*We already know this one too*)
CurrentGS = {1, 1};


While[RightMin < AlphaMax,
  LeftStates = {};
  For[i = 1, i <= Length[HexaticMinima], i++,
   If[HexaticMinima[[i, 1]] ==
       LeftMin && {HexaticMinima[[i, 2]], HexaticMinima[[i, 3]]} !=
       CurrentGS,
     AppendTo[
      LeftStates, {HexaticMinima[[i, 2]], HexaticMinima[[i, 3]]}]];
```

```
];

 (*Print[ParabolicSolutions];*)

 For[j = 1, j <= Length[ParabolicSolutions], j++,
  CandidateAlpha = Alpha /. ParabolicSolutions[[j]];

  (*Print[{N[CandidateAlpha],LeftStates[[i]]}];(*Debug*)*)

  If[RealQ[CandidateAlpha],
   If[LeftMin + NumTolerance < CandidateAlpha <
      RightMin -
       NumTolerance,(*Possible transition found*)(*Check tolerance*)

     TransitionsFound = True;
     AppendTo[
      CandidateTransitions, {CandidateAlpha, LeftStates[[i, 1]],
       LeftStates[[i, 2]]}];
     ];
   ];
  ];
 ];


TransitionsFound = True;
While[TransitionsFound == True,(*Exploiting Boolean logic to re-
 enter this loop*)
 TransitionsFound = False;
 j = 1;
 While[HexaticMinima[[j, 1]] <= LeftMin, j++;]
  RightMin = HexaticMinima[[j, 1]];
 RightStates = {};
 For[i = 1, i <= Length[HexaticMinima], i++,
  If[HexaticMinima[[i, 1]] == RightMin,
    AppendTo[
     RightStates, {HexaticMinima[[i, 2]], HexaticMinima[[i, 3]]}]];
 ];

 (*Print["LRMINS:"];
 Print[{LeftMin,RightMin}];*)

 (*LeftStates;
 RightStates;*)
 CandidateTransitions = {};
 aGS = LatticeVector[CurrentGS[[1]], CurrentGS[[2]]];


 For[i = 1, i <= Length[LeftStates], i++,
  aCandidate = LatticeVector[LeftStates[[i, 1]], LeftStates[[i, 2]]];

  RotationSolutions =
   Solve[VectorLength[aGS] == VectorLength[aCandidate], Alpha];
  For[j = 1, j <= Length[RotationSolutions], j++,
   CandidateAlpha = Alpha /. RotationSolutions[[j]];
   If[RealQ[CandidateAlpha],
    If[LeftMin + NumTolerance < CandidateAlpha <
```

```
      RightMin -
       NumTolerance,(*Possible transition found*)(*Check tolerance*)

     TransitionsFound = True;
     AppendTo[
      CandidateTransitions, {CandidateAlpha, LeftStates[[i, 1]],
       LeftStates[[i, 2]]}];
     ];
   ];
  ];

 ParabolicSolutions =
  NSolve[VectorLength[aGS] == Sqrt[2/Sqrt[3]] - 1 &&
    VectorLength[aCandidate] == Sqrt[2/Sqrt[3]] + 1, {Alpha, 1}];


For[i = 1, i <= Length[RightStates], i++,
 aCandidate =
  LatticeVector[RightStates[[i, 1]], RightStates[[i, 2]]];

 RotationSolutions =
  Solve[VectorLength[aGS] == VectorLength[aCandidate], Alpha];
 (*Print[RotationSolutions];*)
 For[j = 1, j <= Length[RotationSolutions], j++,
  CandidateAlpha = Alpha /. RotationSolutions[[j]];
  (*Print[CandidateAlpha];*)(*Debug*)
  If[RealQ[CandidateAlpha],
   If[LeftMin + NumTolerance < CandidateAlpha <
      RightMin -
       NumTolerance,(*Possible transition found*)(*Check tolerance*)

     TransitionsFound = True;
     AppendTo[
      CandidateTransitions, {CandidateAlpha, RightStates[[i, 1]],
       RightStates[[i, 2]]}];
     ];
   ];
  ];


 ParabolicSolutions =
  NSolve[VectorLength[aGS] == Sqrt[2/Sqrt[3]] - 1 &&
    VectorLength[aCandidate] == Sqrt[2/Sqrt[3]] + 1, {Alpha, 1}];
 (*Print[RotationSolutions];*)
 For[j = 1, j <= Length[ParabolicSolutions], j++,
  CandidateAlpha = Alpha /. ParabolicSolutions[[j]];

  (*Print[{N[CandidateAlpha],RightStates[[i]]}];(*Debug*)*)

  If[RealQ[CandidateAlpha],
   If[LeftMin + NumTolerance < CandidateAlpha <
      RightMin -
       NumTolerance,(*Possible transition found*)(*Check tolerance*)

     TransitionsFound = True;
     AppendTo[
```

```
        CandidateTransitions, {CandidateAlpha, RightStates[[i, 1]],
         RightStates[[i, 2]]}];
       ];
     ];
    ];
   ];
  If[TransitionsFound == True,
   CandidateTransitions = Sort[CandidateTransitions];
   AppendTo[Transitions,
    CandidateTransitions[[1]]];(*The first to occur*)
   CurrentGS = {Transitions[[Length[Transitions], 2]],
     Transitions[[Length[Transitions],
       3]]};(*Now check to see if there are more transitions before the right minimum,
   LeftMin =
    Transitions[[Length[Transitions], 1]]; (*New minimum value of alpha*)

   , LeftMin = RightMin(*Else*)
   ];
  ];

];
```

Bibliography

[1] Cilk plus tutorial. https://www.cilkplus.org/cilk-plus-tutorial. Accessed on 28-09-2017.

[2] Flowsquare 4.0. http://flowsquare.com/. Accessed on 04-09-2017.

[3] Intel c++ and fortran compilers. https://software.intel.com/en-us/intel-compilers. Accessed on 17-09-2017.

[4] Inverse tangent – from worlfam mathworld. http://mathworld.wolfram.com/InverseTangent.html. Accessed on 22-09-2017.

[5] Migrate your application to use openmp or intel(r) tbb instead of intel(r) cilk(tm) plus. https://software.intel.com/en-us/articles/migrate-your-application-to-use-openmp-or-intelr-tbb-instead-of-intelr-cilktm-plus. Accessed on 2017-09-17.

[6] Physical constants - the physics hypertextbook. https://physics.info/constants/. Accessed on 27-09-2017.

[7] What is gpgpu. http://whatis.techtarget.com/definition/GPGPU-general-purpose-graphics-processing-unit. Accessed on 28-09-2017.

[8] Wolfram language documentation. http://reference.wolfram.com/language/. Accessed on 17-09-2017.

[9] Wolfram language documentation - nsolve. http://reference.wolfram.com/language/ref/NSolve.html. Accessed on 20-09-2017.

[10] A.A. Abrikosov. On the magnetic properties of superconductors of the second group. *Soviet Physics Jetp*, 32:1442–1452, 1957. doi:10.1016/0022-3697(57)90083-5.

[11] H. Airy. On leaf-arrangement. *Proc. R. Soc. Lond.*, 21(139-147):176–179, 1872. doi:10.1098/rspl.1872.0040.

[12] Ariel Amir, Jayson Paulose, and David R. Nelson. Theory of interacting dislocations on cylinders. *Phys. Rev. E*, 87(4):042314, 2013. doi:10.1103/physreve.87.042314.

[13] Hans C. Andersen. Molecular dynamics simulations at constant pressure and/or temperature. *The Journal of Chemical Physics*, 72(4):2384–2393, 1980. doi:10.1063/1.439486.

[14] J. F. Annett. *Superconductivity, Superfluids and Condensates*. Oxford University Press, 2009.

[15] Moto Araki and Hisao Hayakawa. Steplike electric conduction in a classical two-dimensional electron system through a narrow constriction in a microchannel. *Phys. Rev. B*, 86:165412, Oct 2012. doi:10.1103/PhysRevB.86.165412.

[16] T. Atobe, M. Funakoshi, and S. Inoue. Orbital instability and chaos in the stokes flow between two eccentric cylinders. *Fluid Dynamics Research*, 16(2-3):115, 1995. 10.1016/0169-5983(94)00018-U.

[17] Egor Babaev and Martin Speight. Semi-meissner state and neither type-i nor type-ii superconductivity in multicomponent superconductors. *Phys. Rev. B*, 72:180502, 2005. doi:10.1103/PhysRevB.72.180502.

[18] J. Bardeen, L. N. Cooper, and J. R. Schrieffer. Microscopic theory of superconductivity. *Phys. Rev.*, 106:162–164, Apr 1957. 10.1103/PhysRev.106.162.

[19] John Bardeen and M. J. Stephen. Theory of the motion of vortices in superconductors. *Phys. Rev.*, 140:A1197–A1207, 1965. doi:10.1103/PhysRev.140.A1197.

[20] Petrucio Barrozo, André A. Moreira, J. Albino Aguiar, and José S. Andrade. Model of overdamped motion of interacting magnetic vortices through narrow superconducting channels. *Phys. Rev. B*, 80:104513, Sep 2009. doi:10.1103/PhysRevB.80.104513.

[21] C. P. Bean and J. D. Livingston. Surface barrier in type-ii superconductors. *Phys. Rev. Lett.*, 12:14–16, Jan 1964. doi:10.1103/PhysRevLett.12.14.

[22] G. Bergmann. Amorphous metals and their superconductivity. *Physics Reports*, 27(4):159 – 185, 1976. doi:10.1016/0370-1573(76)90040-5.

[23] R Besseling, P H Kes, T Drse, and V M Vinokur. Depinning and dynamics of vortices confined in mesoscopic flow channels. *New Journal of Physics*, 7(1):71, 2005.

[24] R. Besseling, R. Niggebrugge, and P. H. Kes. Transport properties of vortices in easy flow channels: A frenkel-kontorova study. *Phys. Rev. Lett.*, 82:3144–3147, Apr 1999. doi:10.1103/PhysRevLett.82.3144.

[25] J. C. N. Carvalho, K. Nelissen, W. P. Ferreira, G. A. Farias, and F. M. Peeters. Diffusion in a quasi-one-dimensional system on a periodic substrate. *Phys. Rev. E*, 85:021136, Feb 2012. doi:10.1103/PhysRevE.85.021136.

[26] L. Civale, A. D. Marwick, T. K. Worthington, M. A. Kirk, J. R. Thompson, L. Krusin-Elbaum, Y. Sun, J. R. Clem, and F. Holtzberg. Vortex confinement by columnar defects in $yba_2cu_3o_7$ crystals: Enhanced pinning at high fields and temperatures. *Phys. Rev. Lett.*, 67:648–651, Jul 1991. doi:10.1103/PhysRevLett.67.648.

[27] D. Cole, S. Bending, S. Savel'ev, A. Grigorenko, T. Tamegai, and F. Nori. Ratchet without spatial asymmetry for controlling the motion of magnetic flux quanta using time-asymmetric drives. *Nature Materials*, 5:305–311, 2006. doi:10.1038/nmat1608.

[28] E. Conen and A. Schmid. Properties of a superconducting film in a perpendicular magnetic field. *Journal of Low Temperature Physics*, 17(3):331–340, Nov 1974. doi:10.1007/BF00659078.

[29] Christophe Coste, Jean-Baptiste Delfau, and Michel Saint Jean. Longitudinal and transverse single file diffusion in quasi-1d systems. *Biophys. Rev. Lett.*, 09(04):333–348, 2014. doi:10.1142/s1793048014400025.

[30] Jean-Baptiste Delfau, Christophe Coste, and Michel Saint Jean. Noisy zigzag transition, fluctuations, and thermal bifurcation threshold. *Phys. Rev. E*, 87:062135, Jun 2013. doi:10.1103/PhysRevE.87.062135.

[31] Jean-Baptiste Delfau, Christophe Coste, and Michel Saint Jean. Transverse single-file diffusion near the zigzag transition. *Phys. Rev. E*, 87:032163, Mar 2013. doi:10.1103/PhysRevE.87.032163.

[32] Nist digital library of mathematical functions. http://dlmf.nist.gov/, release 1.0.15, accessed on 01-06-2017. F. W. J. Olver, A. B. Olde Daalhuis, D. W. Lozier, B. I. Schneider, R. F. Boisvert, C. W. Clark, B. R. Miller and B. V. Saunders, eds.

[33] Jinming Dong. Simulation of the vortex motion in high-t c superconductors. *Journal of Physics: Condensed Matter*, 5(20):3359, 1993.

[34] W.J. Duffin. *Electricity and Magnetism*. McGraw-Hill, fourth edition, 1990. ISBN: 0-07-707209-X, pp: 150–151.

[35] Moore G. E. Cramming more components onto integrated circuits. *Electronics*, 38(11):114, 1965. doi:10.1109/N-SSC.2006.4785860.

[36] R. O. Erickson. Tubular packing of spheres in biological fine structure. *Science*, 181(4101):705–716, 1973. doi:10.1126/science.181.4101.705.

[37] U. Essmann and H. Truble. The direct observation of individual flux lines in type ii superconductors. *Physics Letters A*, 24(10):526 – 527, 1967. doi:10.1016/0375-9601(67)90819-5.

[38] Denis J. Evans and O.P. Morriss. Non-newtonian molecular dynamics. *Computer Physics Reports*, 1(6):297 – 343, 1984. 10.1016/0167-7977(84)90001-7.

[39] Daniel S. Fisher. Flux-lattice melting in thin-film superconductors. *Phys. Rev. B*, 22:1190–1199, Aug 1980. doi:10.1103/PhysRevB.22.1190.

[40] E. M. Forgan, P. G. Kealey, S. T. Johnson, A. Pautrat, Ch. Simon, S. L. Lee, C. M. Aegerter, R. Cubitt, B. Farago, and P. Schleger. Measurement of vortex motion in a type-ii superconductor: A novel use of the neutron spin-echo technique. *Phys. Rev. Lett.*, 85:3488–3491, Oct 2000. doi:10.1103/PhysRevLett.85.3488.

[41] Lin Fu, William Steinhardt, Hao Zhao, Joshua E. S. Socolar, and Patrick Charbon-

neau. Hard sphere packings within cylinders. *Soft Matter*, 12(9):2505–2514, 2016. doi:10.1039/c5sm02875b.

[42] J. E. Galván-Moya, D. Lucena, W. P. Ferreira, and F. M. Peeters. Magnetic particles confined in a modulated channel: Structural transitions tunable by tilting a magnetic field. *Phys. Rev. E*, 89:032309, Mar 2014. doi:10.1103/PhysRevE.89.032309.

[43] J. E. Galván-Moya, V. R. Misko, and F. M. Peeters. Chainlike transitions in wigner crystals: Sequential versus nonsequential. *Phys. Rev. B*, 92:064112, Aug 2015. doi:10.1103/PhysRevB.92.064112.

[44] J. E. Galván-Moya, K. Nelissen, and F. M. Peeters. Structural transitions in vertically and horizontally coupled parabolic channels of wigner crystals. *Phys. Rev. B*, 86:184102, Nov 2012. doi:10.1103/PhysRevB.86.184102.

[45] P. L. Gammel, A. F. Hebard, and D. J. Bishop. Flux-lattice melting in amorphous composite $\frac{\text{in}}{\text{ino}_x}$ two-dimensional superconductors. *Phys. Rev. Lett.*, 60:144–147, Jan 1988. doi:10.1103/PhysRevLett.60.144.

[46] M. J. Godfrey and M. A. Moore. Static and dynamical properties of a hard-disk fluid confined to a narrow channel. *Phys. Rev. E*, 89(3), 2014. doi:10.1103/physreve.89.032111.

[47] A. V. Holden. *Chaos*. Manchester University Press, 1987.

[48] B. A. Huberman and S. Doniach. Melting of two-dimensional vortex lattices. *Phys. Rev. Lett.*, 43:950–952, Sep 1979. doi:10.1103/PhysRevLett.43.950.

[49] E. Infeld and G. Rowlands. *Nonlinear Waves, Solitons and Chaos.* Cambridge University Press, second edition, 2000.

[50] M. H. Kalos and P. A Whitlock. *Monte Carlo Methods.* Whiley-VCH, second edition, 2008.

[51] T. J. Kaper and S. Wiggins. An analytical study of transport in stokes flows exhibiting large-scale chaos in the eccentric journal bearing. *Journal of Fluid Mechanics*, 253:211243, 1993. 10.1017/S0022112093001776.

[52] G. Karapetrov, M. V. Milošević, M. Iavarone, J. Fedor, A. Belkin, V. Novosad, and F. M. Peeters. Transverse instabilities of multiple vortex chains in magnetically coupled $nbse_2$/permalloy superconductor/ferromagnet bilayers. *Phys. Rev. B*, 80:180506, Nov 2009. doi:10.1103/PhysRevB.80.180506.

[53] G. Karapetrov, V. Yefremenko, G. Mihajlović, J. E. Pearson, M. Iavarone, V. Novosad, and S. D. Bader. Evidence of vortex jamming in abrikosov vortex flux flow regime. *Phys. Rev. B*, 86:054524, Aug 2012. doi:10.1103/PhysRevB.86.054524.

[54] P. G. Kealey, T. M. Riseman, E. M. Forgan, L. M. Galvin, A. P. Mackenzie, S. L. Lee, D. McK. Paul, R. Cubitt, D. F. Agterberg, R. Heeb, Z. Q. Mao, and Y. Maeno. Reconstruction from small-angle neutron scattering measurements of the real space magnetic field distribution in the mixed state of sr_2ruo_4. *Phys. Rev. Lett.*, 84:6094–6097, Jun 2000. doi:10.1103/PhysRevLett.84.6094.

[55] P.H. Kes, N. Kokubo, and R. Besseling. Vortex matter driven through mesoscopic channels. *Physica C: Superconductivity*, 408:478 – 481, 2004. doi:10.1016/j.physc.2004.03.182.

[56] Andrei N. Khlobystov, David A. Britz, Arzhang Ardavan, and G. Andrew D. Briggs. Observation of ordered phases of fullerenes in carbon nanotubes. *Phys. Rev. Lett.*, 92(24):245407, 2004. doi:10.1103/physrevlett.92.245507.

[57] David A. Kofke and Albert J. Post. Hard particles in narrow pores. transfer-matrix solution and the periodic narrow box. *J. Chem. Phys.*, 98(6):4853, 1993. doi:10.1063/1.464967.

[58] N. Kokubo, T. G. Sorop, R. Besseling, and P. H. Kes. Vortex-slip transitions in superconducting $a-$NbGe mesoscopic channels. *Phys. Rev. B*, 73:224514, Jun 2006. doi:10.1103/PhysRevB.73.224514.

[59] L. Komendová, M. V. Milošević, and F. M. Peeters. Soft vortex matter in a type-i/type-ii superconducting bilayer. *Phys. Rev. B*, 88:094515, Sep 2013. doi:10.1103/PhysRevB.88.094515.

[60] S. E. Koonin and D. Meredith. *Computational Physics*. Addison-Wesley, fortran edition, 1990.

[61] M. K$'$oppl, P. Henseler, A. Erbe, P. Nielaba, and P. Leiderer. Layer reduction in driven 2d-colloidal systems through microchannels. *Phys. Rev. Lett.*, 97:208302, Nov 2006. doi:10.1103/PhysRevLett.97.208302.

[62] A. E. Koshelev and V. M. Vinokur. Dynamic melting of the vortex lattice. *Phys. Rev. Lett.*, 73:3580–3583, Dec 1994. doi:10.1103/PhysRevLett.73.3580.

[63] G. L. Lamb. *Elements of Soliton Theory*. Wiley, 1980.

[64] L. D. Landau and E. M. Lifshitz. *Theory of Elasticity, 3rd edition, Course of Theoretical Physics Vol. 7*. Pergamon, 1986.

[65] Q. Le Thien, D. McDermott, C. J. Olson Reichhardt, and C. Reichhardt. Orientational ordering, buckling, and dynamic transitions for vortices interacting with a periodic quasi-one-dimensional substrate. *Phys. Rev. B*, 93:014504, 2016. doi:10.1103/PhysRevB.93.014504.

[66] Don S. Lemons and Anthony Gythiel. Paul langevins 1908 paper on the theory of brownian motion [sur la thorie du mouvement brownien, c. r. acad. sci. (paris) 146, 530533 (1908)]. *American Journal of Physics*, 65(11):1079–1081, 1997. doi:10.1119/1.18725.

[67] Ruijing Liang, Jiangping Xu, Renhua Deng, Ke Wang, Shanqin Liu, Jingyi Li, and Jintao Zhu. Assembly of polymer-tethered gold nanoparticles under cylindrical confinement. *ACS Macro Lett*, 3(5):486–490, 2014. doi:10.1021/mz5002146.

[68] N. S. Lin, T. W. Heitmann, K. Yu, B. L. T. Plourde, and V. R. Misko. Rectification of vortex motion in a circular ratchet channel. *Phys. Rev. B*, 84:144511, Oct 2011. doi:10.1103/PhysRevB.84.144511.

[69] N. Lo Gullo, Th. Busch, and M. Paternostro. Structural change of vortex patterns in anisotropic bose-einstein condensates. *Phys. Rev. A*, 83:053612, May 2011. doi:10.1103/PhysRevA.83.053612.

[70] F. London and H. London. The electromagnetic equations of the supraconductor. *Proceedings of the Royal Society of London A: Mathematical, Physical and Engineering Sciences*, 149(866):71–88, 1935. doi:10.1098/rspa.1935.0048.

[71] D. Lucena, D. V. Tkachenko, K. Nelissen, V. R. Misko, W. P. Ferreira, G. A. Farias, and F. M. Peeters. Transition from single-file to two-dimensional diffusion of interacting particles in a quasi-one-dimensional channel. *Phys. Rev. E*, 85:031147, Mar 2012. doi:10.1103/PhysRevE.85.031147.

[72] José I. Martín, M. Vélez, A. Hoffmann, Ivan K. Schuller, and J. L. Vicent. Artificially induced reconfiguration of the vortex lattice by arrays of magnetic dots. *Phys. Rev. Lett.*, 83:1022–1025, Aug 1999. doi:10.1103/PhysRevLett.83.1022.

[73] W. Meissner and R. Ochsenfeld. Ein neuer effekt bei eintritt der supraleitfähigkeit. *Naturwissenschaften*, 21(44):787–788, Nov 1933. 10.1007/BF01504252.

[74] N. D. Mermin and H. Wagner. Absence of ferromagnetism or antiferromagnetism in one- or two-dimensional isotropic heisenberg models. *Phys. Rev. Lett.*, 17:1133–1136, 1966.

[75] Victor Moshchalkov, Mariela Menghini, T. Nishio, Q. H. Chen, A. V. Silhanek, V. H. Dao, L. F. Chibotaru, N. D. Zhigadlo, and J. Karpinski. Type-1.5 superconductivity. *Phys. Rev. Lett.*, 102:117001, 2009. doi:10.1103/PhysRevLett.102.117001.

[76] A. Mughal, H. K. Chan, and D. Weaire. Phyllotactic description of hard sphere packing in cylindrical channels. *Phys. Rev. Lett.*, 106(11):115704, 2011. doi:10.1103/physrevlett.106.115704.

[77] A. Mughal, H. K. Chan, D. Weaire, and S. Hutzler. Dense packings of spheres in cylinders: Simulations. *Phys. Rev. E*, 85(5):051305, 2012. doi:10.1103/physreve.85.051305.

[78] A. Mughal and D. Weaire. Theory of cylindrical dense packings of disks. *Phys. Rev. E*, 89:042307, Apr 2014. doi:10.1103/PhysRevE.89.042307.

[79] A. Mughal and D. Weaire. Phyllotaxis, disk packing, and fibonacci numbers. *Phys. Rev. E*, 95:022401, Feb 2017. doi:10.1103/PhysRevE.95.022401.

[80] S. Mühlbauer, C. Pfleiderer, P. Böni, M. Laver, E. M. Forgan, D. Fort, U. Keiderling, and G. Behr. Morphology of the superconducting vortex lattice in ultrapure niobium. *Phys. Rev. Lett.*, 102:136408, Apr 2009. doi:10.1103/PhysRevLett.102.136408.

[81] C. J. Olson Reichhardt and C. Reichhardt. Vortex clogging, commensuration, and diodes in asymmetric constriction arrays. *Journal of Superconductivity and Novel Magnetism*, 26(5):2005–2008, May 2013. doi:10.1007/s10948-012-2086-z.

[82] H. K. Onnes. Further experiments with liquid helium. on the electrical resistance of pure metals, etc. vi. on the sudden change in the rate at which the resistance of mercury disappears. *Comm. Phys. Lab. Univ. Leiden*, (124c), 1911.

[83] A. Oral, S. J. Bending, and M. Henini. Realtime scanning hall probe microscopy. *Applied Physics Letters*, 69(9):1324–1326, 1996. doi:10.1063/1.117582.

[84] E. C. Oğuz, R. Messina, and H. Löwen. Helicity in cylindrically confined yukawa systems. *EPL*, 94(2):28005, 2011. doi:10.1209/0295-5075/94/28005.

[85] H L Partner, R Nigmatullin, T Burgermeister, K Pyka, J Keller, A Retzker, M B Plenio, and T E Mehlstubler. Dynamics of topological defects in ion coulomb crystals. *New Journal of Physics*, 15(10):103013, 2013.

[86] W. Paul and H. Steinwedel. Verfahren zur trennung bzw. zum getrennten nachweis von ionen verschiedener spezifischer ladung - method for the separation and detection of the separated ions of different specific charge, 1956. DE Patent 944,900.

[87] G. Piacente, G. Q. Hai, and F. M. Peeters. Continuous structural transitions in quasi-one-dimensional classical wigner crystals. *Phys. Rev. B*, 81(2):024108, 2010. doi:10.1103/physrevb.81.024108.

[88] G. Piacente and F. M. Peeters. Pinning and depinning of a classic quasi-one-dimensional wigner crystal in the presence of a constriction. *Phys. Rev. B*, 72:205208, Nov 2005. doi:10.1103/PhysRevB.72.205208.

[89] G. Piacente, I. V. Schweigert, J. J. Betouras, and F. M. Peeters. Generic properties of a quasi-one-dimensional classical wigner crystal. *Phys. Rev. B*, 69(4):045324, 2004. doi:10.1103/physrevb.69.045324.

[90] B. L. T. Plourde, D. J. Van Harlingen, N. Saha, R. Besseling, M. B. S. Hesselberth, and P. H. Kes. Vortex distributions near surface steps observed by scanning squid microscopy. *Phys. Rev. B*, 66:054529, Aug 2002. doi:10.1103/PhysRevB.66.054529.

[91] A. Pruymboom, P. H. Kes, E. van der Drift, and S. Radelaar. Flux-line shear through narrow constraints in superconducting films. *Phys. Rev. Lett.*, 60:1430–1433, Apr 1988. doi:10.1103/PhysRevLett.60.1430.

[92] D. C. Rapaport. *The Art of Moleuclar Dynamics Simulation*. Cambridge University Press, second edition, 2004.

[93] D. G. Rees, H. Totsuji, and K. Kono. Commensurability-dependent transport of

a wigner crystal in a nanoconstriction. *Phys. Rev. Lett.*, 108:176801, Apr 2012. doi:10.1103/PhysRevLett.108.176801.

[94] C Reichhardt and C J Olson Reichhardt. Structural transitions and dynamical regimes for directional locking of vortices and colloids driven over periodic substrates. *Journal of Physics: Condensed Matter*, 24(22):225702, 2012.

[95] C. J. Olson Reichhardt and C. Reichhardt. Coherent and incoherent vortex flow states in crossed channels. *EPL (Europhysics Letters)*, 88(4):47004, 2009.

[96] C. J. Olson Reichhardt and C. Reichhardt. Commensurability, jamming, and dynamics for vortices in funnel geometries. *Phys. Rev. B*, 81:224516, Jun 2010. doi:10.1103/PhysRevB.81.224516.

[97] C.J. Olson Reichhardt and C. Reichhardt. Vortex dynamics and symmetry locking on quasiperiodic and periodic substrates. *Physica C: Superconductivity*, 479:45 – 48, 2012. doi:10.1016/j.physc.2011.12.015.

[98] T.M. Riseman, P.G. Kealey, E.M. Forgan, A.P. Mackenzie, Galvin L.M., A.W. Tyler, S.L. Lee, C. Ager, D.M. Paul, C.M. Aegerter, R. Cubitt, Z.Q. Mao, T. Akima, and Y. Maeno. Observation of a square flux-line lattice in the unconventional superconductor Sr_2RuO_4. *Letters to Nature*, 396:242–254, 1998. doi:10.1038/24335.

[99] H. Shih, T. Hsieh, and N Goldenfeld. Ecological collapse and the emergence of travelling waves at the onset of shear turbulence. *Nature Physics*, 12:245–248, 2016. 10.1038/nphys3548.

[100] W. S. Slaughter. *The Linearized Theory of Elasticity.* Birkhäuser Boston, 2002.

[101] Steven Spencer and Henrik Jeldtoft Jensen. Absence of translational ordering in driven vortex lattices. *Phys. Rev. B*, 55:8473–8481, Apr 1997. doi:10.1103/PhysRevB.55.8473.

[102] Julien Clinton Sprott. *Chaos and Time-Series Analysis*. Oxford University Press, 2003.

[103] Arthur V. Straube, Roel P. A. Dullens, Lutz Schimansky-Geier, and Ard A. Louis. Zigzag transitions and nonequilibrium pattern formation in colloidal chains. *J. Chem. Phys.*, 139(13):134908, 2013. doi:10.1063/1.4823501.

[104] K. A. Stroud. *Advanced Engineering Mathematics*. Palgrave Macmillan, fourth edition, 2003.

[105] William C. Swope, Hans C. Andersen, Peter H. Berens, and Kent R. Wilson. A computer simulation method for the calculation of equilibrium constants for the formation of physical clusters of molecules: Application to small water clusters. *The Journal of Chemical Physics*, 76(1):637–649, 1982. doi:10.1063/1.442716.

[106] D. R. Tilley and J. Tiley. *Superfluidity and Superconductivity*. Institute of Physics Publishing, third edition, 2003.

[107] Michael Tinkham. *Introduction to Superconductivity: Second Edition*. Dover Publications, second edition, 2004.

[108] Austin Alexander Tomlinson. Vortex flow through very thin channels in type ii superconductors. Fourth year project report, University of Birmingham, April 2013.

[109] Austin Alexander Tomlinson. Vortex dynamics in periodic confining potentials. Mid-course assessment, University of Birmingham, September 2014.

[110] Anna A. Vasylenko and Vyacheslav R. Misko. Nonlinear transport of the wigner crystal in symmetric and asymmetric fet-like structures. *The European Physical Journal B*, 88(4):105, Apr 2015. doi:10.1140/epjb/e2015-60217-0.

[111] J. S. Watkins and N. K. Wilkin. Extruding the vortex lattice: two reacting populations of dislocations. *ArXiv e-prints 1601.06542v1*, January 2016.

[112] Jonathan Stewart Watkins. *Density Driven Vortex Motion in Narrow Channel Superconductors*. Phd thesis, University of Birmingham, September 2015.

[113] J. Weertman. *Elementary Dislocation Theory*. Macmillan, second edition, 1964.

[114] F.M. White. *Fluid Mechanics*. McGraw-Hill, seventh edition edition, 2011.

[115] Hassler Whitney. Differentiable manifolds. *Annals of Mathematics*, 37(3):645–680, 1936.

[116] E. Wigner. On the interaction of electrons in metals. *Phys. Rev.*, 46:1002–1011, Dec 1934. doi:10.1103/PhysRev.46.1002.

[117] Alan Wolf, Jack B. Swift, Harry L. Swinney, and John A. Vastano. Determining lyapunov exponents from a time series. *Physica D: Nonlinear Phenomena*, 16(3):285 – 317, 1984. doi:10.1016/0167-2789(85)90011-9.

[118] D. A. Wood, C. D. Santangelo, and A. D. Dinsmore. Self-assembly on a cylinder: a model system for understanding the constraint of commensurability. *Soft Matter*, 9:10016–10024, 2013. doi:10.1039/C3SM51735G.

[119] Yuan Xiao-Ping and Zheng Zhi-Gang. Ground-state transition in a two-dimensional frenkelkontorova model. *Chinese Physics Letters*, 28(10):100507, 2011.

[120] T Yamazaki, K Kuramochi, D Takagi, Y Homma, F Nishimura, N Hori, K Watanabe, S Suzuki, and Y Kobayashi. Ordered fullerene nanocylinders in large-diameter carbon nanotubes. *Nanotechnology*, 19(4):045702, 2008. doi:10.1088/0957-4484/19/04/045702.

[121] K. Yu, M. B. S. Hesselberth, P. H. Kes, and B. L. T. Plourde. Vortex dynamics in superconducting channels with periodic constrictions. *Phys. Rev. B*, 81:184503, May 2010. doi:10.1103/PhysRevB.81.184503.

[122] H. Yukawa. On the interaction of elementary particle japan physics and mathematics journal. *Proc. Phys. Math. Soc. Japan*, 48:48–56, 1935.

[123] E. Zeldov, D. Majer, M. Konczykowski, V. B. Geshkenbein, V. M. Vinokur, and Shtrikmanm H. Thermodynamic observation of first-order vortex-lattice melting transition in $Bi_2Sr_2CaCu_2O_8$. *Nature*, 375:373–376, 1995. doi:10.1038/375373a0.

[124] F. C. Zhang and T. M. Rice. Effective hamiltonian for the superconducting cu oxides. *Phys. Rev. B*, 37:3759–3761, Mar 1988. 10.1103/PhysRevB.37.3759.

[125] Urs Zimmermann, Frank Smallenburg, and Hartmut Lwen. Flow of colloidal solids and fluids through constrictions: dynamical density functional theory versus simulation. *Journal of Physics: Condensed Matter*, 28(24):244019, 2016.